FERMILAB-THESIS-2000-31

Search for a Fourth-Generation Quark More Massive than the Z^0 Boson in $p\overline{p}$ Collisions at $\sqrt{s} = 1.8$ TeV

by

João Pedro Barreiro Guimarães da Costa

A dissertation submitted in partial fulfillment
of the requirements for the degree of
Doctor of Philosophy
(Physics)
in The University of Michigan
2000

Doctoral Committee:

Assistant Professor David W. Gerdes, Chair
Associate Professor Dante E. Amidei
Professor Gordon L. Kane
Assistant Professor Timothy A. McKay
Professor Gopal Prasad

Para os meus pais

Acknowledgments

I want to thank my advisor, David Gerdes, for his guidance throughout my graduate work. I am especially thankful to him for letting me graduate before scoring fewer than 100 strokes in a 18-hole golf course. I am afraid I would be here forever otherwise! I would also like to express my sincere appreciation to Bruce Barnett for his helpful advice since my first years of graduate school.

I am truly grateful to the Fermilab staff and the CDF Collaboration. Without the contributions of all of them this research could not have happened. In particular, I would like to thank the CDF people that interacted directly with me in the course of this work. David Stuart, John Conway and Maxwell Chertok, as convenors of the exotics group during the bulk of the analysis, provided much input that was vital to its success. The godparents of this analysis, Karen Byrum, Thomas Muller and Alberto Ribon, help me make sure that the results were correct. I especially appreciated their willingness to work quickly in order to publish the result in a timely fashion. Rob Roser was always very helpful with information about the data samples and the CDF code.

I am thankful to George Hou, Robin Stuart and Herbert Greenlee for providing some of the computer code necessary for this research. Finally, I thank Professors Dan Amidei, Gordy Kane, Timothy McKay and Gopal Prasad for being part of my dissertation committee. I hope this was not too painful for them. Of course, I cannot forget Ken Bloom, who has always tried to keep me happy for the last couple of years. This work was supported by the U.S. Department of Energy and National Science Foundation; the Italian Istituto Nazionale di Fisica Nucleare; the Ministry of Education, Science, Sports and Culture of Japan; the Natural Sciences and Engineering Research Council of Canada; the National

Science Council of the Republic of China; the Swiss National Science Foundation; the A. P. Sloan Foundation; the Bundesministerium fuer Bildung und Forschung, Germany; and the Junta Nacional de Investigação Científica e Tecnológica (JNICT), Portugal.

Table of Contents

List of Tables

Table

List of Figures

Figure

Chapter 1

Introduction

The Standard Model (SM) of Particle Physics with three generations of quarks and leptons is in excellent agreement with all experimental data available today. There is no experimental indication that an extra fermion generation exists. However, the SM does not explain either the fermion family replication or the fermion mass hierarchy. Several theoretical models have been proposed to solve shortcomings in the Standard Model through the introduction of extra quarks and leptons, while grand unification, supersymmetry, supergravity and superstrings predict or can accomodate extra fermion states.

This dissertation reports on a search for a fourth-generation quark with charge $-1/3$ (b') more massive than the Z^0 boson. We use 87.8 pb^{-1} of $\bar{p}p$ collisions at $\sqrt{s} = 1.8$ TeV obtained with the Collider Detector at Fermilab (CDF) between 1994 and 1996. We search for b' quarks, pair-produced by the strong interaction, that would decay by flavor-changing neutral current into a b quark and a Z^0 boson. We study the decay mode $b'\overline{b'} \rightarrow b\bar{b}Z^0Z^0$ where one Z^0 decays into e^+e^- or $\mu^+\mu^-$ and the other decays hadronically, giving a signature of two leptons plus jets.

The thesis is organized as follows. In the remainder of this chapter, we motivate the search for this quark in this decay mode. Theoretical estimations and current experimental limits are presented. Chapter 2 gives a brief description of the experimental apparatus. The main components of the Fermilab accelerator system and the CDF detector are briefly discussed. The remaining chapters cover the steps necessary to analyze the data and draw

conclusions about the existence of this new quark. Chapter 3 describes the data sample and the event selection done to enhance the signal relative to the background. Chapter 4 is devoted to the calculation of the acceptance and efficiencies for the b' quark signal. Both detector and selection effects are included. The systematic uncertainties that affect the final acceptance calculation are examined in Chapter 5. The background estimation in the Z^0 + jets channel is discussed in Chapter 6. Chapter 7 presents the final results of the search. These include the calculation of an exclusion limit, some cross-checks, and a few comments. Finally, we conclude with a short summary of the dissertation in Chapter 8.

1.1 The Standard Model

The Standard Model (SM) of elementary particles and their fundamental interactions describes all phenomena currently observed in high energy physics experiments. According to the SM, the universe consists of a set of elementary particles that are the basic building blocks of matter and interact through four forces known as the electromagnetic, strong, weak and gravitational forces. Each force is carried by intermediate interaction particles. The matter particles, listed in Table 1.1, are spin-1/2 fermions and are classified into leptons and quarks. There are six leptons (l): the electron (e), the muon (μ) and the tau (τ) with electric charge -1; and their respective neutrinos ν_e, ν_μ, ν_τ with neutral electric charge. There are also six different flavors of quarks: up, down, charm, strange, bottom and top. The quarks differ from the leptons by having fractional charge and an additional quantum number known as color, which can take three different values: red, green and blue.

The forces between the particles above are listed in Table 1.2 together with their respective intermediate particles. The electromagnetic, the weak and the strong forces are mediated by the exchange of spin-1 bosons. The photon (γ) is the exchanged particle in the electromagnetic interaction. The strong interaction is mediated by eight gluons, and the three weak bosons ($W^\pm$ and Z^0) are the corresponding intermediate bosons of the weak interactions. The gravitational interactions are mediated by the graviton, a spin-2 boson. The strength of each force is characterized by a coupling constant. At low energies the

Generation	Particle	Symbol	Charge (e)	Mass (GeV/c^2)
	Electron	e	-1	5.1×10^{-4}
First	Electron neutrino	ν_e	0	$< 15 \times 10^{-9}$
	Up quark	u	2/3	1.5 - 5×10^{-3}
	Down quark	d	-1/3	3 - 9×10^{-3}
	Muon	μ	-1	1.06×10^{-1}
Second	Muon neutrino	ν_μ	0	$< 1.7 \times 10^{-4}$
	Charm quark	c	2/3	1.1 - 1.4
	Strange quark	s	-1/3	6 - 17×10^{-2}
	Tau	τ	-1	1.78
Third	Tau neutrino	ν_τ	0	$< 1.8 \times 10^{-2}$
	Top quark	t	2/3	173.8 ± 5.2
	Bottom quark	b	-1/3	4.1 - 4.4

Table 1.1: The Standard Model lepton and quark generations. The particles masses are from reference [1].

electromagnetic coupling strength is given by the fine structure constant, $\alpha \sim 1/137$. The weak interactions are characterized by a coupling of the order of $\alpha_W \sim 10^{-5}$ at energies much lower that the masses of the intermediate weak bosons. The strong force coupling constant α_s varies from a value of ~ 1 at large distances down to the asymptotic limit $\alpha_s \to 0$ for vanishingly small distances. Gravity ($\alpha_G \sim 10^{-38}$) is too weak to play an important role in the particle physics processes studied in this thesis and will not be discussed any further.

Force		Particle	Charge (e)	Mass (GeV/c^2)
Electromagnetic		Photon (γ)	0	0.
Strong		Gluon (g)	0	0.
Weak	Charged	W Boson ($W^\pm$)	± 1	80.3
	Neutral	Z Boson (Z^0)	0	91.2
Gravitational		Graviton (G)	0	0.

Table 1.2: The Standard Model fundamental forces and corresponding gauge bosons.

The charged lepton interactions are mediated by the electromagnetic and weak forces, while neutrinos, being electrically neutral, only participate in weak interactions.

Quarks carry both color and electric charge and therefore participate in interactions involving the strong, electromagnetic and weak forces. All particles mentioned above have an associated antiparticle with equal mass and spin but opposite charge. For instance, the electron has an antiparticle called the positron (e^+); the antiquarks are denoted by $\bar{u}, \bar{d}, \bar{s}, etc.$ The neutral particles like the photon, Z^0, and gluon are identical to their antiparticles.

The Standard Model is a quantum field theory that is based on the gauge symmetry $SU(3)_C \times SU(2)_L \times U(1)_Y$. This gauge group includes the symmetry group of the strong interactions $SU(3)_C$, and the symmetry group of the electroweak interactions $SU(2)_L \times U(1)_Y$. In the SM, the electroweak symmetry is spontaneously broken $SU(3)_C \times SU(2)_L \times U(1)_Y \rightarrow SU(3)_C \times U(1)_{em}$, where $U(1)_{em}$ is the group symmetry of the electromagnetic interaction. This symmetry-breaking is implemented by the Higgs mechanism which provides the non-zero masses to the weak bosons $W^{\pm}$ and Z^0, and predicts the existence of a new electrically-neutral scalar particle, the Higgs boson. The Higgs boson has yet to be confirmed experimentally and the mechanism for the electroweak symmetry breaking remains one of the great open questions of the SM.

In the SM with $SU(2)_L \times U(1)_Y$ as the gauge group of electroweak interactions, the fermions can be grouped into three generations (or families) as shown in Table 1.1. Each generation is a replica of the others except for the particle masses. Each contains a charged and neutral lepton, and an up-type and a down-type quark. The fermions are assigned to left-handed doublets and right-handed singlets as follows:

$$\begin{pmatrix} \nu_e \\ e \end{pmatrix}_L, \begin{pmatrix} u \\ d \end{pmatrix}_L, e_R,\ u_R,\ d_R.$$

$$\begin{pmatrix} \nu_\mu \\ \mu \end{pmatrix}_L, \begin{pmatrix} c \\ s \end{pmatrix}_L, \mu_R,\ c_R,\ s_R.$$

$$\begin{pmatrix} \nu_\tau \\ \tau \end{pmatrix}_L, \begin{pmatrix} t \\ b \end{pmatrix}_L, \tau_R,\ t_R,\ b_R.$$

The quark mass eigenstates are not the same as the weak interaction eigenstates. The 3×3 matrix relating them is known as Cabibbo-Kobayashi-Maskawa (CKM) matrix.

The mixing is expressed in terms of an unitary matrix operating on the charge $-1/3$ quarks. The matrix contains four independent parameters: three angles and one phase.

$$\begin{pmatrix} d \\ s \\ b \end{pmatrix}_{weak} = \begin{pmatrix} V_{ud} & V_{us} & V_{ub} \\ V_{cd} & V_{cs} & V_{cb} \\ V_{td} & V_{ts} & V_{tb} \end{pmatrix}_{CKM} \begin{pmatrix} d \\ s \\ b \end{pmatrix}_{mass}$$

1.2 Quarks beyond the SM

The Standard Model describes the fermion family replication but cannot explain why there is exactly three families and what is the origin of the mass hierarchy observed among the fermions. Extra fermion families could be added to the SM without much modification. The idea of a fourth generation has been considered from a number of different perspectives, such as,

- The scenario of dynamical electroweak symmetry breaking due to heavy-quark condensation [2]. In some models [3, 4] the top-quark mass is not large enough to be responsible for the electroweak symmetry breaking. Heavier quarks that couple to top would be required.

- A minimal four-family supergravity model [5].

- Supersymmetric models [6, 7] with four fermion families.

- Models that attempt to solve the strong-CP problem without axions can introduce a non-chiral doublet of quarks or non-chiral singlets [8].

- It has been shown that extending the SM with one extra generation can allow unification of the gauge couplings at the unification scale without supersymmetry [9].

- It has been argued [10] that flavor democracy, which requires that the Yukawa couplings of all fermions of a particular type with the Higgs boson before the diagonalisation of the mass matrix are equal, can be achieved in a four-generation model with

a heavy neutrino without requiring any large hierarchy among Yukawa couplings of the fermions of different types. This is no longer possible in a three-family model due to the high mass of the top quark and the relatively low masses of the other fermions.

In this thesis, we consider a new charge $-1/3$ quark (b') belonging to a standard sequential fourth generation.

$$\begin{pmatrix} u \\ d \end{pmatrix} \begin{pmatrix} c \\ s \end{pmatrix} \begin{pmatrix} t \\ b \end{pmatrix} \begin{pmatrix} t' \\ b' \end{pmatrix} \tag{1.1}$$

We assume that the b' quark is lighter than the t' quark, its partner in a SU(2) doublet. Nevertheless, our results should also apply to vector-like quarks, both doublets and singlets, with little or no modification.

1.2.1 Production and Decay of the b' Quark

Fourth-generation b' quarks can be pair-produced in $p\overline{p}$ collisions through gg fusion and $q\overline{q}$ annihilation with the same cross section, for a given mass, as top quarks. The tree-level diagrams for strong $b'\overline{b'}$ production are shown in Figure 1.1.

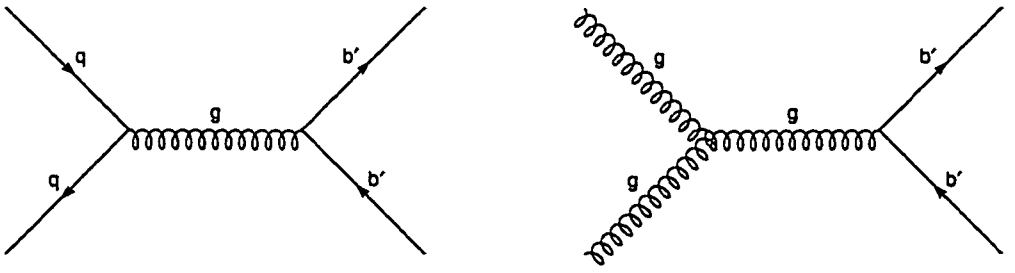

Figure 1.1: Feynman diagrams for pair production of the b' quark.

Each quark can decay via the the Standard Model charged current (CC), or via loop induced flavor-changing neutral currents (FCNC). In general, CC transitions are by far more important because the FCNC's are higher-order processes and can be suppressed by the

Glashow-Iliopoulos-Maiani (GIM) mechanism. However, if a b' quark exists and is lighter than both the t and t' quarks, the charged-current decays $b' \to tW^-$ and $b' \to t'W^-$ are kinematically forbidden. The leading charged-current decay mode will then be $b' \to cW^-$, shown in Figure 1.2, which is doubly Cabibbo-suppressed. That is, the CKM matrix element $V_{cb'}$ is expected to be very small because it represents the mixing between two non-adjacent families (for instance, the corresponding coefficient between the first and third families is $V_{ub} = 0.0018$ to 0.0045 [1]).

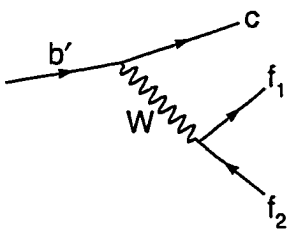

Figure 1.2: Charge current weak decay of a b' quark lighter than both t and t'.

On the other hand, the loop induced FCNC $b' \to bV^0$ shown in Figure 1.3, where V^0 is a neutral vector boson, carries the CKM coefficients

$$V_{tb}V_{tb'} \approx -V_{t'b}V_{t'b'} \tag{1.2}$$

and therefore has more or less the same CKM coefficients as the forbidden tree level transition $b' \to tW^-$ (since the processes corresponding to $V_{ub}V_{ub'}$ and $V_{cb}V_{cb'}$ would also be very Cabbibo suppressed). Box diagrams involving two W bosons also contribute, but it has been argued that these can be ignored [13]. In this situation FCNC decays can dominate [11, 12, 13] provided $|V_{cb'}|/|V_{tb'}|$ is less than roughly 10^{-2} to 10^{-3}, depending on the b' and t' masses [13]. This is a reasonable assumption when compared with the equivalent quantity for three generations $|V_{ub}|/|V_{cb}| = 0.08 \pm 0.02$ [1].

The $b' \to b\gamma$, $b' \to b +$ hadrons and $b' \to bZ^0$ width obtained with $m_t = 175$ GeV/c^2 are shown in Figure 1.4 as function of the b' and t' masses.[1] From these calculations, we

[1]The theoretical predictions for the different FCNC branching ratios were performed before the discovery

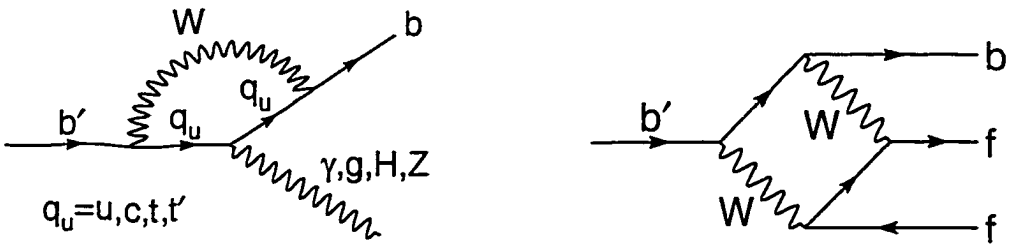

Figure 1.3: FCNC weak decays of the b' quark, where q_u represents any of the charge 2/3 quarks.

conclude that if $m_{b'} > m_Z + m_b$, the dominant FCNC decay mode is $b' \to bZ^0$ [13] as long $b' \to bH$ is kinematically suppressed or forbidden [16].

For $m_t < m_{b'} < m_t + m_W$, the decay mode $b' \to tW^*$ becomes available but is suppressed by three-body phase space, and the $b' \to bZ^0$ channel can still dominate over the CC decay for b' masses up to about 230 GeV/c^2 [11, 17].

1.2.2 Experimental Limits

The LEP experiments have established with high statistical precision that the number of light neutrinos (*i.e.*, $m_\nu < m_{Z/2}$) is three. This excludes the possibility of existence of a fourth generation of fermions with a zero or small mass neutrino. However, if a fourth-generation neutrino is heavier than $m_{Z/2}$, it would not show up in the "neutrino counting" experiment at LEP, and therefore the existence of an extra fermion generation is not excluded.

The direct experimental limits on the b' quark mass come from several sources. A summary of these limits is given in Figure 1.5. The experimental signatures of the t' and b' quark decays via charged currents to bottom and charm are very similar to the top quark signatures that have been studied at CDF and DØ. Therefore, on the assumption of

of the top quark [12, 13], therefore the authors assumed that $m_t = m_{b'} + 10$ GeV. We thank Robin Stuart for providing the program for the calculation with $m_t = 175$ GeV/c^2.

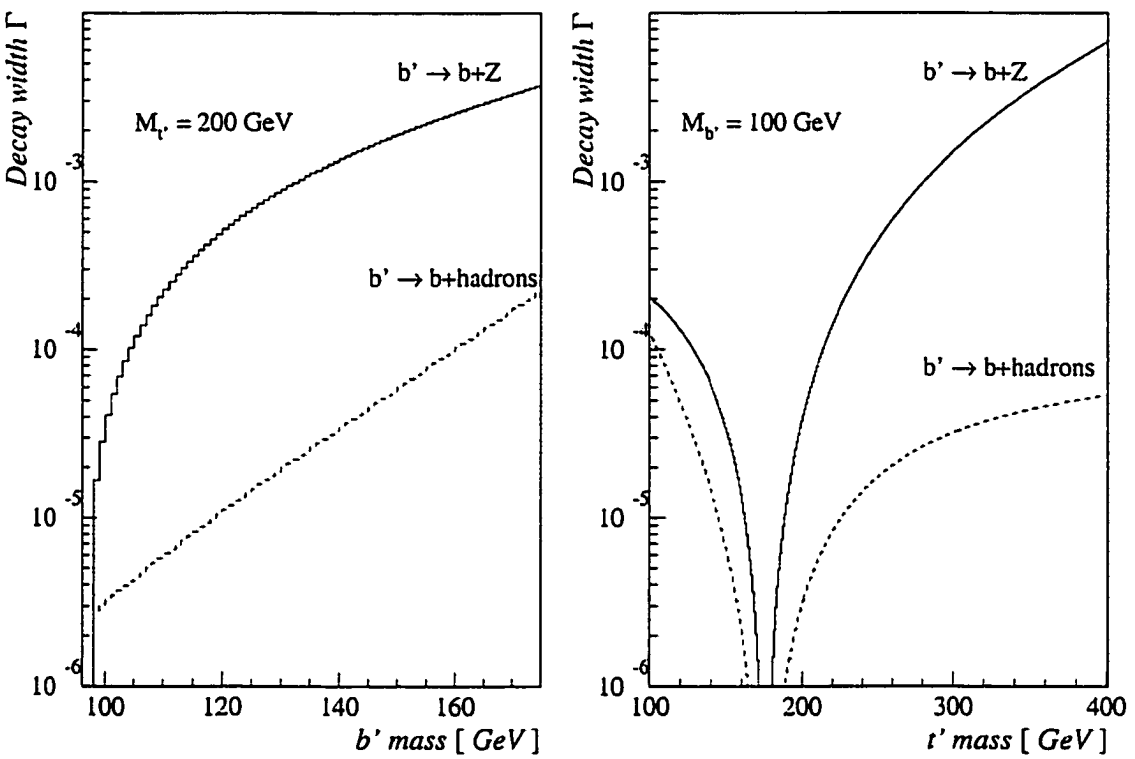

Figure 1.4: Theoretical prediction of the FCNC b' width in arbitrary units.

predominant CC decay, the dilepton and the lepton + jets (without b-tagging in the b' case) mass limits will apply with little modification to the lighter of b' or t'. In 1990, CDF used this argument to publish a lower limit on the b' mass of 72 GeV [15]. If the CC transition $b' \to cW^-$ is the exclusive b' decay, the lower mass bound of 128 GeV found in a DØ top quark search [22] also applies to the b' quark [1].

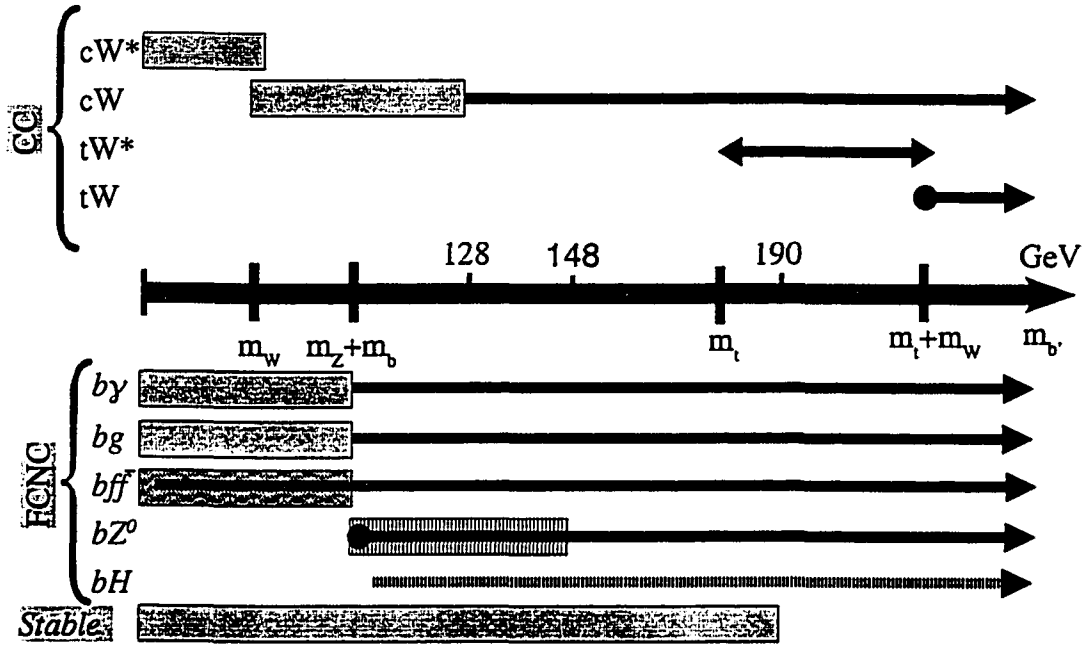

Figure 1.5: Summary of b' mass excluded regions. Light boxes indicate previously excluded regions. The box with vertical dashes indicates the previously excluded region for a long-lived quark.

Several experiments have searched explicitly for b' quarks decaying via FCNC. The most stringent limit comes from the DØ Collaboration, which searched in the $b'\overline{b'} \to \gamma g b\bar{b}$ and $b'\overline{b'} \to \gamma\gamma b\bar{b}$ channels, excluding a b' quark mass up to $m_Z + m_b$ for a FCNC branching fraction larger than 50% [19]. Previous lower mass limits, carried out at e^+e^- colliders, had been established by the AMY, VENUS, MARK II and LEP I collaborations [18].

CDF has excluded a long-lived b' quark with mass up to 148 GeV/c^2 and a lifetime of $\tau \approx 3.3 \times 10^{-11}$ sec, assuming $BR(b' \to bZ^0) = 100\%$ [20]. CDF has also carried out a

preliminary search for very long-lived charged massive particles [21]. These would be heavy quarks produced in $p\bar{p}$ collisions and that would leave the detector without decaying. The lower mass limit for a stable charge $-1/3$ quark is 195 GeV/c^2. These limits are only valid for the special case when the fourth generation is almost completely decoupled from the other three.

1.2.3 The b′ Signature

As mentioned before, under some reasonable assumptions on the sizes of the relevant Kobayashi-Maskawa matrix elements, the flavor-changing neutral current decay of b' can be the dominant decay mode. In this case, for a b' quark more massive than the Z^0 boson the theoretical prediction for $BR(b' \rightarrow bZ)$ is close to 100%. Therefore, we search for pair-produced b' quarks decaying via FCNC into bZ^0. One Z^0 decays into leptons and the other decays hadronically, as shown in Figure 1.6. The signature is two high transverse momentum (p_T) leptons from the Z^0 decay, two high-p_T jets from the second Z^0, and two b jets with p_T which scales with the b' mass being considered.

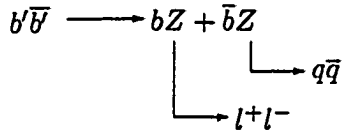

Figure 1.6: The b' decay mode under study.

Chapter 2

Experimental Apparatus

The Fermi National Accelerator Laboratory (Fermilab) in Batavia, Illinois, is a major facility dedicated to the study of high-energy physics. The laboratory holds a particle accelerator complex that includes the accelerator which provides the most energetic collisions per nucleon in the world, the Tevatron. The Tevatron produces proton (p) and antiproton ($\bar{p}$) collisions with a center of mass energy of $\sqrt{s} = 1.8$ TeV. The debris from the collisions are studied by two large multi-purpose particle detectors, the Collider Detector at Fermilab (CDF) and the DØ detector. The data used to search for $b'\overline{b'}$ production were collected with the CDF detector between 1994 and 1996.

2.1 Fermilab Accelerator Complex

In order to obtain beams of particles at high energies several stages are necessary. In a short description of this process, we will follow the path of the protons and antiprotons paths from their creation until their annihilation in the interaction point. A schematic diagram of the Fermilab accelerator complex is shown in Figure 2.1. The process starts with the production of H^- ions from a bottle of hydrogen gas. The ions are accelerated by a Cockroft-Walton electrostatic accelerator to an energy of 750 keV before being delivered to a 145 m linear accelerator, the Linac, which accelerates the ions to an energy of 400 MeV. The H^- ions pass through a copper foil and lose their two electrons. The resulting bare protons

are then injected into another accelerator, the Booster ring. The Booster, a synchroton with a radius of 75 m, boosts the protons to an energy of 8 GeV and gathers the protons into bunches. The proton bunches are extracted and delivered to the Main Ring.

The Main Ring is a 1 km radius synchroton with conventional magnets that is able to accelerate protons up to an energy of 150 GeV. After reaching 150 GeV, the protons are coalesced into a single bunch and injected into the Tevatron ring. The Tevatron is a synchroton accelerator with the same radius as the Main Ring and located just below it. The Tevatron uses superconducting magnets operating at the liquid helium temperature to produce the large magnetic fields required to attain 900 GeV energies per beam.

The Main Ring serves a second major purpose. It provides 120 GeV protons to be used in the production of antiprotons. The antiproton production is rather complex. The 120 GeV protons from the Main Ring are extracted and collide with a tungsten target. Antiprotons are selected from the resulting particles, focused with a lithium lens, and injected into the Debuncher. The Debuncher reduces the antiproton momenta spread using stochastic cooling. From the Debuncher, the antiprotons are transfered to the Accumulator, a ring that stores them at an energy of 8 GeV. Here, they are "stacked" at a rate of $\sim 4\times10^{10}$ antiprotons per hour, until approximately 10^{12} antiprotons have been collected. When a large number of antiprotons has been stored, six bunches of approximately 2×10^{11} protons are injected from the Main Ring into the Tevatron. Then, six bunches of $\sim 5.5 \times 10^{10}$ antiprotons from the Accumulator are transfered into the Main Ring and accelerated to an energy of 150 GeV. When this energy is reached, the antiproton bunches are injected into the Tevatron in the opposite direction of the protons. Many antiprotons are lost in the transfer process from the Accumulator to the Tevatron, and therefore the antiproton bunches at the Tevatron are composed of only $\sim 3 \times 10^{10}$ particles. The proton and antiproton beams travel in counter-rotating helical paths sharing the same beam pipe, while being accelerated up to 900 GeV. The $p\bar{p}$ collisions take place at the B0 and D0 interaction regions where the CDF and DØ detectors are located respectively. The transverse beam profile, in the collision region, is characterized by a gaussian distribution in the horizontal and vertical

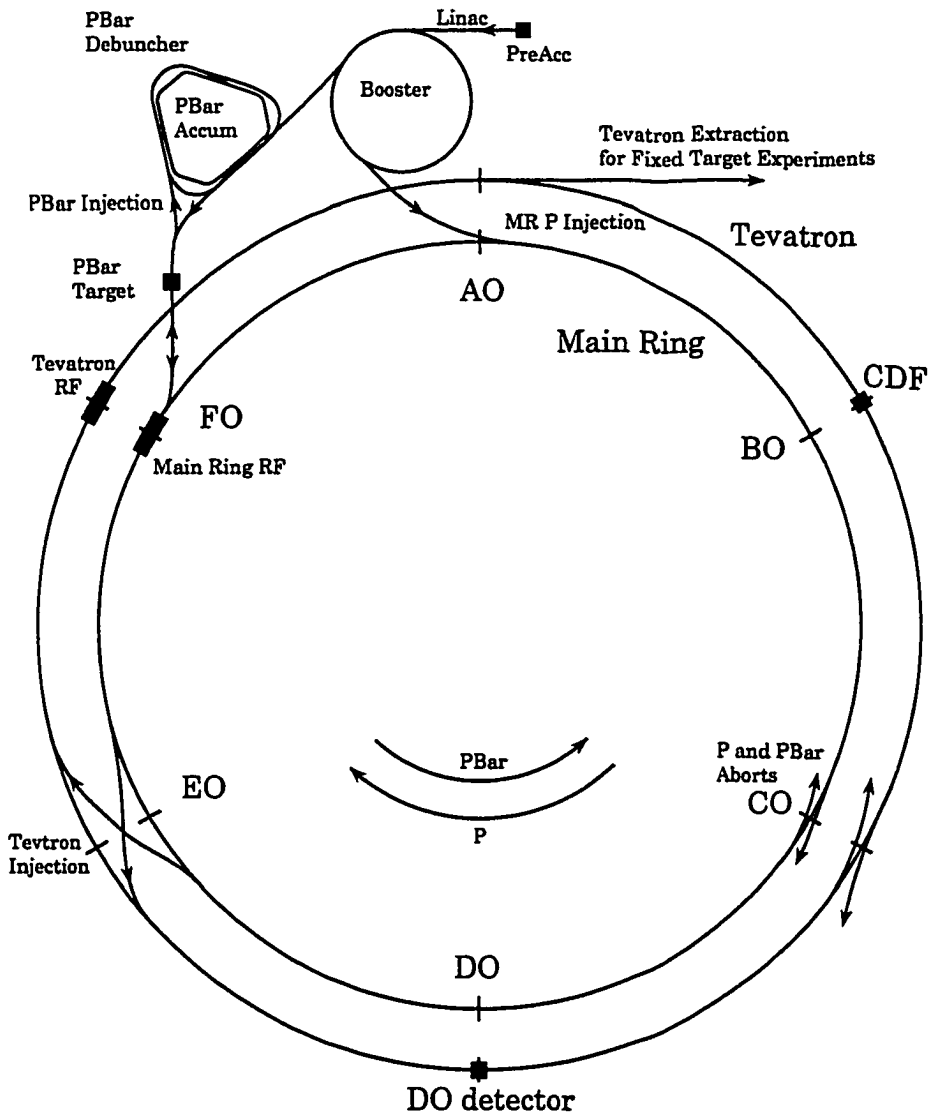

Figure 2.1: Schematic diagram of the Fermilab accelerator complex. The Main Ring and the Tevatron are both inside the same tunnel. The Tevatron is located below the Main Ring and both have the same 1 km radius [25].

directions with a width of $\sigma_x \approx \sigma_y \approx 35$ μm. The bunch crossing at the interaction region accurs at every 3.5 μs, corresponding to the Tevatron typical instantenous luminosity of 1-2 $\times 10^{-31}$ cm^{-2}s^{-1}.

2.2 Collider Detector at Fermilab

The Collider Detector at Fermilab is a multi-purpose apparatus designed to detect and study the particles produced in high-energy $p\bar{p}$ collisions. Extensive descriptions of the CDF detector can be found in the literature [26, 27]. Here, we will briefly describe the components that were the most relevant for this analysis. A schematic cross-section view of the CDF detector is shown in Figure 2.2. The detector has an overall forward-backward and cylindrical symmetry, and therefore only a quarter is shown. The CDF coordinate system uses (θ, ϕ, z), where the proton beam is in the z direction and θ and ϕ are the polar and azimuthal angles. The origin of the coordinate system is located at the nominal interaction point shown on the lower righthand corner of Figure 2.2. The detector pseudorapidity is defined in terms of the polar angle as $\eta = -\log[\tan(\theta/2)]$.

The CDF detector is composed of a variety of smaller specialized components. Most of these are integrated into the four major systems of the detector: tracking, calorimetry, muon chambers and trigger.

Surrounding the nominal interaction point and inside a 1.4 T solenoidal magnetic field, the silicon vertex detector (SVX), the vertex time projection chamber (VTX), and the central tracking chamber (CTC) provide tracking information. The SVX, positioned immediately outside the beampipe and inside the VTX, delivers precise track reconstruction in the plane transverse to the beam and is used to identify secondary vertices from the decay of b hadrons. The VTX is used to measure the position of the primary interaction vertex along the z axis. The CTC is a cylindrical drift chamber that covers the pseudorapidity range $|\eta| < 1.1$.

Outside the solenoid, electromagnetic (CEM, PEM, FEM) and hadronic (CHA, WHA, PHA, FHA) calorimeters surround the tracking volume and are used to identify

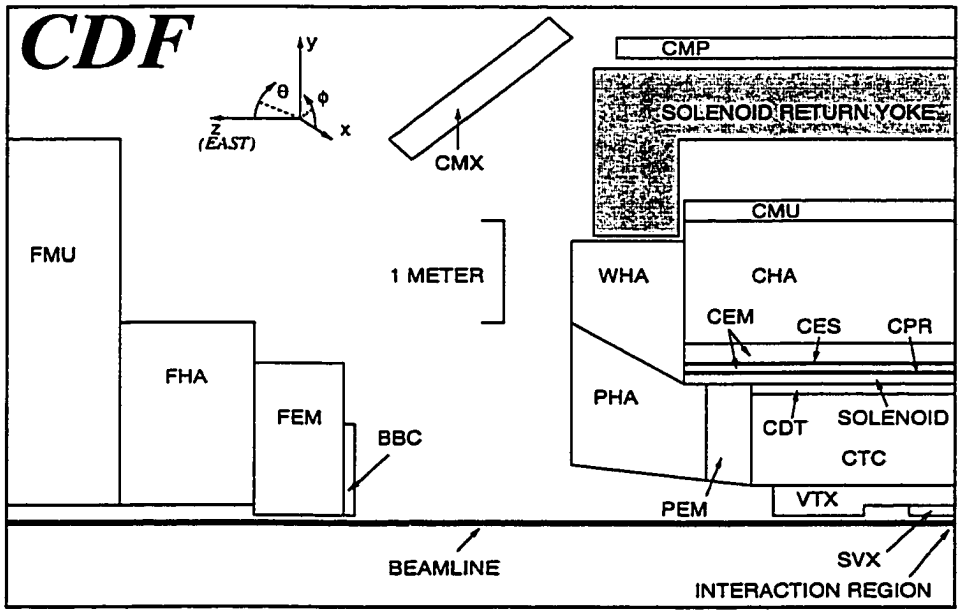

Figure 2.2: Schematic diagram of a quarter of the CDF detector. The interaction point is located at the lower righthand corner. The detector components are described in the text. The coordinate system used by CDF is also shown.

electrons, photons and jets over the range $|\eta| < 4.2$. Outside the calorimeters, three systems of drift chambers (CMU, CMP, CMX) in the region $|\eta| < 1.0$ provide muon identification. A three-level trigger selects the inclusive electron and muon events used in this analysis. Each of these systems is described in more detailed below.

2.2.1 Tracking System

The silicon vertex detector (SVX), the vertex time projection chamber (VTX), and the central tracking chamber (CTC) provide the tracking information at CDF. They are located inside a uniform 1.4 T magnetic field oriented along the beam direction that is produced by a superconducting solenoidal coil [28]. The coil is 3 m in diameter and 4.8 m in length with an overall radial thickness of 0.85 radiation lengths. The charged particles pass through the uniform solenoidal field with a helical trajectory. The transverse momentum of these particles is then derived from their trajectory curvature as measured by the tracking systems.

The SVX [29, 30, 31, 32] is a silicon micro-strip vertex detector that provides tracking information in the plane transverse to the beam and is used to identify secondary vertices from the decay of b hadrons. Positioned immediately outside the beryllium beampipe and inside the VTX, the SVX is the tracking detector closest to the interaction point. The detector is composed of two similar barrels aligned end-to-end along the beam pipe and symmetrically positioned relative to the nominal interaction point, $z = 0$. One such barrel is shown in Figure 2.3. The total active length of the detector is 51 cm, corresponding to a pseudorapidity coverage of $|\eta| < 1.9$. Since the actual $p\bar{p}$ interaction position is distributed around the nominal interaction point according to a gaussian distribution of width ~ 30 cm, the SVX has a geometrical acceptance for $p\bar{p}$ collisions of roughly 60%.

Each barrel consists of four layers of silicon micro-strip detectors position at a radii of 2.86, 4.26, 5.69 and 7.87 cm from the beam axis. The layers are divided into twelve azimuthal wedges of 30°, each housing one ladder with silicon detectors. Each ladder accomodates three single-sided silicon detectors of 8.5 cm in length. The silicon detectors

have axial strips with a 60 μm pitch on the three inner layers and 55 μm pitch on the outermost layer. The resolution for a single hit in the SVX detector is 13 μm, while the track impact parameter in the $r-\phi$ plane relative to the beam position can be measured with a precision of 17 μm. This good resolution allows the detection of secondary vertices from b hadron decays. For this reason, the SVX has become an essential tool in the quest for new physics. The impact parameter information provided by the SVX is used in this thesis in the algorithm that allows the identification of the b hadrons from the b' quark decay. The SVX tracking is done in conjunction with the information from the CTC.

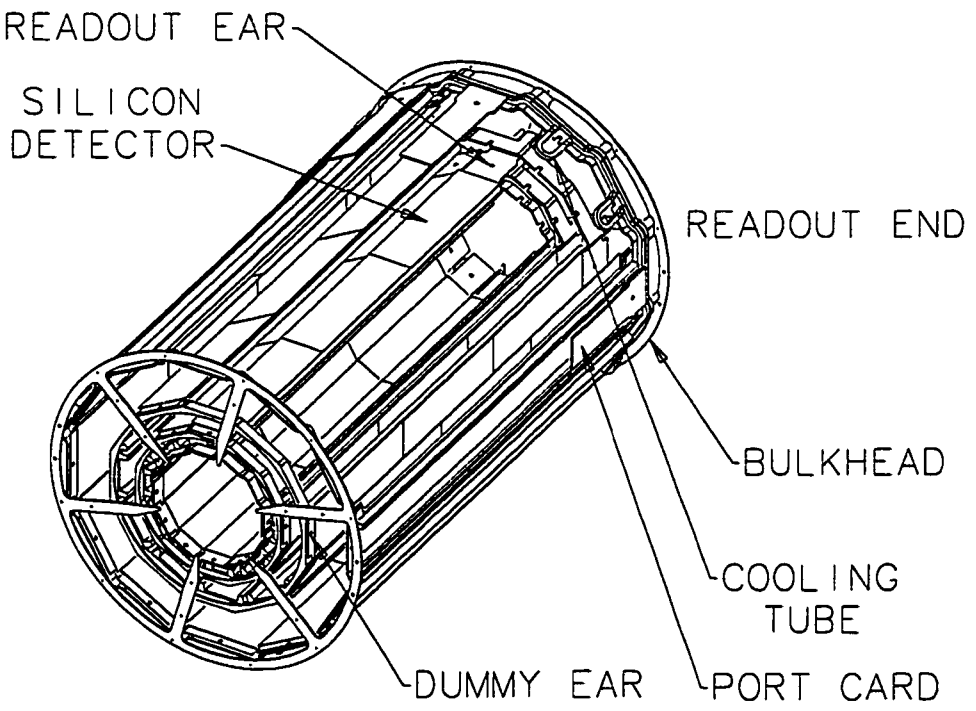

Figure 2.3: Diagram of one SVX barrel.

The Vertex Time Projection chamber (VTX) [33] is used to measure the position of the primary interaction vertex along the z axis. The VTX, with a 8 cm inner radius and 22 cm outer radius, lies between the SVX and the CTC. It covers the region in z between $z = \pm 1.4$ m corresponding to a pseudorapidity $|\eta| < 3.2$. The detector consists of octagonal

time projection chamber modules with radial wires and it is capable of finding the event vertex to within ± 1 mm. The event primary vertex distribution, as measured by the VTX, is described by a gaussian of width ~ 30 cm.

The Central Tracking Chamber (CTC) [34] is a large cylindrical drift chamber that covers the pseudorapidity range of $|\eta| < 1.1$. It is 3.2 m long in the z-direction, centered at $z = 0$, with an inner radius of 31.0 cm and an outer radius of 132.5 cm. It consists of 84 concentric cylindrical layers of sense wires that are grouped into nine superlayers. Five of the superlayers are called axial superlayers and contain twelve layers of sense wires parallel to the z axis. These are interleaved with four stereo superlayers each of which contain six layers of sense wires tilted $\pm$ 3° with respect to the beam axis. Figure 2.4 shows a diagram of the CTC endplate featuring the nine superlayer geometry. The superlayers are divided into cells tilted 45° relative to the radial direction to compensate for the Lorentz angle of the ionization drift velocity. This gives electron drift trajectories perpendicular to the radial direction so that the maximum drift distance is less than 40 mm, corresponding to a drift time of about 800 ns. The gas mixture used is argon-ethane-alcohol in a 49.6%:49.6%:0.8% proportion and the drift field is $\sim$ 1350 V/cm. The axial superlayers provide information about track momentum in the r-ϕ plane. The stereo layers allow for the reconstruction of the track momentum along the z direction, and therefore, together with the axial layers, provide tracking in three dimensions. The CTC measures momentum with a resolution of $\delta p_T/p_T = 0.002\ \text{GeV}^{-1} \cdot p_T$ without beam constraint or SVX information.

2.2.2 Calorimeters

Electromagnetic and hadronic calorimeters are positioned outside the tracking chambers and the solenoid, covering 2π in azimuth and $|\eta| < 4.2$ in pseudorapidity. They are divided into three major $|\eta|$ regions: central, endplug, and forward. In each region the electromagnetic calorimeter precedes the corresponding hadron calorimeter with respect to the nominal interaction point. The calorimeters are segmented in azimuth and pseudora-

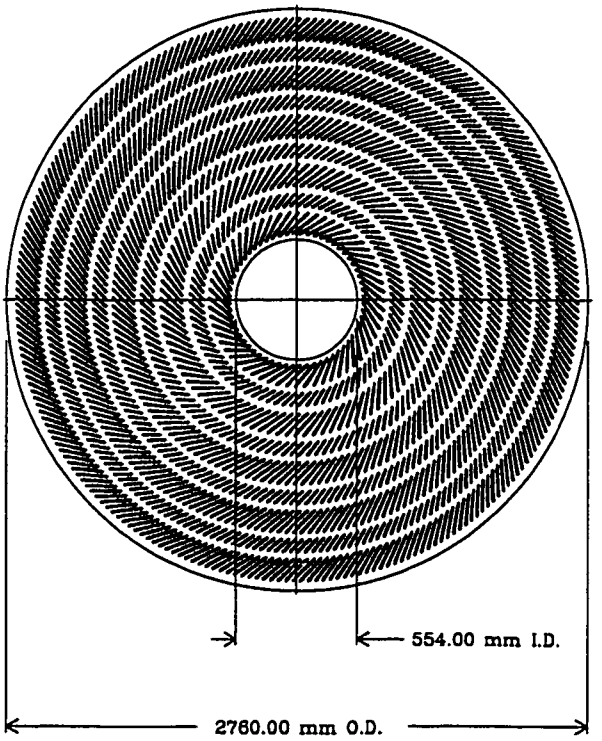

Figure 2.4: Diagram of CTC endplate emphasizing the nine superlayers.

pidity in a projective tower geometry that points back to the interaction point. Some of the calorimeters' characteristics are summarized in Table 2.1.

The central electromagnetic calorimeter (CEM) [35, 36, 37, 38, 39] is divided projective towers assembled into wedges as shown in Figure 2.5. Each tower is 15° wide in azimuth and 0.1 units wide in η. The towers are composed of alternating layers of lead and scintillator with a total thickness of 18 radiation lengths. The energy resolution is $\sigma(E)/E = 13.5\%/\sqrt{E \sin\theta}$ where E is measured in GeV. In each CEM tower, wire proportional strip chambers (CES) are located at the depth corresponding to the approximate shower maximum ($6 \cdot X_0$). The CES provides shower shape and position information in both z and r-ϕ. Proportional chambers (CPR) are located between the solenoid and the CEM. They sample the early development of electromagnetic showers in the solenoid coil. The CPR measures only the r-ϕ position of showers.

The central hadronic calorimeter (CHA) [40] is located immediately behind the CEM and is contained in the same physical wedges. It shares the same tower geometry and segmentation as the electromagnetic calorimeter. The wall hadronic calorimeter (WHA) complements the CHA as shown in Figure 2.2. The WHA has a significantly different shape because it covers the edge of the cylindrically shaped central region. Together, the CHA and the WHA provide hadronic coverage in the region $|\eta| < 1.3$. Both calorimeters are made up of alternating layers of iron and plastic scintillator. Their energy resolution and absorption thickness are given in Table 2.1.

The plug electromagnetic calorimeter (PEM) [41] and the plug hadronic calorimeter (PHA) cover the polar angle region between roughly 10° and 30° with respect to the beamline. They are located immediately next to the central calorimeters extending the total coverage in the central region to $|\eta| < 2.4$. The plug calorimeters are composed of two identical modules located on each end of the CDF detector as shown in Figure 2.2. The tower size in the plug is 5° wide in ϕ and 0.1 units wide in η. Both the PEM and PHA use the same projective geometry and segmentation. The active region is gas proportional chambers with a 50/50 mixture of argon-ethane gas. The proportional tube arrays are in-

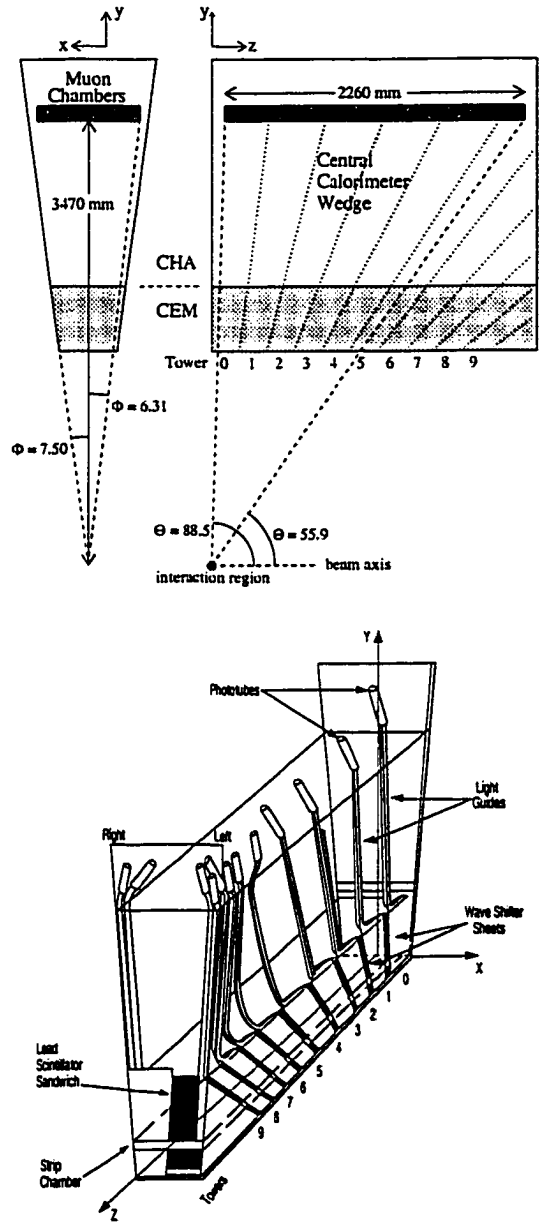

Figure 2.5: Schematic of a single central calorimeter wedge. Each wedge is composed of 10 towers. A single tower covers a region of $\Delta\eta = 0.1$ and $\Delta\phi = 15°$. Wire proportional strip chambers are located at shower maximum. The top diagram shows the position of the central electromagnetic and hadronic calorimeter wedge relative to the interaction point and the central muon chambers. The z-axis corresponds to the beam axis, the x-axis to the azimuthal direction and the y-axis to the radial direction. The bottom diagram shows the details of the CEM light collection system.

Calorimeter Subsystem	Geometric Coverage η Range	$\Delta\eta \times \Delta\phi$ segmentation	Energy Resolution (GeV)	Absorption Thickness
CEM	$0.0 < \|\eta\| < 1.1$	$0.1 \times 15°$	$13.7\%/\sqrt{E_T} \oplus 2\%$	18 X_0
PEM	$1.1 < \|\eta\| < 2.4$	$0.09 \times 5°$	$22\%/\sqrt{E} \oplus 2\%$	18-21 X_0
FEM	$2.2 < \|\eta\| < 4.2$	$0.1 \times 5°$	$26\%/\sqrt{E} \oplus 2\%$	18 X_0
CHA	$0.0 < \|\eta\| < 0.9$	$0.1 \times 15°$	$50\%/\sqrt{E_T} \oplus 3\%$	4.5 λ_0
WHA	$0.7 < \|\eta\| < 1.3$	$0.1 \times 15°$	$75\%/\sqrt{E} \oplus 4\%$	4.5 λ_0
PHA	$1.3 < \|\eta\| < 2.4$	$0.09 \times 5°$	$106\%/\sqrt{E} \oplus 6\%$	5.7 λ_0
FHA	$2.4 < \|\eta\| < 4.2$	$0.1 \times 5°$	$137\%/\sqrt{E} \oplus 3\%$	7.7 λ_0

Table 2.1: Summary of the CDF calorimeter properties. Tower segmentation is listed under the column $\Delta\eta \times \Delta\phi$. Energy resolutions are for incident electrons and photons in the electromagnetic calorimeters, and for incident isolated pions in the hadronic calorimeters. $E_T = E\sin\theta$ is the transverse energy. The symbol $\oplus$ signifies addition in quadrature. Thicknesses are given in radiation lengths (X_0) for electromagnetic calorimeters, and in interaction lengths (λ_0) for hadronic calorimeters.

terleaved with sheets of lead in the PEM and iron in the PHA. The absorption lengths and energy resolution are shown in Table 2.1.

The forward electromagnetic calorimeter (FEM) and the forward hadronic calorimeter (FHA) [42] are physically separated from the rest of the CDF detector. They are composed of two identical modules located in both the proton and antiproton beam directions, positioned approximately 6.5 m from the interaction point. The forward detectors cover the small angle region between 10° and 1.7° relative to the beamline, extending the calorimeter coverage up to $|\eta| < 4.2$. Their construction and energy resolution are similar to the corresponding plug calorimeters.

2.2.3 Muon Detectors

Outside the calorimeters, three systems of drift chambers provide muon identification information. These are the central muon chambers (CMU), the central muon upgrade chambers (CMP) and the central muon extension chambers(CMX). The muon chambers are used to identify muons and make a crude measurement of their transverse momentum

Chamber	Geometric Coverage η Range	Radial Position	Typical Resolution
CMU	$0.03 < \|\eta\| < 0.63$	347 cm $< r <$358 cm	250 μm
CMP	$0.00 < \|\eta\| < 0.55$	470 cm $< r <$550 cm	300 μm
CMX	$0.65 < \|\eta\| < 1.00$	440 cm $< r <$520 cm	250 μm
FMU	$2.40 < \|\eta\| < 4.20$	1.0 m $< r <$7.6 m	—

Table 2.2: Coverage and resolution of muon chambers.

at the trigger level. This information, combined with a matching extrapolated CTC track, provides accurate muon transverse momentum measurement. The geometric coverage and position resolution for each chamber is summarized in Table 2.2. A fourth muon system located in the detector forward region, the forward muon chamber (FMU), was not used in this analysis, and therefore is not described here.

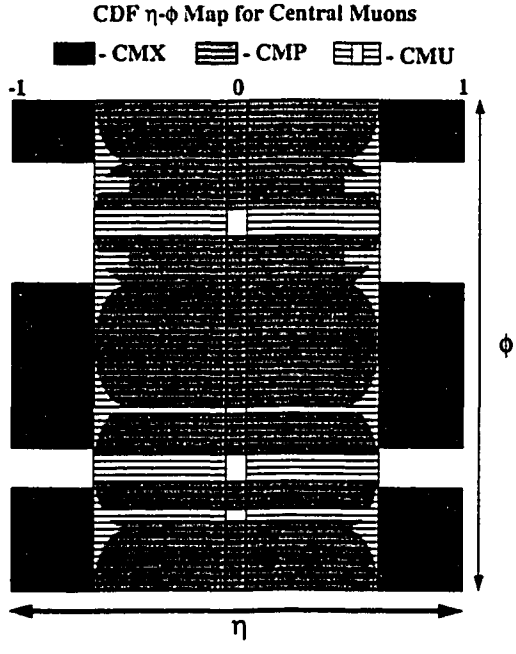

Figure 2.6: Coverage in the $\eta - \phi$ plane of the central muon chambers used in this analysis. These are the CMU, the CMP and the CMX chambers.

All three muon systems consist of four-layer drift chambers. The CMU chambers

are located immediately outside the CHA and are segmented as $\Delta\eta \times \Delta\phi = 0.1 \times 12.6°$ corresponding to each 15° wedge of the CHA as shown in Figure 2.5. With its 4.5 interaction lengths (λ_0) of iron, the CHA acts as a hadron absorber for the CMU chambers. The CMP chambers are located behind an additional 0.6 m ($3.5\lambda_0$) of steel. This additional steel reduces the rate of hadronic punchthrough by a factor of 30. By requiring a positive identification by both the CMU and a CMP chambers, the number of fake muons can be significantly reduced. The muon chambers do not cover all the central region of the CDF detector resulting in some η and ϕ gaps as shown in Figure 2.6. The CMU system covers approximately 84% of solid angle for $|\eta| < 0.6$ while 63% is covered by the CMP. The CMU-CMP simultaneous coverage is 53%.

The CMX chambers extend muon coverage to the region $0.6 < |\eta| < 1.0$, covering 71% of the solid angle in that region. The position of the CMX is shown in Figure 2.2. The CMX drift chambers are arranged as four free-standing conical arches. Scintillators on both faces of the CMX provide trigger information.

2.2.4 Beam-Beam Counters

Minimum bias events account for almost all the $p\bar{p}$ interactions at the Tevatron. These events are characterized by a large number of particles that leave the interaction point at small angles relative to the beamline. The luminosity of the accelerator delivered to CDF is monitored by measuring the rate of the minimum bias events using small-angle scintillating planes called beam-beam counters (BBC). The BBC are located on the front face of each of the forward electromagnetic calorimeters, covering the range $3.2 < |\eta| < 5.9$.

Coincidental signals from both BBCs are required to fall within a 15 ns window around the Tevatron bunch crossing signal. These provide the Level 0 CDF trigger and a measurement of the instantaneous luminosity. The total delivered luminosity at CDF is found by integrating this instantaneous luminosity over time. During the data taking run from 1994 to 1995, the total luminosity at CDF was measured to be 87.8 ± 3.6 pb^{-1}.

2.2.5 *Trigger System*

The event rate delivered by the Tevatron ($\sim$ 280 kHz) is too large for all events to be recorded and processed by the CDF online data acquisition system. CDF uses a three-level trigger system, to reduce the rate of events to a manageable level ($\sim$ 6 Hz) while maximizing the selection of interesting events. Each of the trigger levels consists of a logical OR of a number of triggers designed to find several types of interesting events. Each successive trigger level is more sophisticated and takes a longer time to reach a decision but processes a smaller number of events. The CDF Level 1 and Level 2 triggers are implemented in hardware, while the Level 3 trigger is implemented in software which allows more flexibility.

The hardware implementation of the Level 1 trigger allows for a quick decision on whether to process the event any further. The decision is made within the $3.5\mu s$ between bunch crossings, to minimize the amount of deadtime, *i.e.* time during which the detector does not acknowledge new interactions. The Level 1 triggers relevant for this analysis are the central muon and calorimeter triggers. These select events with muon tracks in the central muon chambers or significant calorimeter energy for the electron triggers. The three Level 1 central muon triggers use fast outputs from the CMU, CMP, and the CMX. They require a pair of hits in two parallel muon drift tubes. No tracking information is used at this level. The calorimeter triggers use fast outputs from the central calorimeters. In these triggers, the energy in the electromagnetic and hadronic calorimeter are separately summed into trigger towers, defined as $\Delta\eta \times \Delta\phi = 0.2 \times 15°$. These towers are required to have an energy above a given threshold. For a typical instantaneous luminosity of 10×10^{30} cm^{-2} s^{-1}, the Level 1 trigger reduces the event rate from approximately 280 kHz to $\sim$ 1 kHz.

The Level 2 trigger implements more sophisticated algorithms than Level 1 by making more extensive use of trigger signals coming from the calorimeter, tracking, and muon systems. A hardware calorimeter-cluster finder searches for a seed tower above a certain threshold and then adds in neighboring towers which are above a lower threshold. The E_T, mean ϕ, and mean η are calculated for each cluster. The central fast tracker (CFT) [44] is a hardware processor that uses information from the five axial CTC superlayers to iden-

tify high-momentum tracks in r-ϕ. The CFT is able to measure the transverse momentum with a resolution of $\delta P_T/P_T \approx 0.035\ \mathrm{GeV}^{-1} \cdot P_T$, and has an efficiency of $93.5 \pm 0.3\%$ for tracks with p_T above 10 GeV/c. Track segment information, including azimuthal position and p_T, from the CMU, CMP and CMX chambers is also available. Dedicated hardware extrapolates tracks found by the CFT to the CEM calorimeter clusters and to the muon chamber segments, forming electron and muon candidates respectively. For flexibility, the final Level 2 decision is made in a programmable module. Depending on the complexity of the event, the Level 2 trigger processing can take from ~ 20 μs up to hundreds of microseconds. During this time, the detector ignores any subsequent crossing. For a typical instantaneous luminosity of 10×10^{30} cm^{-2} s^{-1}, the Level 2 trigger incurs a deadtime of about 4%, and outputs events at a rate of aproximately 20 to 35 Hz.

The Level 3 trigger is a fully software-based trigger which runs on a farm of Silicon Graphics processors. It bases its decision on data read out from the entire detector. It executes a simplified version of the offline event reconstruction code, including calorimeter clustering and tracking. All events that pass the Level 3 trigger are stored on 8 mm magnetic tapes with a typical output rate of about 5-8 events per second. The Level 3 trigger and the DAQ incur a dead time of about 10%.

Chapter 3

Event Selection

In this analysis, we search for pair-production of b' quarks that decay by FCNC into bZ^0, where one Z^0 decays into e^+e^- or $\mu^+\mu^-$ and the other decays hadronically. These events contain two high transverse momentum (p_T) leptons from the Z^0 decay, two high-p_T jets from second Z^0 , and two b-jets whose p_T scales with the b' mass. We select events satisfying a high-p_T lepton trigger and containing a well-identified muon or electron in the central region. Inclusive $Z^0 \to e^+e^-$ and $Z^0 \to \mu^+\mu^-$ samples are selected by requiring one primary lepton that satisfies tight lepton identification cuts and a second lepton satisfying looser identification cuts, with a dilepton invariant mass close to the Z^0 mass. From these events, we define as our b' signal sample those with three or more jets in which at least one jet is identified as corresponding to a b quark.

In this chapter we describe in detail the requirements imposed on our data. In the first section, we define the inclusive high-p_T electron and muon samples which are the starting point of the analysis. The second section describes the Z^0 selection in both the electron and muon channels, including the lepton identification requirements. Finally, we present the jet selection criteria including the b-tag requirement, and the optimization studies that motivated them. A detailed discussion of the background processes will be presented in Chapter 6.

3.1 Data Sample

This search uses the data resulting from $p\bar{p}$ collisions at $\sqrt{s} = 1.8$ TeV collected with the CDF detector from 1994 to 1995[1] which corresponds to an integrated luminosity of $\int \mathcal{L}dt = 87.8 \pm 3.6$ pb^{-1}. The data set consists of events that passed the inclusive high-p_T central electron and muon triggers and is similar to the one used for the CDF top analysis.

3.1.1 High-p_T Electron Sample

Electrons produce a unique signature in the CDF detector. They are distinguished by a cluster of electromagnetic energy with most of the energy deposited in a single electromagnetic tower. In the case of central electrons, a CTC track points to the cluster and the shower profile is mapped by the proportional strip chambers (CES) inside the calorimeter. This additional information results in a better identification of central electrons as compared to plug electrons. The electron signal is characterized by a set of variables, described briefly below:

E_T Transverse energy deposited in the electromagnetic calorimeters towers associated with the cluster to which the track points.

P_T Transverse momentum of the track associated with the electromagnetic cluster. The momentum is measured from the track curvature in the CTC.

E_{had}/E_{em} The ratio of energy deposited in the hadronic calorimeters (CHA or WHA) to the electromagnetic calorimeters (CEM or PEM) in the towers corresponding to the electron cluster.

E/P The ratio of the calorimeter energy in the cluster to the total track momentum as measured by the CTC.

[1]The 1994-1995 CDF data collection period is known as Run 1b.

$|\Delta x|$ The distance in the $r-\phi$ plane between the CES shower position and the extrapolated CTC track. Only for CEM electrons.

$|\Delta z|$ The distance in the $r-z$ plane between the CES shower position and the extrapolated CTC track. Only for CEM electrons.

χ^2_{strip} The χ^2 from the comparison between the CES shower profile and the expectation from test beam electron data. Only for CEM electrons.

L_{shr} Comparison of the lateral shower profile in the CEM and expectations from test beam electron data. This variable is defined by

$$L_{shr} = 0.14 \sum_i \frac{E_i^{obs} - E_i^{test}}{\sqrt{(0.14\sqrt{E})^2 + \sigma^2_{E_i^{test}}}}$$

where the sum is over the towers adjacent to the seed tower, E_i^{obs} is the energy observed in tower i, E_i^{test} is the energy expected to be observed from test beam electron data, $\sigma^2_{E_i^{test}}$ is the uncertainty in E_i^{test} and $0.14\sqrt{E}$ is the calorimeter energy resolution.

$|z_v - z_e|$ The distance along the z-axis between the event primary vertex and the electron track. If there is more than one primary vertex (due to multiple interactions), this is the distance to the closest vertex.

I_{cal} Transverse calorimeter energy in a cone of radius $R = \sqrt{(\Delta\phi)^2 + (\Delta\eta)^2} = 0.4$ centered on the electron cluster but excluding the transverse energy associated to the electron cluster, $I_{cal} = E_T^{cone} - E_T^{electron}$.

The inclusive high-p_T central electron sample is collected using the multilevel trigger system[2] described in Section 2.2.5. The Level 1 trigger identifies a central electromagnetic cluster as an electron candidate if it has $E_T > 8$ GeV. The Level 2 central electron trigger requires an energy cluster with $E_T > 16$ GeV associated to a CTC track reconstructed by the Central Fast Tracker (CFT) with $p_T > 12$ GeV. The hadronic energy in the cluster is

[2]The Level 2 trigger described here is known has the CEM_16_CFT_12 trigger; and the Level 3 trigger is the ELEA_CEM_18.

required to be less than 12.5% the electromagnetic energy. Finally, the software trigger at Level 3 requires a central electromagnetic cluster with $E_T > 18$ GeV matched to a CTC track with $p_T > 13$ GeV plus some additional cuts. The inclusive high-p_T electron sample contains about 750,000 events.

3.1.2 High-p_T Muon Sample

Muons are minimum-ionizing particles that can traverse large amounts of matter before stopping. Therefore, the muon signature in the CDF detector is a high-p_T CTC track with little electromagnetic or hadronic energy deposited in the calorimeters that points to a track segment ("stub") in the muon chambers. Since the muon chambers do not cover all the CDF detector, we define a second muon category called CMIO. The CMIO muons, are consistent with a minimum-ionizing particle but were not detected by the muon chambers. These muons have a CTC track which does not extrapolate to a muon chamber, and they deposit very little energy in the calorimeters. The muon signal is characterized by the following set of variables:

P_T Transverse momentum of the muon track as measured in the CTC.

E_{had} Energy deposited in the hadronic calorimeter tower traversed by the muon track.

E_{em} Energy deposited in the electromagnetic calorimeter tower traversed by the muon track.

$|\Delta x|$ The distance in the $r - \phi$ plane between the muon chamber stub position and the extrapolated CTC track.

d_0 Impact parameter, defined as the distance of closest approach, in the $r-\phi$ plane, between the muon track and the beam axis, $r = 0$.

$|z_v - z_\mu|$ The distance along the z-axis between the event primary vertex and the muon track. If there is more than one primary vertex (due to multiple interactions), this is the distance to the closest vertex.

I_{cal} Transversed calorimeter energy in a cone of radius $R = \sqrt{(\Delta\phi)^2 + (\Delta\eta)^2} = 0.4$ centered on the muon but excluding the transverse energy in the calorimeter tower transversed by the muon.

The CDF muon detector system has a rather complex geometry, resulting in a correspondingly complicated trigger system. The muon candidates are categorized by the name of the muon chamber that detected them. Muons with stubs in both the CMU and CMP chambers are called CMUP. Muons reconstructed in only one of the chambers are called CMU, CMP or CMX.

The events are required to pass the Level 1 muon triggers and at least one of the Level 2 triggers listed in Table 3.1. The Level 2 triggers require the stubs in the muon detectors to match a CTC track reconstructed by the CFT, with $p_T > 12$ GeV. The match must be to within 5° in azimuthal angle. The CMUP triggers select events covered by both the CMU and CMP detectors. The candidates that fall in the η gaps of the CMP but cross the CMU chambers are selected with the CMNP triggers. The CMX triggers cover the higher-rapidity region, $0.6 < |\eta| < 1.0$. Several of the muon triggers have very high event rates and it was necessary to prescale the data. This means that only a percentage of the triggered events are kept. The prescale factor is set dynamically using an algorithm that is based on the instantaneous luminosity during data taking. The b' events are expected to have a large number of jets; therefore we have used triggers that require the presence of a jet with $E_T > 15$ GeV in addition to the muon. These triggers help to recover some of the efficiency lost due to the prescaling. We do not use missing-energy triggers because these triggers contribute little to our acceptance and are difficult to model.

The Level 3 trigger requires a reconstructed CTC track with $p_T > 18$ GeV/c matched to a muon chamber stub. The distance between the extrapolated track and the muon stub, $|\Delta x|$ must be less than 10 cm for CMU or CMUP muons and 25 cm for CMX muons. The inclusive high-p_T muon sample contains about 570,000 events.

Trigger	Prescale	Data events	%
CMNP_CFT_12_5Deg_V*	0.40	343	12
CMUP_CFT_12_5Deg_V*	1.	1915	65
CMNP_JET*	1.	88	3
CMUP_JET*	1.	175	6
CMU_CMP_JET*	0.37	100	3
CMNP_CFT_12_5Deg_M*	0.25	402	14
CMUP_CFT_12_5Deg_M*	0.96	1751	60
CMX_CFT_12_5Deg_V*	0.43	543	18
CMX_JET*	1.	108	4
CMX_CFT_12_5Deg_M*	0.30	200	7
CMX_CFT_12_5Deg_E*	0.50	571	19

Table 3.1: List of high-p_T L2 muon triggers used. The second column shows the number of events and the percentage that passed the corresponding trigger after the Z^0 selection described in Section 3.2. The percentage is relative to the total number of Z^0 events.

3.2 Z^0 Selection

From the inclusive lepton sample described above, we select $Z^0 \to l^+l^-$ events. In order to increase the search sensitivity, we select Z^0 events using rather loose lepton identification requirements. Inclusive dielectron and dimuon samples are selected by requiring one primary lepton that satisfies tight lepton identification cuts and a second lepton satisfying looser identification cuts.

The events are required to be from a "good run", meaning that all the components in the detector were in good working condition [3]. The primary vertex of the event, $|z_{vertex}|$, is required to be within 60 cm along the beam axis of the nominal interaction position. This assures that the interaction occured close to the detector center and therefore that its products traversed the instrumented regions of the detector.

[3]CDF code flag used was: BADRUN = 15 or -1.

3.2.1 *Electron Channel*

We start by selecting a first electron detected by the central calorimeter (CEM) with $E_T \geq 20$ GeV. To ensure that the electron shower energy is well-measured we require that the shower position is within the fiducial region of the calorimeter. This region excludes the calorimeter boundaries and inactive towers[4]. A detailed description of this cut can be found in reference [46]. The fiducial cut efficiency is about 84% for central electrons.

This first electron is required to pass tight electron identification requirements on the variables defined in Section 3.1.1:

- $E_T \geq 20$ GeV
- $E_{had}/E_{em} \leq 0.05$
- $E/P \leq 1.8$
- track strip matching:
  - $|\Delta x| \leq 1.5$ cm
  - $|\Delta z| \leq 3.0$ cm
- $L_{shr} \leq 0.2$
- $\chi^2_{strip} \leq 10.0$
- $|z_v - z_e| \leq 5.0$ cm

These cuts ensure a large reduction of fakes due to charged hadrons. To increase the acceptance, we do not impose any energy isolation requirement on this first electron. A large source of background electrons is photon conversions to e^+e^- pairs in the detector material. The electrons from photon conversions are removed using an algorithm that is 0.907 ± 0.038 efficient [47]. The primary electron candidate is removed if there is a near by opposite-charged track passing the following cuts:

[4]The fiducial cuts are implemented by the CDF offline code subroutine FIDELE.

- The separation of the two tracks in the $r-\phi$ plane at the tangency point is $|\delta(r-\phi)| <$ 0.3 cm
- The difference in polar angle at the tangency point is $|\delta \cot\theta| < 0.06$
- The conversion radial position, after the cuts above, is $-20 < R_{conv} < 50$ cm

Often, the partner track of a conversion electron is missed. In this case, the primary electron is considered to be from a conversion and removed if the following conditions are met:

- The number of expected VTX hits is at least three.
- The ratio of observed VTX hits to the number expected is less than 0.2.

For events that have one high-P_T electron that passes all the cuts above, we require a second electron with $E_T \geq 10$ GeV that can be in the central or plug calorimeters. No other fiducial requirements are imposed. This second electron must satisfy the following loose electron identification criteria:

- $E_T \geq 10$ GeV
- $E/P < 2.0$ (if in the CEM)
- $E_{had}/E_{em} < 0.12$

Furthermore, in order to reduce hadronic backgrounds, this second electron must pass a calorimeter isolation requirement. The calorimeter transverse energy inside a cone of radius $\sqrt{\eta^2+\phi^2} = 0.4$ centered on the electron direction, excluding the electron transverse energy, must be less than 20% the transverse energy associated with the electron,

$$iso = \frac{E_T^{cone} - E_T^{electron}}{E_T^{electron}} < 0.2.$$

We accept events for the $Z^0 \rightarrow e^+e^-$ data sample if the reconstructed invariant mass of the identified electron pair is between 75 and 105 GeV/c^2. After this selection there are 6287 Z^0 events remaining. Figure 3.1 shows the η distribution for the second-leg electrons

of the events that have passed our Z^0 selection requirements. The events are distributed in the central and plug calorimeters as shown in Table 3.2. Only 8% of the events that have both electrons in the CEM have a second electron that fails the tight cuts. About 60% of the $Z^0 \rightarrow e^+e^-$ events have one of the electrons in the plug calorimeter. The forward calorimeter is not used in this analysis because its contribution to the signal acceptance is only about 3% and there is some concerns of large QCD backgrounds in that area of the detector. Figure 3.2 shows the Z^0-mass peak observed in the dielectron invariant mass distribution after all the Z^0 selection cuts have been applied to the data.

Observed $Z \rightarrow e^+e^-$ data events			
central - central		central - plug	total
tight Z	loose Z		
2410	197	3680	6287

Table 3.2: Number of observed events in the $Z^0 \rightarrow e^+e^-$ data divided by the second-leg electron calorimeter. The loose Z^0 column indicates the number of central Z^0 events in which the second electron did not pass the tight cuts but passed the loose ones.

3.2.2 Muon Channel

The dimuon selection starts by requiring one CTC track with $p_T \geq 20$ GeV/c that passed the high-p_T muon trigger and has a matching stub in the CMU or CMX muon chambers. These include the muons from the CMUP, CMU and CMX categories described in Section 3.1.2. To ensure that the track corresponds to a muon and to reduce backgrounds, we impose the muon identification criteria given below:

- $p_T \geq 20$ GeV/c
- $E_{em} \leq 2$ GeV
- $E_{had} \leq 6$ GeV
- $E_{em} + E_{had} \geq 0.1$ GeV

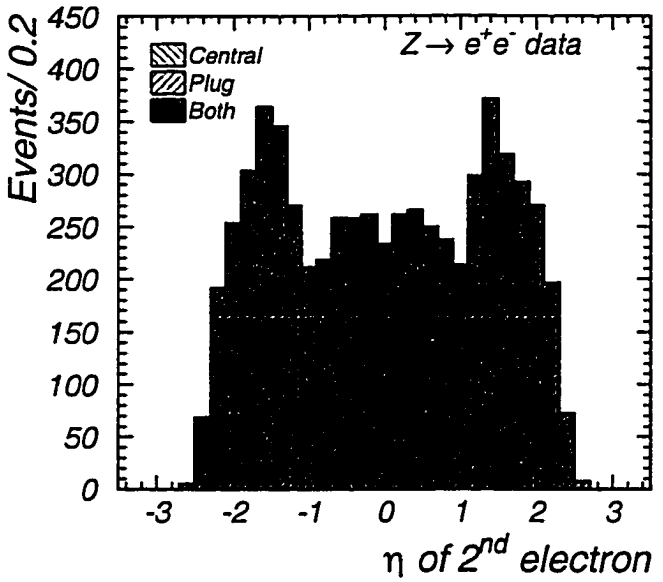

Figure 3.1: η distribution of the second-leg electron in $Z^0 \rightarrow e^+e^-$ events. The contributions from the two calorimeters used are indicated with different hashes.

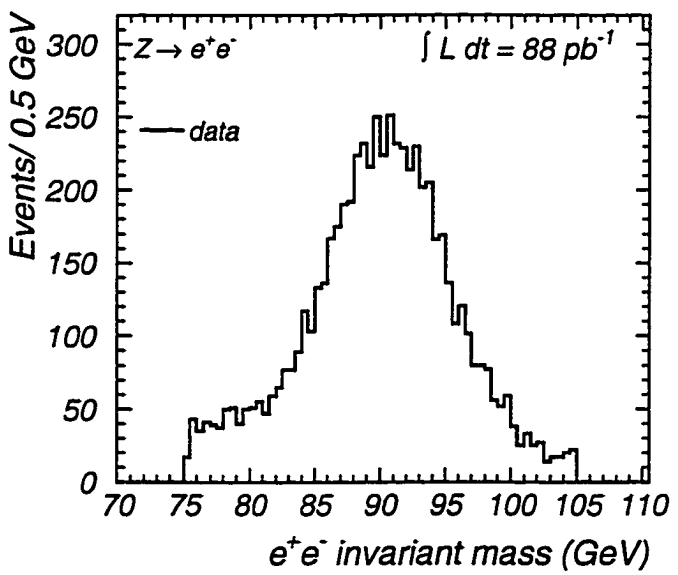

Figure 3.2: Dielectron invariant mass after Z^0 selection cuts.

- $|\Delta x| = 2.0$ cm (5.0 cm) in CMU (CMP and CMX)
- $d_0 \leq 0.3$ cm
- $|z_0 - z_v| \leq 5.0$ cm

For events that have one high-p_T muon that passes the above cuts, we require a second muon with $p_T \geq 10$ GeV/c. Besides the muon categories that were valid for the first muon, we accept other two looser categories of muons: the CMP and the CMIO muons. The lepton identification requirements for this second muon are less stringent than for the first muon. If it was detected by the muon chambers, the following criteria are applied:

- Muon type: CMU, CMP, CMUP or CMX
- $p_T \geq 10$ GeV/c
- $E_{had} \leq 10$ GeV
- $E_{em} \leq 5$ GeV
- $|\Delta x| \leq 5$ cm.

For CMIO muons, the identification requirements are more stringent because there is no confirmation from a muon chamber. The rapidity cut ensures that the track goes through most of the tracking chamber.

- $p_T \geq 10$ GeV/c
- $E_{had} \leq 6$ GeV
- $E_{em} \leq 2$ GeV
- $|\eta| \leq 1.2$

Similiarly to the electron case, a calorimeter energy isolation cut is imposed on the second muon. The muon is accepted if

$$iso = \frac{E_T^{cone} - E_T^{muon}}{P_T^{muon}} < 0.2,$$

where E_T^{cone} is the calorimeter energy in a cone of radius of 0.4 centered in the muon track, E_T^{muon} is the transverse energy found in the calorimeter tower associated with the muon track and P_T^{muon} is the muon transverse momentum.

We accept events if the reconstructed $\mu\mu$ invariant mass is between 75 and 105 GeV/c^2. After this selection there are 2940 Z^0 events remaining in the muon data sample. From these, 2904 have opposite-sign muons and 36 have like-sign muons. Figure 3.3 shows the invariant mass distribution of the 2940 Z^0 events. The events with CMIO muons compose a large percentage of the total number accepted, as shown in Table 3.3.

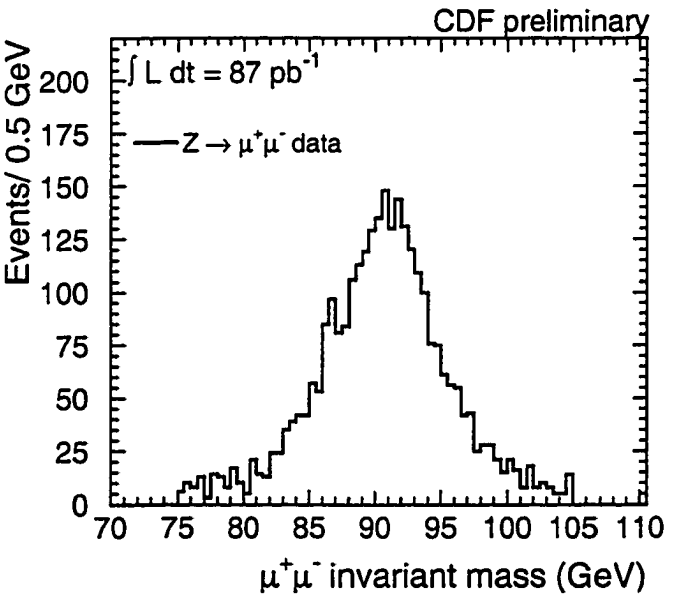

Figure 3.3: Dimuon invariant mass after Z^0 selection cuts.

Muon type	First Leg %	Second Leg %
CMU only	10	11
CMP only	N/A	12
CMUP	63	24
CMX	27	19
CMIO	N/A	34

Table 3.3: Distribution of the muon data events by muon category. The numbers are given in percentage of Z^0 events.

3.3 Jet Selection

Our b' signal contains four quarks in the final state, of which at least two are b quarks. In this analysis, quarks are identified as hadronic jets using a calorimeter energy clustering algorithm [48] with a cone size of $\Delta R = \sqrt{\Delta\eta^2 + \Delta\phi^2} = 0.4$. The algorithm begins by grouping pre-clusters of contiguous calorimeter towers with $E_T > 1$ GeV. Towers with $E_T > 0.1$ GeV inside a $\Delta R < 0.4$ cone centered on the pre-cluster are associated into a cluster. A new center for the cluster is calculated and an iterative procedure is performed until the cluster configuration is stable. The jet energy is the sum of the individual tower transverse energy within the cluster cone. The jet energy can be corrected for several effects: (*i*) calorimeter non-linearities, (*ii*) out-of-cone energy loss, (*iii*) loss of low-p_T tracks curled by the magnetic field, (*iv*) undetected energy from muons and neutrinos in the jet, (*v*) detector boundary effects, (vi) energy from the underlying event (soft interactions between spectator partons in the event). These corrections are more crucial for analyses where the best possible determination of the jet energy is important. In this analysis, these jet-corrections are not applied, which results in an underestimation of the actual parton energies by approximately 30%.

Since some of the jets can be merged, or lost due to inefficient coverage of the detector, we only require the presence of three jets in our Z^0 sample. In order to optimize our sensitivity to a b'-quark signal we make a jet selection that depends on the b' mass

being considered. Each event is required to have at least three jets within $|\eta| < 2.0$, two of which with $E_T > 15$ GeV. For b' masses above 120 GeV/c^2, the third jet is required to have $E_T > 15$ GeV. For $m_{b'} \leq 120$ GeV/c^2, the E_T requirement on the third jet is relaxed to $E_T > 7$ GeV since the b jets for b' masses near the $m_Z + m_b$ threshold have low momentum.

The p_T of the b' decay products is expected to increase with the b' mass. We define the variable $\sum E_T^{jets}$ as the summed transverse energy of jets with $E_T > 15$ GeV and $|\eta| < 2.0$. Motivated by the studies described in section 3.3.2, we require this quantity to scale with the b' mass according to the equation $\sum E_T^{jets} \geq m_{b'}c^2 - 60$ GeV. Figure 3.4 shows the $\sum E_T^{jets}$ distribution for ee and $\mu\mu$ events passing the 3-jet requirement for b' masses above 120 GeV/c^2. Also shown are the distributions expected from the main Standard Model background (Z^0 + jets)[5] and from the decay of a 150 GeV/c^2 b' quark[6]. The number of events passing each major selection criterion for each leptonic channel is shown in Table 3.4.

$m_{b'}$	$Z^0 \to e^+e^-$			$Z^0 \to \mu^+\mu^-$		
(GeV/c^2)	3 jets	$\sum E_T^{jets}$	b-tag	3 jets	$\sum E_T^{jets}$	b-tag
100	34	31	0	32	29	1
110	34	24	0	32	22	1
120	34	20	0	32	21	1
130	9	8	0	8	6	0
140	9	8	0	8	5	0
150	9	7	0	8	4	0
160	9	4	0	8	4	0
170	9	2	0	8	4	0
180	9	1	0	8	3	0
190	9	1	0	8	3	0
200	9	1	0	8	2	0
210	9	1	0	8	0	0

Table 3.4: Events observed in data after each main selection requirement in both the electron and the muon channels. The 3 jets requirement is different for $m_{b'} \leq 120$ GeV/c^2 and $m_{b'} > 120$ GeV/c^2 and the $\sum E_T^{jets}$ cut scales with the b' mass.

[5]The background is discussed in detail in Chapter 6.

[6]The signal Monte Carlo simulation is described in Chapter 4 together with the efficiencies and acceptance calculation.

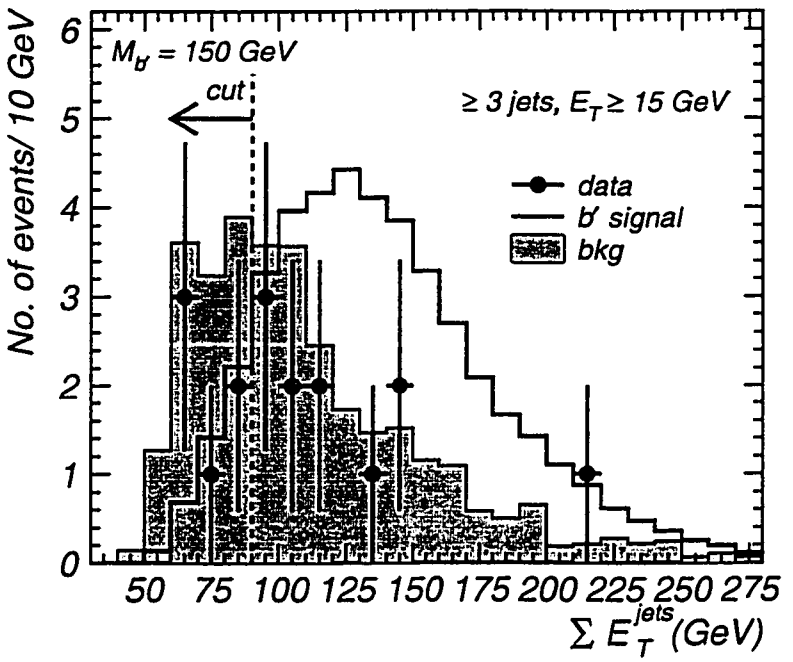

Figure 3.4: $\sum E_T^{jets}$ distribution for events with at least 3 jets with $E_T > 15$ GeV and $|\eta| < 2$, before the b-tagging requirement. The expected SM background is shown shaded. The expected signal event distribution for a b' quark mass of 150 GeV/c^2 is shown as a solid line. The vertical dashed line represents the $\sum E_T^{jets}$ cut for this specific b' mass. Events to the right of this line are accepted.

3.3.1 Silicon Vertex b-tag

A b-quark jet can be distinguished from other jets due to the relatively long lifetime of the b quark. With a lifetime of about 1.5 psec, a B hadron created in the high-p_T collision can travel a few millimiters before decaying. The displacement between the decay vertex and the event primary vertex can be measured by the Silicon Vertex Detector. This measurement provides a means to identify or "tag" b-quark jets. This identification is accomplished by the SVX b-tagging algorithm [49] developed for the top quark analyses.

Since a b' signal should be rich in b quarks, we require the events in the Z^0 sample that pass the above jet selection criteria to have at least one jet positively identified by the SVX b-tagging algorithm. A summary of the event statistics in our selection process is shown

in Table 3.4. We do not observe any events in the electron data sample after the final b-tag requirement, but there is one $\mu\mu$ event in which the highest-E_T jet is found to be consistent with a b-quark. This muon event passes all our selection criteria for $m_{b'} \leq 120$ GeV/c^2; however, it has a third jet with $E_T = 8.3$ GeV which fails the third-jet E_T requirement for larger b' masses.

The candidate event has the number 15532 and it is from run number 64275. Figures 3.5 and 3.6 show the CTC and calorimeter display for this event. The event passes the muon triggers that requires a central high-p_T muon and a CFT track (CMUP_CFT*) and the corresponding jet trigger (CMUP_JET*). The muon that fired the trigger was detected by both the CMU and CMP muon chambers and passes the tight muon identification cuts, while the second muon is a CMIO. The invariant mass of the two muons is 94 GeV, consistent with originating from a Z^0 decay. The two most energetic jets ($E_T(j_1) = 56.7$ GeV, $E_T(j_2) = 20.3$ GeV) have an invariant mass within our Z^0 mass window. So, an extra cut on the jets invariant mass would not reject the event. It really looks like an event with two Z^0 bosons! Some more information about this event is given in Table 3.5.

Run# 64275			Event# 15532		
	E_T (GeV)	p_T (GeV/c)	η	ϕ	charge
μ_1		38.8	0.257	1.09	-
μ_2		56.3	0.974	4.93	+
jet_1	56.7		-0.31	2.44	
jet_2	20.3		-0.16	5.04	
jet_3	8.3		-1.5	0.38	
$\sum E_T^{jets}$	77 GeV				
$m(\text{jet}_1, \text{jet}_2)$	97 GeV				
$m(\mu_1, \mu_2)$	94 GeV				
$\not\!\!E_T$	7.1 GeV				
z_{vertex}	-18 cm				
b-tag	jet_1				

Table 3.5: Characteristics of the muon event that passed the b' selection criteria.

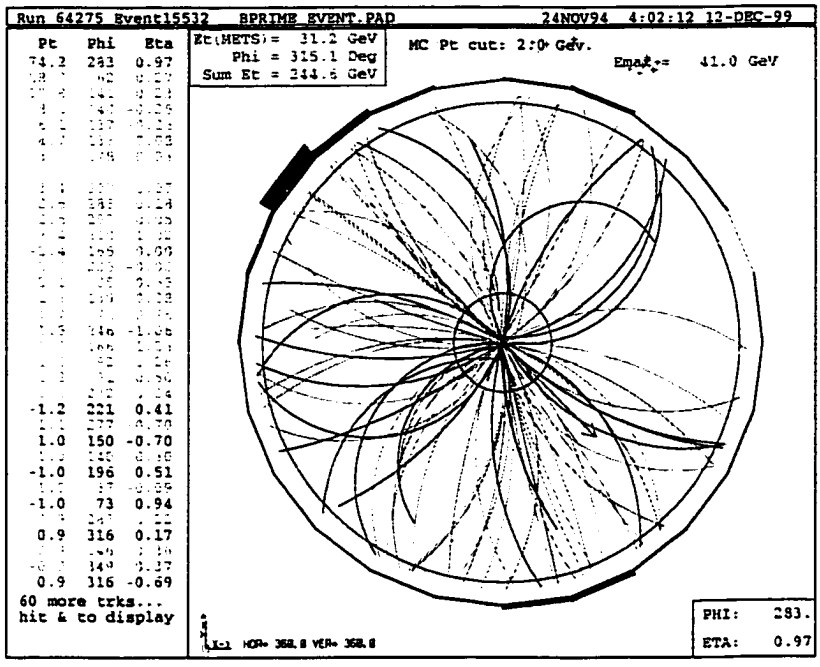

Figure 3.5: Central tracker image of b' candidate event.

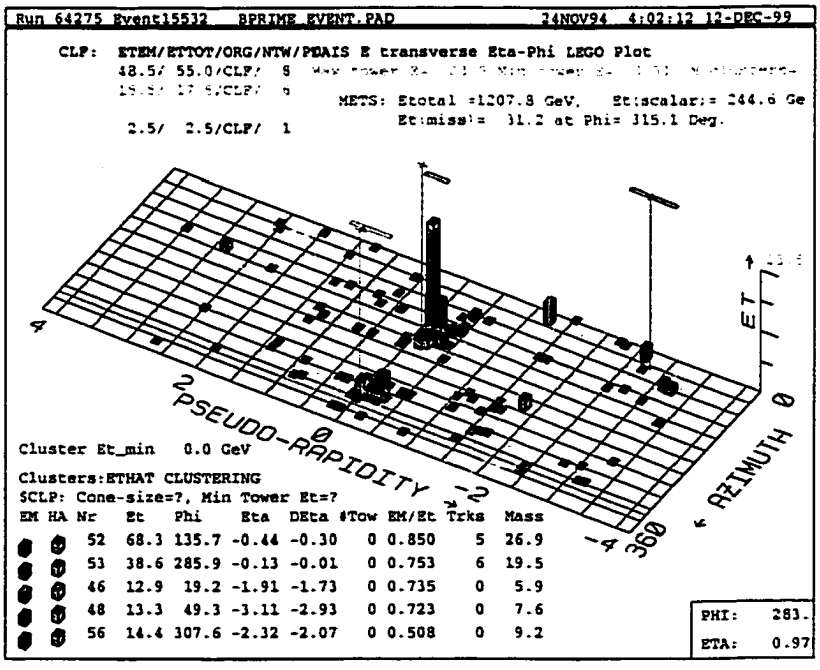

Figure 3.6: Calorimeter image of b' candidate event.

3.3.2 Cuts Optimization

Our selection criteria were motivated by a thorough study of $sgn/\sqrt{bkg}$ distributions. The b' signal Monte Carlo used in this calculation is described in Section 4.1. The background estimations are reported in Chapter 6. Figure 3.3.2 shows the $sgn/\sqrt{bkg}$ as a function of the $\sum E_T^{jets}$. The study was performed before and after the b-tag requirement, but subsequently to the other selection criteria. Each curve in the plot corresponds to a different b' mass. The arrows indicate were the $\sum E_T^{jets}$ cut is applied for a given mass. We show the results for masses from 100 GeV to 200 GeV. We observed that the $\sum E_T^{jets}$ cut improves the $sgn/\sqrt{bkg}$ independently of the b-tag requirement. We also observe that the b-tag boosts our sensitivity by at least a factor of two for almost every b' mass. In the case of a 100 GeV b' quark, the b-tag requirement actually results in a slightly lower $sgn/\sqrt{bkg}$, but we benefit from the fact that the background is reduced to almost zero. This way, we can calculate a limit without subtracting background and therefore are not affected by the uncertainties in the background estimation.

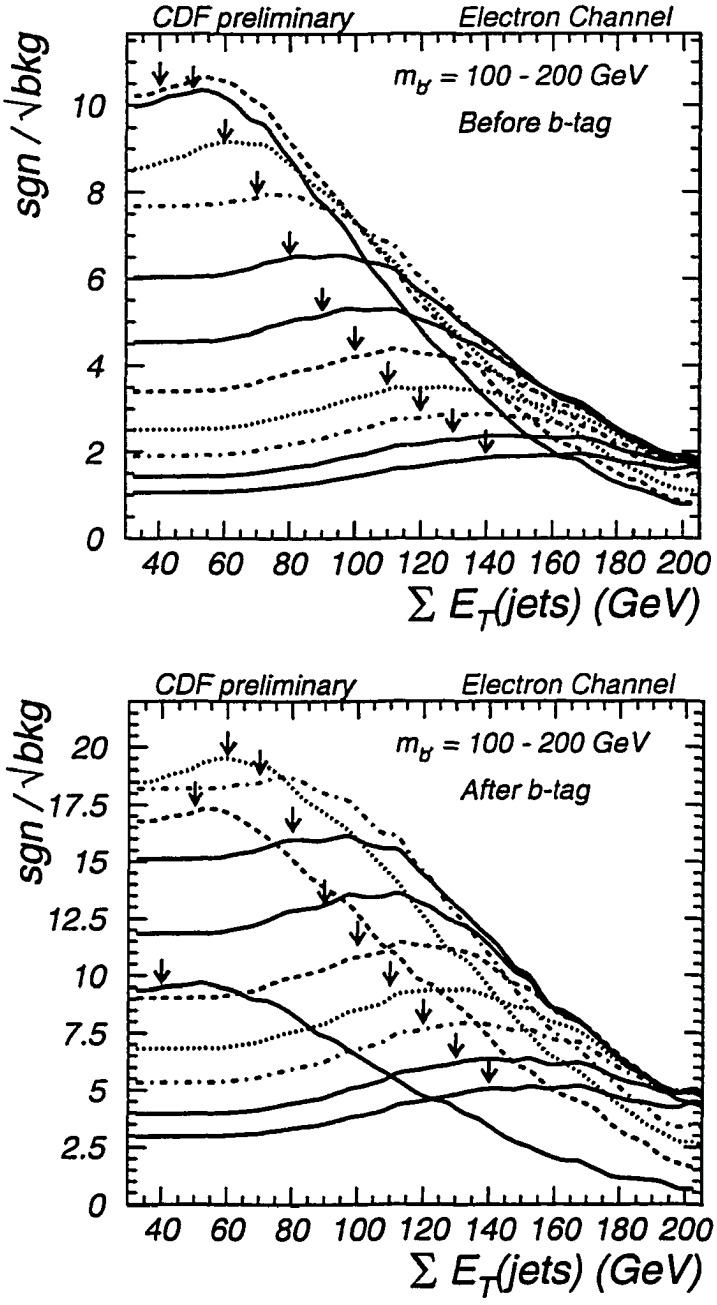

Figure 3.7: $sgn/\sqrt{bkg}$ as a function of $\sum E_T^{jets}$ for all b' masses. The arrows show the position of the $\sum E_T^{jets}$ cut; events to its right are accepted. The curves show b' masses in 10 GeV steps from 100 GeV to 200 GeV. The leftmost arrow corresponds to a 100 GeV b' while the rightmost arrow is for 200 GeV. Top: Calculation done after the 3-jet requirement and before the b-tag. Bottom: Calculation done after all selection besides the $\sum E_T^{jets}$cut. Both plots are normalized to the Run 1b luminosity.

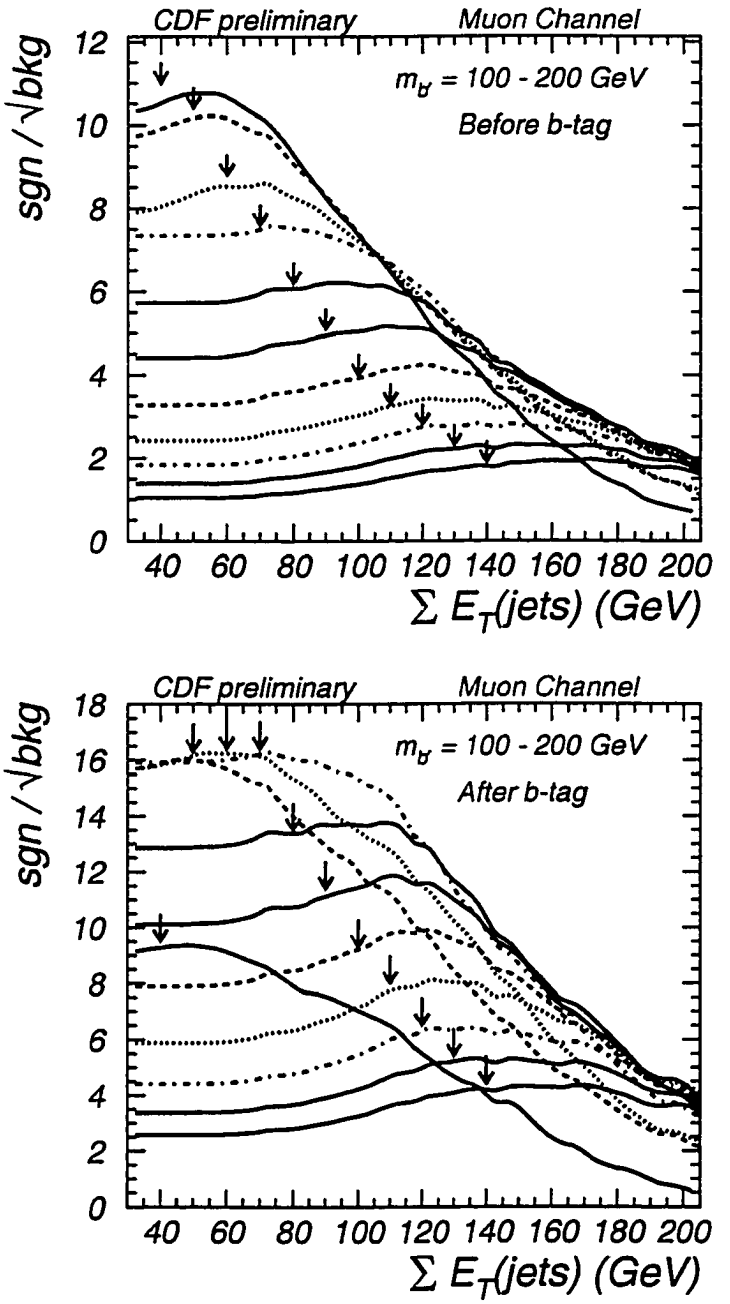

Figure 3.8: $sgn/\sqrt{bkg}$ as a function of $\sum E_T^{jets}$ for all b' masses. The arrows show the position of the $\sum E_T^{jets}$ cut; events to its right are accepted. The curves show b' masses in 10 GeV steps from 100 GeV to 200 GeV. The leftmost arrow corresponds to a 100 GeV b' while the rightmost arrow is for 200 GeV. Top: Calculation done after the 3-jet requirement and before the b-tag. Bottom: Calculation done after all selection besides the $\sum E_T^{jets}$cut. Both plots are normalized to the Run 1b luminosity.

Chapter 4

Acceptance and Efficiencies

This section describes the computation of the fraction of $b'\overline{b'}$ events that can be identified using the selection criteria from the previous chapter. The acceptance and detection efficiencies calculation is factorized into independent terms as follows:

$$A \cdot \epsilon = A_Z \cdot \epsilon_Z \cdot \epsilon_{jet} \cdot \epsilon_{b-tag}, \tag{4.1}$$

where A_Z is the detector geometrical acceptance for a $Z^0 \to l^+l^-$ from a $b'\overline{b'}$ event, ϵ_Z is the detection efficiency for the Z^0, ϵ_{jet} is the overall jet requirement efficiency and ϵ_{b-tag} the efficiency for b-tagging at least one jet in the event. These acceptance and detection efficiencies are determined from a combination of data and Monte Carlo simulation.

4.1 Signal Monte Carlo

We used the HERWIG v5.6 Monte Carlo generator program [50] to study the acceptance of the detector and the kinematic selection cuts. The standard version of HERWIG does not have the possibility to generate the $b'\overline{b'} \to bZ^0\overline{b}Z^0$ process. Since both top and b' are produced by the same hadronic processes of gluon-gluon fusion and $q\overline{q}$ annihilation, we have generated top quarks as if they were b' quarks. The subroutine that handles the standard charged-current decays of heavy quarks was replaced with another subroutine that allows 2-body neutral-current decays of top (our b') into γ and gluons [51]. The subroutine was then modified to make the $b' \to bZ^0$ neutral-current decay. One Z^0 is required to decay

into muons or electrons while the other is allowed to decay through any available decay channel. The CLEO QQ Monte Carlo program [53] is used to decay the b quarks generated by HERWIG. This step is necessary to ensure the proper lifetime and decay of the b hadrons. These events are passed through a fast simulation of the CDF detector[1]. Each event was subjected to the same selection requirements as the data.

We generated Monte Carlo samples of $b'\overline{b'} \rightarrow bZ\bar{b}Z$ with the MRSD0′ structure functions [52]. We made samples at twelve different b' masses between 100 and 210 GeV/c^2 in steps of 10 GeV/c^2. The sample size varies from 60,000 ($m_{b'}$= 100 GeV) to 30,000 events in order to allow a similar statistical uncertainty for all b' masses after event selection requirements have been imposed. These large samples led to a small Monte Carlo statistical error and allowed a comprehensive study of the systematic uncertainties.

4.2 Z^0 Acceptance

The Z^0 acceptance is the geometrical acceptance for detecting a $Z^0 \rightarrow l^+l^-$ decay from the $b'\overline{b'}$ event. This acceptance includes the z_{vertex} efficiency, the efficiency for having both leptons in the fiducial region of the detector, and the Z^0 mass cut efficiency.

4.2.1 z_{vertex} Efficiency

As we saw in Chapter 3, we require the primary vertex of the event to be within 60 cm of the nominal interaction position, $|z_{vertex}| < 60$ cm, in order to keep the events well-contained in the fiducial region of the detector. The event primary vertex distribution is described by a gaussian of width $\sigma_z = 29$ cm and is not expected to vary with the physics process being studied. Therefore, the b' Monte Carlo samples, used to determine the geometrical acceptance, were simulated with a primary vertex drawn from a truncated gaussian with $\sigma_z = 29$ cm and the requirement that $|z_{vertex}| < 60$ cm. The z_{vertex} efficiency was obtained from an independent CDF data sample.

[1]We used the QFL′ v3.61 program for the CDF detector simulation.

The efficiency was measured from $W \rightarrow \mu\nu$ data to be $\epsilon_{z_{vertex}} = 0.949 \pm 0.023$ [54], which includes statistical (0.1%) and systematic uncertainties. The systematic uncertainties of $\pm 0.8\%$ and $\pm 2.3\%$ were assigned to the assumptions that the z_{vertex} efficiency does not depend on the total integrated luminosity and on the number of jets in the event, respectively.

4.2.2 Geometrical Acceptance

The geometrical acceptance for the b' signal is determined from the Monte Carlo samples described in Section 4.1, using a method similar to the one used in the CDF top dilepton analysis [56]. The method involves matching muon or electron objects that have been reconstructed by the detector simulation with the corresponding generator-level particle. The geometrical acceptance $\epsilon_{geom \cdot P_T}$ is defined as the fraction of the total events in the signal Monte Carlo simulation that pass the requirements below.
In the electron channel, each event must have:

- One reconstructed electron candidate with $E_T > 20$ GeV, in the central calorimeter and passing the fiducial criteria.
- A second electron-candidate object in the central or plug calorimeters with $E_T > 10$ GeV. No fiducial requirement is made on this second electron.
- The reconstructed track for both simulated electron objects above must lie within a cone of $\Delta R < 0.11$ around the momentum direction of a generator-level electron, where $\Delta R = \sqrt{\Delta\eta^2 + \Delta\phi^2}$.

In the muon channel, each event must have:

- One muon object candidate with $p_T > 20$ GeV/c detected by the CMU (with or without CMP confirmation) or the CMX muon chambers.
- A second muon candidate which can be a CMU, CMP, CMUP, CMX or CMIO with $p_T > 10$ GeV/c.

- The reconstructed track for both muon objects above must lie within a cone of $\Delta R <$ 0.11 about the momentum direction of a generator-level muon.

For this purpose, the minimum requirements to reconstruct an object as an electron candidate are a calorimeter cluster with $E_T > 5$ GeV and $E_{had}/E_{em} < 0.125$. Every stub in any of the muon chambers that is matched to a CTC track, and every track with $p_T > 10$ GeV/c that is not matched to a muon stub or calorimeter cluster (CMIO muons) is considered a muon candidate. So, $\epsilon_{geom \cdot P_T}$ is the acceptance before the lepton identification requirements of Section 3.2 have been imposed. This acceptance does not include the z_{vertex} efficiency which was obtained from data in Section 4.2.1.

The $\epsilon_{geom \cdot P_T}$ values are shown, as a function of the b' mass, in Figure 4.1 and Table 4.10 for electrons and Table 4.11 for muons. The geometrical acceptance for the first electron is slightly larger than the one for the first muon because the rapidity coverage of the central calorimeter ($|\eta| < 1.1$) is slightly larger than the central muon chambers ($|\eta| < 1.0$). However, the second electron can also be in the plug calorimeter which extends the rapidity coverage in the electron channel up to $|\eta| = 2.4$. So, the geometrical acceptance for a pair of electrons is significantly larger than for a pair of muons. Its ratio varies from 1.44 to 1.24 for b' masses of 100 GeV/c^2 to 210 GeV/c^2. $\epsilon_{geom \cdot P_T}$ increases with the b' mass because heavier b' pair production requires more violent collisions, which result in more central events. This also explains why the relative geometrical acceptances in the electron and muon channels is not constant as a function of the b' mass.

4.2.3 Z^0-mass Cut Efficiency

The Z^0-mass cut efficiency, ϵ_{Z-mass}, is defined as the fraction of Monte Carlo events passing the geometrical requirements above which have two leptons with an invariant mass in the Z^0 mass window 75 GeV/$c^2 \leq M_{l^+l^-} <$ 105 GeV/c^2. These two leptons are required to be matched with a generator level electron or muon. Table 4.10 and Table 4.11 show this efficiency as a function of the b' mass for electrons and muons, respectively.

We observe that the Z^0-mass cut efficiency decreases as a function of the b' mass.

This effect arises because the two leptons, which have passed the geometrical criteria above, were not required to originate from the Z^0 decay. Therefore, events in which one of the Z^0 leptons was lost due to a geometrical inefficiency can pass the geometrical requirements as long as other same-type lepton was observed. This third lepton can, for instance, originate from the weak decay of a b quark. The number of such leptons rises with the b' mass due to the increase of the event centrality. Therefore, the probability of having a second lepton that is not from the Z^0 decay passing the geometrical cuts also increases with the b' mass. It is interesting to notice that ϵ_{Z-mass} shows a trend opposite to $\epsilon_{geom \cdot p_T}$, as the above reasoning would suggest.

The Z^0 acceptance is calculated by multiplying the Z^0-mass cut efficiency, the geometrical acceptance and the z_{vertex} efficiency.

$$A_Z = \epsilon_{z_{vertex}} \cdot \epsilon_{geom \cdot p_T} \cdot \epsilon_{Z-mass} \tag{4.2}$$

The Z^0 acceptance is shown, as a function of the b' mass, for the electron channel in Figure 4.7 and Table 4.12, and for the muon channel in Figure 4.8 and Table 4.13. The Z^0 acceptance rises steadly with the b' mass due to the factors explained above.

Figure 4.2 shows the acceptance for the two detectors of the second leg electron relative to the total Z^0 acceptance, as a function of the b' mass. Events from more massive b' quarks have a larger percentage of electrons in the central calorimeter. This agrees with the statement of an increased event centrality for more massive b' quarks. In Figure 4.3, we show the same fractional acceptance but for each muon category. In this case, all the muon categories correspond to a central η region and therefore no significant trend is observed as a function of the b' mass. This information on the relative Z^0 acceptance will be crucial to calculate the Z^0 detection efficiency.

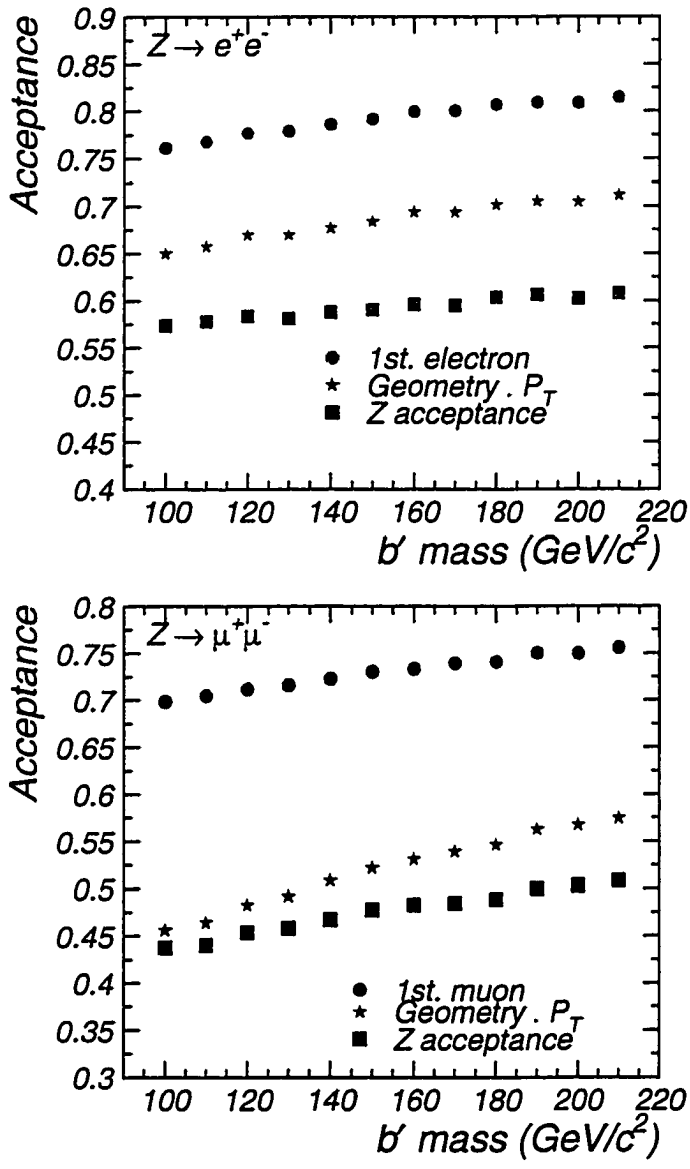

Figure 4.1: Geometrical acceptance calculated from the b' signal Monte Carlo. The points labeled "geometry·p_T " correspond to the geometrical acceptance for two electrons or muons as defined in 4.2.2. Top: Electron channel. Bottom: Muon channel.

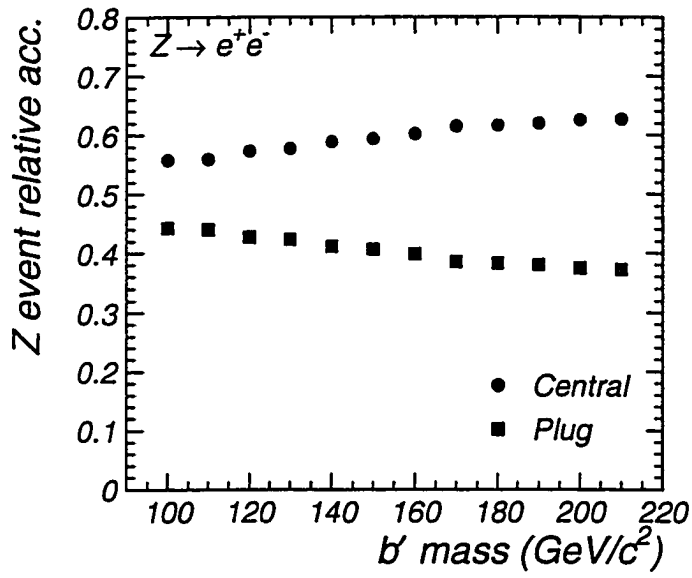

Figure 4.2: Acceptance for the two detectors of the second leg electron relative to the total $Z^0 \to e^+e^-$ acceptance, as a function of the b' mass.

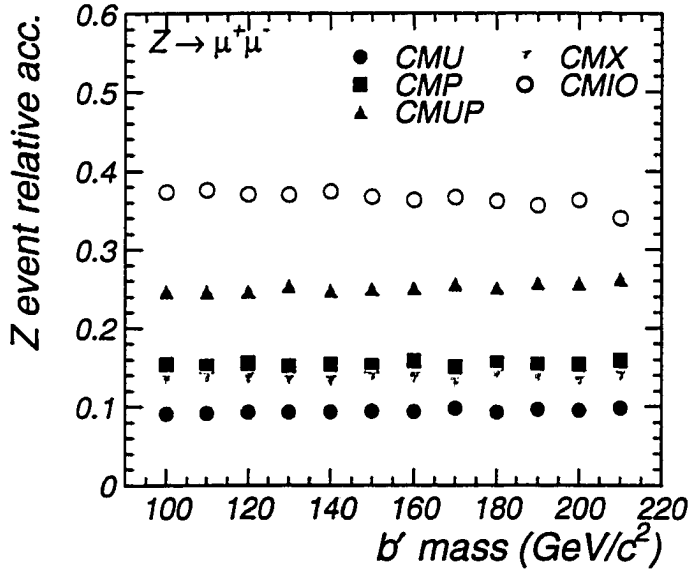

Figure 4.3: Acceptance for the several categories of the second leg muon relative to the total $Z^0 \to \mu^+\mu^-$ acceptance, as a function of the b' mass.

4.3 Z^0 Detection Efficiency

The Z^0 detection efficiency includes all the detector effects other than geometrical that reduce the acceptance for $Z^0 \to l^+l^-$ events from b' decays. These include the trigger efficiency, the lepton identification efficiencies and the lepton isolation efficiency.

4.3.1 Trigger Efficiency

In the electron channel, we use a trigger that requires a CTC track found by the Central Fast Tracker (CFT) [44]. The electron trigger efficiency is obtained solely from data. We use electron candidates that passed other triggers that do not require a CFT track and measure the probability that these electrons will pass the CFT trigger used in this analysis. We find that the central electron trigger efficiency is $\epsilon_{trigger} = (91.95 \pm 0.12)\%$ [57].

In the muon channel, we use triggers that require one jet in addition to the high-p_T muon. These triggers are very efficient for our signal because each event has at least three high-p_T jets. The overall trigger efficiency in the muon channel depends on the kinematics of the event because of these jet triggers and therefore it has to be obtained using a trigger simulation[2]. The trigger simulation takes into consideration the values for the muon trigger efficiencies measured from $Z^0 \to \mu^+\mu^-$ data, $\epsilon_{CMU/CMP} = 0.863^{+0.027}_{-0.031}$ and $\epsilon_{CMX} = 0.696^{+0.045}_{-0.049}$ [55], the jet trigger efficiency as a function of the jet E_T [60], and the trigger prescale values in Table 3.1. The efficiency is determined after all the jet selection criteria have been applied. The results, shown in Table 4.1, do not depend on the b' mass. The average trigger efficiency per event is 0.8140 ± 0.0013, where the uncertainty is statistical only.

4.3.2 Lepton Identification Efficiencies

The lepton identification efficiencies, $\epsilon_{lepton-id}$, were obtained from data [61] the $Z^0 \to e^+e^-$ and $Z^0 \to \mu^+\mu^-$ data samples. We start by looking for a lepton that passes

[2]The trigger simulation package used was SIM_MUTRIG [58]. This simulation is the same as the one used for the measurement of the top cross-section [59].

$m_{b'}$ [GeV/c^2]	$\epsilon_{trigger}$
100	0.814 ± 0.005
110	0.813 ± 0.005
120	0.815 ± 0.004
130	0.804 ± 0.004
140	0.814 ± 0.004
150	0.818 ± 0.004
160	0.812 ± 0.004
170	0.811 ± 0.004
180	0.818 ± 0.004
190	0.812 ± 0.004
200	0.815 ± 0.004
210	0.822 ± 0.005

Table 4.1: The muon trigger efficiency obtained from the trigger simulation as a function of the b' mass. The trigger efficiency calculation is done after the jet requirements.

the first leg selection requirements described in Section 3.2. Then, we look for a second same-type lepton candidate with $E_T > 20$ GeV that, together with the first lepton, makes an invariant mass close to the Z^0 mass, $75 < M_{l^+l^-} < 105$ GeV/c^2. The lepton identification efficiencies are given by the fraction of the second-leg lepton candidates that pass the loose and/or tight lepton identification requirements. The lepton isolation efficiency was calculated separately and is described in Section 4.3.3. The lepton identification efficiencies were obtained with the requirement that the E_T of the second leg electron is larger than 20 GeV. We have checked the lepton identification efficiencies with the $E_T > 10$ GeV requirement on the second leg and the results are consistent within the statistical error.

The efficiencies for the individual electron identification cuts are shown in Table 4.2. We emphasize that the requirements on the plug electron are very loose. Besides the 10 GeV E_T requirement, we only have the additional requirement that $E_{had}/E_{em} \leq 0.12$, which is very efficient. Thus, the electron identification efficiency for plug electrons is close to 100%. The total electron identification efficiency for the different types of electrons are shown in Table 4.3. These values do not include the conversion removal algorithm

overefficiency [47] which is included separately. The muon identification efficiencies for the different muon categories are shown in Table 4.4. These values are in good agreement with results from other studies [62, 63].

Efficiency	Central tight	Central loose	Plug
$E_{had}/E_{em} \leq 0.05$	0.944(3)		
$E_{had}/E_{em} \leq 0.12$		0.987(2)	0.995(1)
$E/P \leq 1.8$	0.895(5)		
$E/P \leq 2.0$		0.908(5)	
$\|\Delta x\| \leq 1.5$ cm	0.895(5)		
$\|\Delta z\| \leq 3.0$ cm			
$L_{shr} \leq 0.2$	0.972(2)		
$\chi^2_{strip} \leq 10.0$	0.945(4)		
$\|z_0 - z_v\| \leq 5.0$ cm	0.996(1)		

Table 4.2: Electron identification selection efficiencies for each individual cut.

Category	Central	Plug
Loose ϵ	0.901 $\pm$ 0.004	0.995 $\pm$ 0.001
Tight ϵ	0.804 $\pm$ 0.006	

Table 4.3: Electron identification efficiency for each electron category.

4.3.3 Isolation Efficiency

We require the second Z^0 lepton to pass the calorimeter isolation cut, $iso < 0.2$, described in Section 3.2. The isolation efficiency due to the jet activity in b'-signal events was calculated directly from the signal Monte Carlo simulation, for each type of electron and muon. The efficiency is measured using the Z^0 second lepton from events that passed the jet requirement, $\epsilon_{iso}^{b'MC} = \frac{N_{iso}}{N_{jet}}$. The electron isolation efficiency for each detector is shown in Table 4.5 as a function of the b' mass, and the average isolation efficiency for muons is

Category	Tight ϵ	Loose ϵ
CMU	0.869 ± 0.016	0.946 ± 0.012
CMP	0.876 ± 0.017	0.972 ± 0.008
CMUP	0.940 ± 0.006	0.982 ± 0.003
CMX	0.914 ± 0.008	0.950 ± 0.006
CMIO	N/A	0.911 ± 0.014

Table 4.4: Muon identification efficiencies for each muon category.

shown in Table 4.6. Heavier b' quarks will result in larger jet activity and centrality of the event, therefore the lepton isolation efficiency decreases with the increase of the b' mass.

$m_{b'}$ [GeV/c^2]	$\epsilon_{iso}^{b'MC}(central)$	$\epsilon_{iso}^{b'MC}(plug)$
100	0.953 ± 0.003	0.983 ± 0.002
110	0.939 ± 0.003	0.980 ± 0.002
120	0.919 ± 0.003	0.975 ± 0.002
130	0.920 ± 0.003	0.973 ± 0.002
140	0.918 ± 0.003	0.972 ± 0.002
150	0.915 ± 0.003	0.969 ± 0.002
160	0.918 ± 0.003	0.973 ± 0.002
170	0.911 ± 0.003	0.972 ± 0.002
180	0.913 ± 0.003	0.974 ± 0.002
190	0.913 ± 0.003	0.970 ± 0.003
200	0.916 ± 0.003	0.976 ± 0.002
210	0.914 ± 0.003	0.980 ± 0.002

Table 4.5: Isolation efficiency for an unbiased electron due to the jet activity in a b' signal event.

Multiple interactions, minimum bias events and underlying events add some level of isotropic energy in the calorimeters. To include this factor in our overall isolation efficiency we have computed a scaling factor between the isolation efficiency observed in the $Z^0 \rightarrow e^+e^-$ ($\mu^+\mu^-$) data and in a HERWIG $Z^0 \rightarrow e^+e^-$ ($\mu^+\mu^-$) Monte Carlo,

$$SF_{iso} = \frac{\epsilon_{iso}^{data}}{\epsilon_{iso}^{Z^0MC}}. \tag{4.3}$$

$m_{b'}$ [GeV/c^2]	$\epsilon_{iso}^{b' MC}$
100	0.927 ± 0.006
110	0.905 ± 0.006
120	0.888 ± 0.005
130	0.876 ± 0.006
140	0.876 ± 0.006
150	0.880 ± 0.006
160	0.883 ± 0.006
170	0.879 ± 0.006
180	0.876 ± 0.006
190	0.883 ± 0.006
200	0.873 ± 0.006
210	0.869 ± 0.006

Table 4.6: Isolation efficiency for an unbiased muon due to the jet activity in a b' signal event, averaged over all five muon categories and weighted by the numbers of events.

For this purpose, the isolation efficiency is computed with the events that pass the Z^0 selection criteria including lepton identification, but before any jet requirement. The results for central and plug electrons are shown in Table 4.7. The scale factor for each detector is different because of the different $|\eta|$ coverage. For central muons, the average isolation efficiency in the Z^0 Monte Carlo is 0.998 ± 0.001 while in the data we measure 0.985 ± 0.003. Thus, in the muon case, we take a scale factor $SF_{iso} = 0.987 \pm 0.003$, independent of the muon type.

$Z \rightarrow e^+e^-$	Central	Plug
Data	0.985 ± 0.002	0.951 ± 0.003
Monte-Carlo	0.998 ± 0.002	0.997 ± 0.002
SF_{iso}	0.987 ± 0.003	0.954 ± 0.004

Table 4.7: Isolation efficiency measured after the Z^0 selection in the data and in the $Z^0 \rightarrow e^+e^-$ Monte-Carlo. SF_{iso} is the ratio between both measurements.

The corrected isolation efficiency for a given lepton in detector x is obtained by

multiplying the efficiency from the b' Monte Carlo by the data scale factor.

$$\epsilon_{iso}^{x} = \epsilon_{iso}^{b'MC,x} \times SF_{iso}^{x} \tag{4.4}$$

The overall isolation efficiency for the b' events has to take into consideration the fact that there are two leptons in the event and each has a probability ϵ_{iso}^{x} of passing this cut. It is incorrect to consider that the event isolation efficiency is ϵ_{iso}^{x} because the isolation cut is done only on the second lepton. This approach would neglect the fact that when both leptons pass tight cuts, one passes isolation and the other fails isolation, the event always passes our cuts. The correct treatment of the event isolation efficiency needs to convolve the lepton identification, trigger and isolation efficiencies. This is explained in detail in Section 4.3.4.

4.3.4 Z^0 Efficiency Calculation

The Z^0 efficiency is composed of all the efficiencies mentioned in this section. Its calculation is rather complex because of the large number of different lepton categories and the existence of different levels of lepton identification cuts (tight and loose) for the first and second Z^0 leptons.

4.3.4.1 Electron Channel

The overall $Z^0 \rightarrow e^+e^-$ event detection efficiency can be separated in two terms.

$$\epsilon_Z = F_{cc} \cdot \epsilon_Z^{cc} + F_{cp} \cdot \epsilon_Z^{cp} \tag{4.5}$$

The first term accounts for events with both Z^0 electrons in the central calorimeter, while the second term accounts for events with one central and one plug electron. F_{cc} and F_{cp} are the fraction of Z^0 events in which the second leg falls into the central and plug calorimeter, respectively. These fractions were obtained from our studies of the geometrical acceptance, the results of which are shown in Figure 4.2.

In the case that the second electron is in the plug calorimeter the Z^0 efficiency, ϵ_Z^{cp}, is simply the product of all the detection efficiencies. These are the event trigger efficiency

ϵ_T, the central electron identification efficiency for first leg electrons c_1, the plug electron identification efficiency p, the correction factor for the overefficiency of the conversion removal algorithm $\epsilon_{conv} = 0.987 \pm 0.004$ [47] and the isolation efficiency for plug electrons ϵ^p_{iso}.

$$\epsilon^{cp}_Z = \epsilon_T \cdot c_1 \cdot \epsilon_{conv} \cdot p \cdot \epsilon^p_{iso} \tag{4.6}$$

In the case that both electrons are in the central calorimeter, either electron can be used for the Z^0 first leg. This factor makes the Z^0 efficiency for central-central events, ϵ^{cc}_Z, rather complicated,

$$\epsilon^{cc}_Z = \epsilon_T \cdot c_1 \cdot \epsilon_{conv} \cdot \epsilon_{iso} \left(2c_2 - \epsilon_T \cdot c_1 \cdot \epsilon_{conv} \cdot \epsilon_{iso}\right), \tag{4.7}$$

where we have introduced c_2, the central electron identification efficiency for second leg electrons and ϵ^c_{iso}, the isolation efficiency for central electrons. In this case, each central electron has 24 possible outcomes from which only the following nine are accepted:

1. $\epsilon_1 = \epsilon_T \cdot \epsilon_{conv} \cdot c_1 \cdot \epsilon_{iso}$
2. $\epsilon_2 = \epsilon_T \cdot \epsilon_{conv} \cdot c_1 \cdot (1 - \epsilon_{iso})$
3. $\epsilon_3 = \epsilon_T \cdot \epsilon_{conv} \cdot (c_2 - c_1) \cdot \epsilon_{iso}$
4. $\epsilon_4 = (1 - \epsilon_T) \cdot \epsilon_{conv} \cdot c_1 \cdot \epsilon_{iso}$
5. $\epsilon_5 = (1 - \epsilon_T) \cdot \epsilon_{conv} \cdot (c_2 - c_1) \cdot \epsilon_{iso}$
6. $\epsilon_6 = \epsilon_T \cdot (1 - \epsilon_{conv}) \cdot c_1 \cdot \epsilon_{iso}$
7. $\epsilon_7 = \epsilon_T \cdot (1 - \epsilon_{conv}) \cdot (c_2 - c_1) \cdot \epsilon_{iso}$
8. $\epsilon_8 = (1 - \epsilon_T) \cdot (1 - \epsilon_{conv}) \cdot c_1 \cdot \epsilon_{iso}$
9. $\epsilon_9 = (1 - \epsilon_T) \cdot (1 - \epsilon_{conv}) \cdot (c_2 - c_1) \cdot \epsilon_{iso}$

From the above, only electrons satisfying the conditions 1 and 2 can be used for the first Z^0 leg. Only electrons passing condition 1 can be used for both legs. Electrons that satisfy

any of the nine conditions can be used for the second leg of the Z^0 event. Therefore, the Z^0 efficiency for central-central electrons is given by,

$$\epsilon_Z^{cc} = \epsilon_1^2 + 2\epsilon_1(\epsilon_2 + \epsilon_3 + \epsilon_4 + \epsilon_5 + \epsilon_6 + \epsilon_7 + \epsilon_8 + \epsilon_9) \quad (4.8)$$

$$+2\epsilon_2(\epsilon_3 + \epsilon_4 + \epsilon_5 + \epsilon_6 + \epsilon_7 + \epsilon_8 + \epsilon_9) \quad (4.9)$$

$$= \epsilon_T \cdot c_1 \cdot \epsilon_{conv} \cdot \epsilon_{iso}(2c_2 - \epsilon_T \cdot c_1 \cdot \epsilon_{conv} \cdot \epsilon_{iso}) \quad (4.10)$$

The overall $Z^0 \to e^+e^-$ event detection efficiency obtained in this way is shown, as a function of the b' mass, in Table 4.8. Its average value is $\epsilon_Z = 0.734 \pm 0.002$, where the uncertainty is statistical only.

$m_{b'}$ [GeV/c^2]	ϵ_Z^{cc}	ϵ_Z^{cp}	ϵ_Z
100	0.767 ± 0.010	0.707 ± 0.006	0.741 ± 0.007
110	0.763 ± 0.010	0.705 ± 0.006	0.737 ± 0.007
120	0.756 ± 0.010	0.701 ± 0.006	0.732 ± 0.007
130	0.756 ± 0.010	0.700 ± 0.006	0.733 ± 0.007
140	0.756 ± 0.010	0.699 ± 0.006	0.732 ± 0.007
150	0.755 ± 0.010	0.697 ± 0.006	0.731 ± 0.007
160	0.755 ± 0.010	0.700 ± 0.006	0.733 ± 0.007
170	0.753 ± 0.010	0.700 ± 0.006	0.733 ± 0.007
180	0.754 ± 0.010	0.701 ± 0.006	0.733 ± 0.007
190	0.754 ± 0.010	0.698 ± 0.006	0.732 ± 0.007
200	0.755 ± 0.010	0.702 ± 0.006	0.735 ± 0.008
210	0.754 ± 0.010	0.705 ± 0.006	0.736 ± 0.008

Table 4.8: Z^0 efficiency in the electron channel. The first two columns give the efficiency for central-central and central-plug events. The last column is the averaged efficiency over both detectors.

4.3.4.2 Muon Channel

The overall event selection efficiency for a $Z^0 \to \mu^+\mu^-$ event is defined in a similar way as in the electron case,

$$\epsilon_Z = \epsilon_T \times (\epsilon_{lepton-id} \otimes \epsilon_{iso}) \quad (4.11)$$

where ϵ_T is the trigger efficiency per event, $\epsilon_{lepton-id}$ is the muon identification efficiency of Section 4.3.2, and ϵ_{iso} is the isolation efficiency of Section 4.3.3. The lepton identification efficiency and the isolation efficiency are convoluted because there are two muons per event and there are different levels of cuts (i.e. tight and loose) applied to each muon.

In order to calculate this quantity we divide the events into eleven different combinations depending on the muon types: CMU, CMP, CMUP, CMX and CMIO. The first Z^0 leg has to satisfy tight lepton identification cuts and no isolation cut while the second leg needs to pass loose lepton identification cuts and an isolation requirement. Furthermore, the Z^0 first leg cannot be a CMP or CMIO muon. Therefore, each combination of detectors falls into one of the following 3 categories:

CASE I) For CMU-CMU, CMUP-CMUP and CMX-CMX combinations, both muons can be used for the Z^0 first leg. Each muon has six possible outcomes from which only the following three are accepted:

1. It passes tight cuts and isolation, $\epsilon_1 = \epsilon_{tight} \cdot \epsilon_{iso}$
2. It passes tight cuts but fails isolation, $\epsilon_2 = \epsilon_{tight} \cdot (1 - \epsilon_{iso})$
3. It fails tight cuts but passes loose cuts and isolation, $\epsilon_3 = (\epsilon_{loose} - \epsilon_{tight}) \cdot \epsilon_{iso}$

In this case, the efficiency $(\epsilon_{lepton-id} \otimes \epsilon_{iso})$ is given by:

$$\epsilon_I^A = \epsilon_1^A \left(\epsilon_1^A + 2\epsilon_2^A + 2\epsilon_3^A\right) + 2\epsilon_2^A \cdot \epsilon_3^A \tag{4.12}$$

$$= \epsilon_{tight}^A \cdot \epsilon_{iso}^A \left(2\epsilon_{loose}^A - \epsilon_{tight}^A \cdot \epsilon_{iso}^A\right) \tag{4.13}$$

where A denotes the general detector common to both muons.

CASE II) For CMU-CMUP, CMU-CMX and CMUP-CMX combinations both muons can still be used for the first leg, however they are not indistinguishable as in CASE I because they are from different detectors. Each muon still has the same three possible outcomes that are accepted but it has to satisfy the cuts corresponding to its own detector.

In this case, if we denote each general detector by A and B, the efficiency $(\epsilon_{lepton-id} \otimes \epsilon_{iso})$ is given by:

$$\epsilon_{II}^{A-B} = 2\left(\epsilon_1^A\left(\epsilon_1^B+\epsilon_2^B+\epsilon_3^B\right)+\epsilon_2^A\left(\epsilon_1^B+\epsilon_3^B\right)+\epsilon_3^A\left(\epsilon_1^B+\epsilon_2^B\right)\right) \quad (4.14)$$

$$= 2\left(\epsilon_{tight}^A\cdot\epsilon_{loose}^B\cdot\epsilon_{iso}^B+\epsilon_{tight}^B\cdot\epsilon_{loose}^A\cdot\epsilon_{iso}^A-\epsilon_{tight}^A\cdot\epsilon_{tight}^B\cdot\epsilon_{iso}^A\cdot\epsilon_{iso}^B\right) \quad (4.15)$$

CASE III) If one muon is a CMP or a CMIO it cannot be used for the first leg and things are much simplified. The convolution of the lepton identification and isolation efficiencies is given by,

$$\epsilon_{III}^{A-B} = \epsilon_{tight}^A\cdot\epsilon_{loose}^B\cdot\epsilon_{iso}^B \quad (4.16)$$

where A denotes the detector of the first-leg muon.

The overall combined lepton identification and isolation efficiency for Z^0 events can be obtained by multiplying the efficiencies above by the corresponding event fractions F_A^B for detectors A and B,

$$\begin{aligned}(\epsilon_{lepton-id}\otimes\epsilon_{iso}) = {} & F_U^U\cdot\epsilon_I^U+F_X^X\cdot\epsilon_I^X+F_{UP}^{UP}\cdot\epsilon_I^{UP}+\\ & F_U^{UP}\cdot\epsilon_{II}^{U-UP}+F_U^X\cdot\epsilon_{II}^{U-X}+F_{UP}^X\cdot\epsilon_{II}^{UP-X}+\\ & F_U^P\cdot\epsilon_{III}^{U-P}+F_U^{IO}\cdot\epsilon_{III}^{U-IO}+F_{UP}^P\cdot\epsilon_{III}^{UP-P}+F_{UP}^{IO}\cdot\epsilon_{III}^{UP-IO}+\\ & F_X^P\cdot\epsilon_{III}^{X-P}+F_X^{IO}\cdot\epsilon_{III}^{X-IO}, \end{aligned} \quad (4.17)$$

where we made the abbreviations: CMU ≡ U, CMP ≡ P, CMUP ≡ UP, CMX ≡ X and CMIO ≡ I. The event fractions F_A^B where determined using the b' Monte Carlo described in Section 4.1 after the Z^0 mass cut has been applied. The differences between these fractions and the event fractions obtained after all cuts are within the statistical uncertainty.

4.4 Jet Selection Efficiencies

The jet selection efficiency is determined from the Monte Carlo samples described in Section 4.1. This efficiency is composed of two components, the 3-jet cut efficiency

$m_{b'}$ [GeV/c^2]	$\epsilon_{lepton-id} \otimes \epsilon_{iso}$	ϵ_{Z^0}
100	0.847 ± .007	0.690 ± 0.007
110	0.836 ± .008	0.679 ± 0.007
120	0.826 ± .008	0.673 ± 0.007
130	0.822 ± .008	0.661 ± 0.007
140	0.818 ± .007	0.666 ± 0.007
150	0.822 ± .008	0.673 ± 0.007
160	0.825 ± .008	0.670 ± 0.007
170	0.821 ± .008	0.666 ± 0.007
180	0.822 ± .008	0.672 ± 0.007
190	0.826 ± .008	0.671 ± 0.007
200	0.818 ± .008	0.667 ± 0.007
210	0.822 ± .009	0.675 ± 0.008

Table 4.9: The $\epsilon_{lepton-id} \otimes \epsilon_{iso}$ includes the lepton-id and isolation efficiencies. The Z^0 efficiency is obtained by multiplying the trigger efficiency by the first column.

and the $\sum E_T^{jets}$ cut efficiency: $\epsilon_{jet} = \epsilon_{3-jet} \cdot \epsilon_{\Sigma E_T}$. The 3-jet cut efficiency is defined by $\epsilon_{3-jet} = \frac{N_{3-jet}}{N_Z}$, where N_Z is the number of Monte Carlo events that pass the Z^0 selection and N_{3-jet} is the subset of such events that also pass the 3-jet requirement. The $\sum E_T^{jets}$ cut efficiency, $\epsilon_{\Sigma E_T} = \frac{N_{jet}}{N_{3-jet}}$, is calculated with the events that have passed the 3-jet criteria, where N_{jet} is the number of events that passed all the selection cuts but the b-tag requirement. The calculation of these efficiencies is done separately for b' events in the $Z^0 \to e^+e^-$ and $Z^0 \to \mu^+\mu^-$ channels. The results are presented in Table 4.10 and Figure 4.4 for electrons, and in Table 4.11 and Figure 4.5 for muons. The step observed in the efficiency for b' masses between 120 GeV/c^2 and 130 GeV/c^2 is due to the different requirement on the energy of the third jet for $m_{b'} \leq 120$ GeV/c^2 and more massive b' quarks.

The overall jet efficiency is higher in the muon channel than in the electron due to several factors. First, the muon sample is composed of events that are more central than the electron ones because the muon selection requires muons to be within $|\eta| < 1.1$, while electrons can have $|\eta|$ up to 2.4. More central events result from more violent collisions, and therefore the jet energy present in the event is higher. Furthermore, the centrality

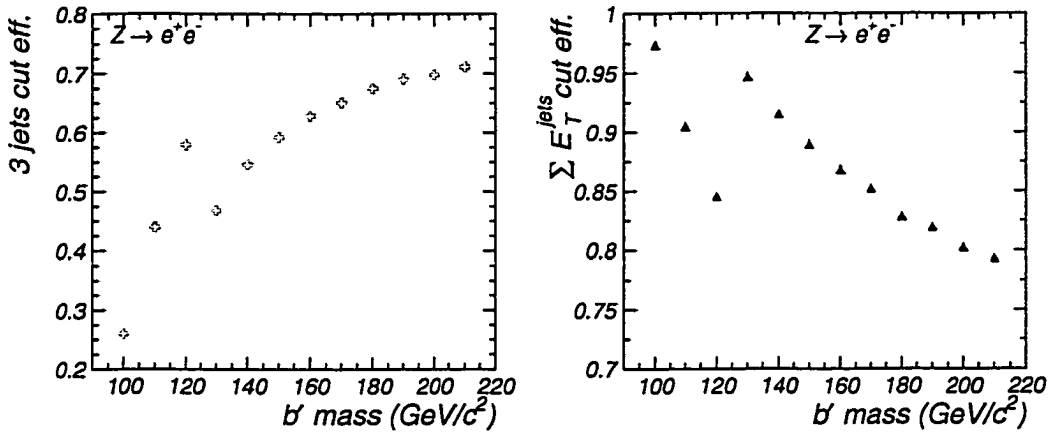

Figure 4.4: Jet selection efficiencies, as a function of the b' mass, for events in the electron channel. Left: 3-jet efficiency; Right: $\sum E_T^{jets}$ efficiency.

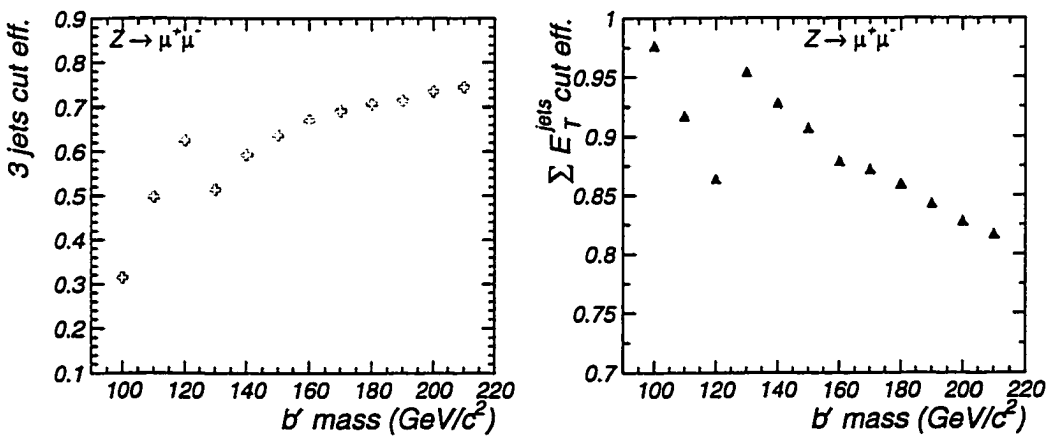

Figure 4.5: Jet selection efficiencies, as a function of the b' mass, for events in the muon channel. Left: 3-jet efficiency; Right: $\sum E_T^{jets}$ efficiency.

of the event will result in a better acceptance for the jets, which will be less likely to fail the $|\eta| < 2$ cut. Besides that, jets and electrons look very similar in our detector. They are distinguished by the relative energy deposited in the hadronic and electromagnetic calorimeters. It is possible that, if one electron is lost, a jet will fake an electron which will pass our Z^0 selection. In this case, the event will lack one jet and therefore it will be less likely to pass the 3-jet requirement. Another possibility is that a jet and an electron overlap in the calorimeters in such a way that they are indistinguishable. In this case, the jet could be incorporated in the electron and thus be removed from our jet counting.

$m_{b'}$	signal acceptance/efficiencies [%]				
[GeV/c^2]	geometry·P_T	Z-mass cut	3-jet cut	$\sum E_T^{jets}$ cut	b–tag
100	65.0 ± 0.2	88.3 ± 0.2	25.9 ± 0.5	97.4 ± 0.2	15.3 ± 0.4
110	65.7 ± 0.2	87.9 ± 0.2	43.9 ± 0.5	90.5 ± 0.3	27.1 ± 0.5
120	67.0 ± 0.2	87.2 ± 0.2	57.9 ± 0.5	84.6 ± 0.3	36.2 ± 0.5
130	67.0 ± 0.2	86.8 ± 0.2	46.8 ± 0.5	94.7 ± 0.3	43.3 ± 0.5
140	67.7 ± 0.2	86.8 ± 0.2	54.6 ± 0.5	91.5 ± 0.3	45.8 ± 0.5
150	68.4 ± 0.2	86.3 ± 0.2	59.2 ± 0.5	89.0 ± 0.3	47.9 ± 0.5
160	69.4 ± 0.3	85.9 ± 0.2	62.8 ± 0.5	86.9 ± 0.3	48.7 ± 0.5
170	69.4 ± 0.3	85.7 ± 0.2	65.1 ± 0.5	85.3 ± 0.3	50.2 ± 0.5
180	70.2 ± 0.3	86.1 ± 0.2	67.5 ± 0.5	82.9 ± 0.3	52.1 ± 0.5
190	70.5 ± 0.3	86.0 ± 0.2	69.0 ± 0.5	82.0 ± 0.3	51.5 ± 0.5
200	70.5 ± 0.3	85.4 ± 0.2	69.7 ± 0.5	80.3 ± 0.3	52.2 ± 0.5
210	71.2 ± 0.3	85.4 ± 0.2	71.1 ± 0.5	79.3 ± 0.3	53.1 ± 0.5

Table 4.10: Acceptance calculated directly from the signal b' Monte Carlo for events in the electron channel. Note that the geometry·p_T does not include the z_{vertex} efficiency and the b-tag does not include the b-tag scale factor.

4.5 b-tag Efficiency

The b-tag efficiency was calculated from the b' signal Monte Carlo and adjusted by a scale factor obtained from data, $\epsilon_{b-tag} = \epsilon_{b-tag}^{b'MC} \times SF_{b-tag}^{event}$. We define the event b-tag efficiency obtained from the Monte Carlo as $\epsilon_{b-tag}^{b'MC} = \frac{N_{b-tag}}{N_{jet}}$, where N_{jet} is the number of

$m_{b'}$	signal acceptance/efficiencies [%]				
[GeV/c^2]	geometry·p_T	Z-mass cut	3-jet cut	$\sum E_T^{jets}$ cut	b–tag
100	45.6 ± 0.2	96.0 ± 0.1	31.5 ± 0.5	97.7 ± 0.3	17.0 ± 0.4
110	46.4 ± 0.3	94.8 ± 0.2	49.7 ± 0.6	91.8 ± 0.4	30.7 ± 0.5
120	48.3 ± 0.3	93.9 ± 0.2	62.6 ± 0.6	86.4 ± 0.4	38.4 ± 0.5
130	49.2 ± 0.3	93.1 ± 0.2	51.4 ± 0.6	95.5 ± 0.4	45.2 ± 0.6
140	50.8 ± 0.3	92.0 ± 0.2	59.3 ± 0.6	92.8 ± 0.4	48.0 ± 0.5
150	52.2 ± 0.3	91.6 ± 0.2	63.7 ± 0.5	90.7 ± 0.4	49.2 ± 0.5
160	53.1 ± 0.3	90.9 ± 0.2	67.0 ± 0.5	87.9 ± 0.4	50.9 ± 0.5
170	53.9 ± 0.3	89.9 ± 0.2	69.2 ± 0.5	87.3 ± 0.4	52.5 ± 0.5
180	54.6 ± 0.3	89.4 ± 0.2	70.7 ± 0.5	86.0 ± 0.4	51.8 ± 0.6
190	56.3 ± 0.3	88.8 ± 0.2	71.4 ± 0.5	84.3 ± 0.4	52.9 ± 0.6
200	56.7 ± 0.3	88.7 ± 0.2	73.5 ± 0.5	82.8 ± 0.4	53.6 ± 0.6
210	57.5 ± 0.3	88.5 ± 0.3	74.4 ± 0.5	81.7 ± 0.4	54.4 ± 0.6

Table 4.11: Acceptance calculated from the signal b' Monte Carlo for events in the muon channel. Note that the geometry·p_T does not include the z_{vertex} efficiency and the b-tag does not include the b-tag scale factor.

events that passed all the selection criteria besides the b-tag requirement and N_{b-tag} is the subset of N_{jet} that in addition passed the b-tag cut. We observe that as expected, the b-tag efficiency is strongly dependent on the b' mass because for small b' mass the E_T of the b jets is considerably lower. Table 4.10 and Table 4.11 show the b-tag efficiencies obtained directly from the signal Monte Carlo as a function of the b' mass.

The detector simulation produces a better tracking efficiency than the one for data. To account for this we include a track degradation scale factor [64] calculated using data,

$$SF_{b-tag}^{deg} = \frac{\epsilon_{b-tag}^{data}}{\epsilon_{b-tag}^{b'MC}} = 0.87 \pm 0.07 \tag{4.18}$$

On the other hand, it has been found that the b-tagging efficiency in Monte Carlo events is actually smaller than for real data. This is due to several other factors in the detector simulation which we correct for by introducing another scale factor [65, 66]. In our analysis, we used the SECVTX scale factor determined for the W + 3 jets top events, $SF_{b-tag}^{W} = 1.22 \pm 0.12$. The heavy flavor content in $t\bar{t} \rightarrow bW\bar{b}W$, is smaller than in $b'\overline{b'}$ events because in the latter about 15% of the events have four b-jets, where the extra two jets come from

a Z^0 decay. This effect should be very small (less than 2%) but difficult to determine and therefore we have neglected it. The overall b-tag scale factor per event is given by,

$$SF^{event}_{b-tag} = SF^{deg}_{b-tag} \times SF^{W}_{b-tag} = 1.06 \pm 0.10 \tag{4.19}$$

The final event b-tag efficiency is given by $\epsilon_{b-tag} = \epsilon^{b'MC}_{b-tag} \times SF^{event}_{b-tag}$. The numbers obtained are consistent with the expectations. For large b' masses, we expected a b-tag efficiency slightly larger than the one for $t\bar{t}$ ($\epsilon_{svx} = 0.505 \pm 0.051$ [67]) because each b' event has at least two high-p_T b quarks just like a top event but, in addition 15% of the b' events have a Z^0 which decays into $b\bar{b}$. In these events there are four high-p_T b quarks.

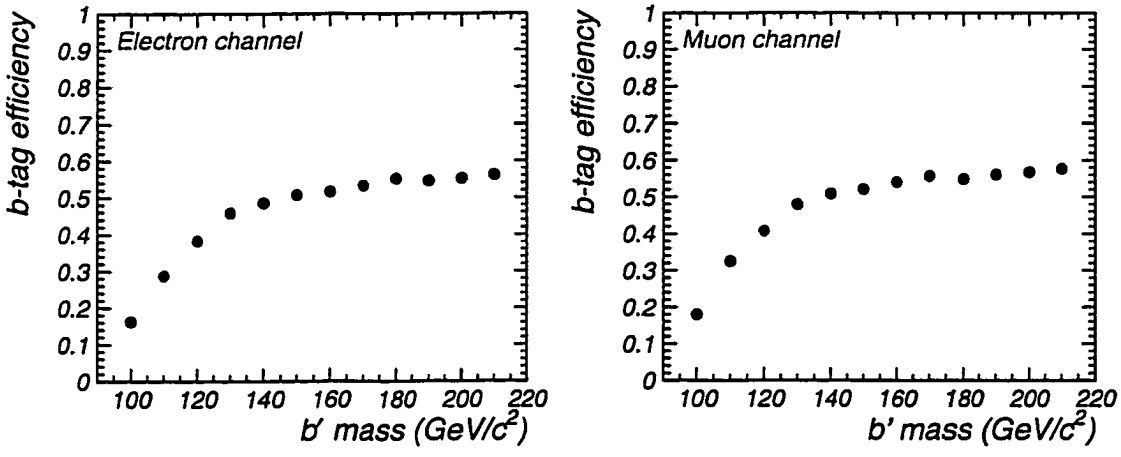

Figure 4.6: b-tag efficiency as a function of the b' mass including the b-tag scale factor. Left: Electron channel. Right. Muon channel.

4.6 Total Acceptance × Efficiency ($A \cdot \epsilon$)

The total acceptance × efficiency is the product of all independent acceptances and efficiencies calculated in this Chapter,

$$A \cdot \epsilon = \underbrace{\epsilon_{z_{vertex}} \cdot \epsilon_{geom\text{-}P_T} \cdot \epsilon_{Z-mass}}_{A_Z} \cdot \epsilon_Z \cdot \underbrace{\epsilon_{3-jet} \cdot \epsilon_{\Sigma E_T}}_{\epsilon_{jet}} \cdot \epsilon_{b-tag}. \tag{4.20}$$

The total acceptance × efficiency is given in Table 4.12 and Figure 4.7 for electrons, and in Table 4.13 and Figure 4.8 for muons.

$m_{b'}$	$(A \cdot \epsilon)$ [%]				
[GeV/c^2]	$\epsilon_{z_{vertex}} \cdot \epsilon_{geo \cdot p_T}$	A_Z	$A_Z \cdot \epsilon_Z$	$A_Z \cdot \epsilon_Z \cdot \epsilon_{jet}$	$A_Z \cdot \epsilon_Z \cdot \epsilon_{jet} \cdot \epsilon_{b-tag}$
100	61.7 ± 0.2	54.5 ± 0.2	40.3 ± 0.1	10.2 ± 0.1	1.65 ± 0.05
110	62.4 ± 0.2	54.9 ± 0.2	40.4 ± 0.2	16.1 ± 0.1	4.62 ± 0.09
120	63.6 ± 0.2	55.4 ± 0.2	40.6 ± 0.2	19.9 ± 0.2	7.62 ± 0.11
130	63.6 ± 0.2	55.2 ± 0.2	40.4 ± 0.2	17.9 ± 0.2	8.22 ± 0.12
140	64.3 ± 0.2	55.8 ± 0.2	40.9 ± 0.2	20.4 ± 0.2	9.91 ± 0.13
150	64.9 ± 0.2	56.0 ± 0.2	41.0 ± 0.2	21.6 ± 0.2	10.9 ± 0.14
160	65.9 ± 0.2	56.6 ± 0.3	41.5 ± 0.2	22.6 ± 0.2	11.6 ± 0.15
170	65.9 ± 0.2	56.5 ± 0.3	41.4 ± 0.2	23.0 ± 0.2	12.2 ± 0.15
180	66.6 ± 0.2	57.3 ± 0.3	42.0 ± 0.2	23.5 ± 0.2	12.9 ± 0.16
190	66.9 ± 0.2	57.5 ± 0.3	42.1 ± 0.2	23.8 ± 0.2	13.0 ± 0.16
200	66.9 ± 0.3	57.2 ± 0.3	42.0 ± 0.2	23.5 ± 0.2	13.0 ± 0.17
210	67.6 ± 0.3	57.7 ± 0.3	42.5 ± 0.2	24.0 ± 0.2	13.4 ± 0.17

Table 4.12: Acceptance × efficiency for the b' signal in the electron channel. The two last columns show the final $(A \cdot \epsilon)$ before and after b-tag.

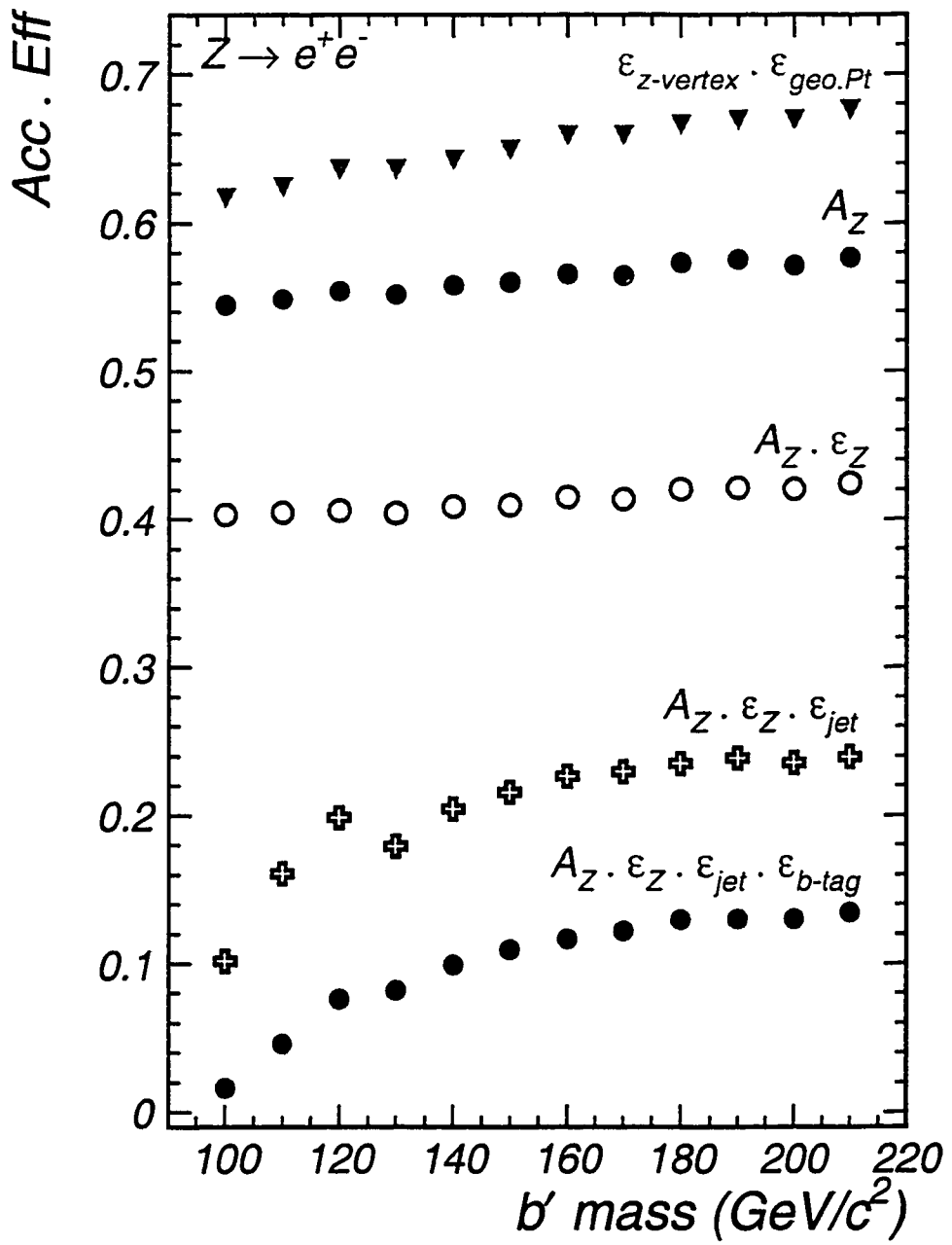

Figure 4.7: Acceptance × efficiency ($A \cdot \epsilon$), in the electron channel, as a function of the b' mass after the successive selection criteria.

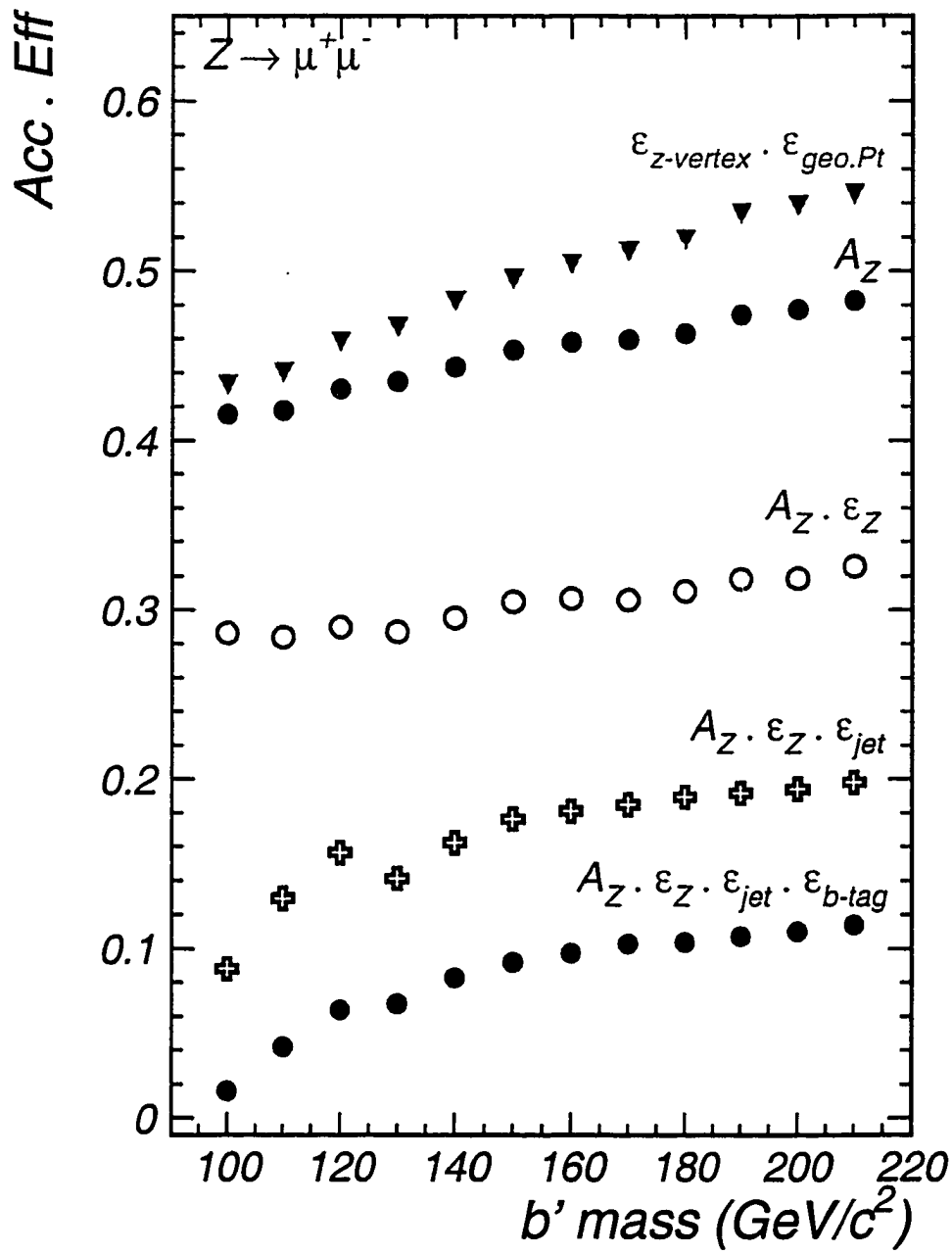

Figure 4.8: Acceptance × efficiency ($A \cdot \epsilon$) in the muon channel, as function of b' mass after the successive selection criteria.

$m_{b'}$ [GeV/c^2]	$(A \cdot \epsilon)$ [%]				
	$\epsilon_{z_{vertex}} \cdot \epsilon_{geo \cdot p_T}$	A_Z	$A_Z \cdot \epsilon_Z$	$A_Z \cdot \epsilon_Z \cdot \epsilon_{kin}$	$A_Z \cdot \epsilon_Z \cdot \epsilon_{kin} \cdot \epsilon_{b-tag}$
100	43.3 ± 0.2	41.5 ± 0.2	28.7 ± 0.1	8.8 ± 0.1	1.59 ± 0.04
110	44.0 ± 0.2	41.8 ± 0.2	28.4 ± 0.2	12.9 ± 0.1	4.21 ± 0.09
120	45.8 ± 0.2	43.0 ± 0.2	29.0 ± 0.2	15.7 ± 0.1	6.37 ± 0.10
130	46.7 ± 0.2	43.5 ± 0.2	28.7 ± 0.2	14.1 ± 0.1	6.76 ± 0.10
140	48.2 ± 0.2	44.4 ± 0.2	29.5 ± 0.2	16.3 ± 0.1	8.27 ± 0.11
150	49.5 ± 0.2	45.3 ± 0.2	30.5 ± 0.2	17.6 ± 0.1	9.20 ± 0.12
160	50.4 ± 0.3	45.8 ± 0.3	30.7 ± 0.2	18.1 ± 0.2	9.77 ± 0.13
170	51.2 ± 0.3	46.0 ± 0.3	30.6 ± 0.2	18.5 ± 0.2	10.30 ± 0.14
180	51.9 ± 0.3	46.3 ± 0.3	31.1 ± 0.2	18.9 ± 0.2	10.39 ± 0.14
190	53.4 ± 0.3	47.4 ± 0.3	31.8 ± 0.2	19.2 ± 0.2	10.76 ± 0.15
200	53.8 ± 0.3	47.8 ± 0.3	31.9 ± 0.2	19.4 ± 0.2	11.01 ± 0.15
210	54.5 ± 0.3	48.3 ± 0.3	32.6 ± 0.2	19.8 ± 0.2	11.43 ± 0.17

Table 4.13: Acceptance × efficiency for the b' signal in the muon channel. The two last columns show the final $(A \cdot \epsilon)$ before and after b-tag.

Chapter 5

Systematic Uncertainties

The efficiency and acceptance calculations described in the previous chapter depend on many particulars that can introduce a bias into the final result. Uncertainties in the detector response and Monte Carlo description of nature are among the most important ones. While we try to correct for most of these factors, some remain without being fully understood and therefore they can be seen as irreducible. In this chapter, we account for all the systematic uncertainties that we know affect the final results in our acceptance calculation. We describe in some detail the estimation of the systematic uncertainty due to the jet energy scale, gluon radiation and the parton distribution function. We finish with a summary of all the systematic uncertainties considered in the determination of the b' acceptance.

5.1 Jet-Energy Scale

The calorimeter jet-energy measurement has a large relative uncertainty due to the detector calibration and stability, fragmentation effects and the underlying event. The b' kinematic efficiency is strongly dependent on the jet-energy scale because of the requirement at low b' mass of a jet with $E_T > 7$ GeV, which is near the detector threshold, and the $\sum E_T^{jets}$ cut. To estimate the systematic uncertainty introduced by the jet-energy scale, we vary the energy of the jets in the Monte Carlo simulation by a factor of $\pm 10\%$. The

effects of the variation of the jet E_T on the kinematic distributions are shown in Figures 5.1 and 5.2. Figure 5.1 shows the jet-E_T and multiplicity distributions for events from 100 GeV b'-quarks. With the decrease in jet-E_T, the jets that were produced near the threshold of the jet-E_T cut are lost. Since a large percentage of events for low b' masses only have three jets, this results in a considerable loss of events. Figure 5.2 shows the $\sum E_T^{jets}$ and multiplicity distributions for 150 GeV b'-quark events. For heavier b' quarks, most events have at least four jets and most jets have large E_T relative to the cut threshold. In this case, the jet-energy scale has the largest impact on the $\sum E_T^{jets}$ distribution, resulting in a significant variation in the number of events that pass the kinematic cuts.

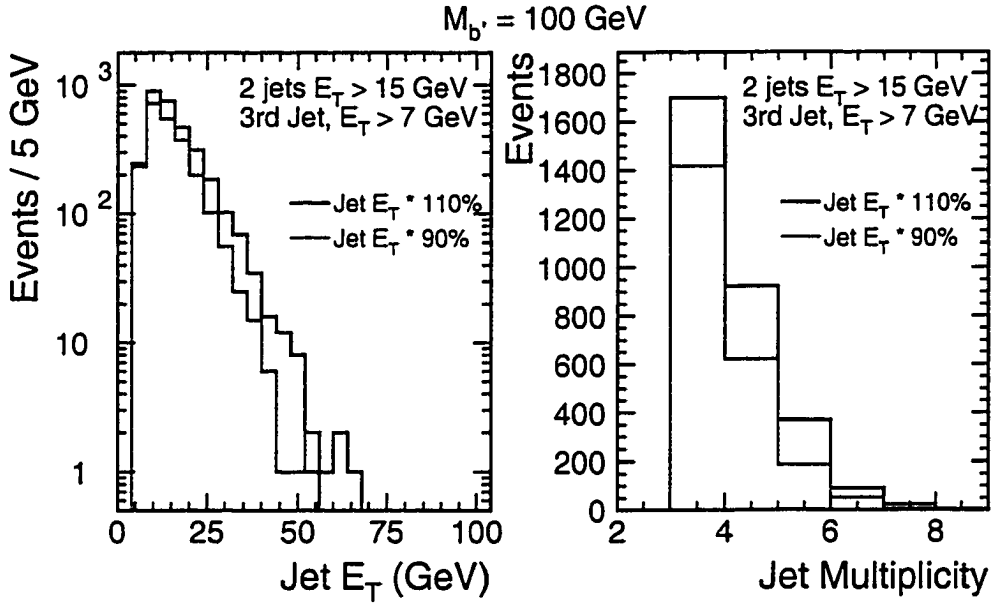

Figure 5.1: Jet-E_T scale impact on kinematic distribution for $m_{b'} = 100$ GeV in the muon channel. Left: third-jet E_T distribution; Right: jet multiplicity distribution. The plots were made after the 3-jet requirement but before the $\sum E_T^{jets}$ cut.

We recalculate the efficiencies, for the twelve b' masses from 100 to 210 GeV/c^2, using the Monte Carlo samples with the ±10% variations of jet E_T. From these, the jet-energy scale systematic uncertainty, $\Delta_{1/2}^{js}$, is defined by the following equation,

$$\Delta_{1/2}^{js} = \frac{1}{2} \times \frac{\epsilon_{110\%} - \epsilon_{90\%}}{\epsilon_{default}} \tag{5.1}$$

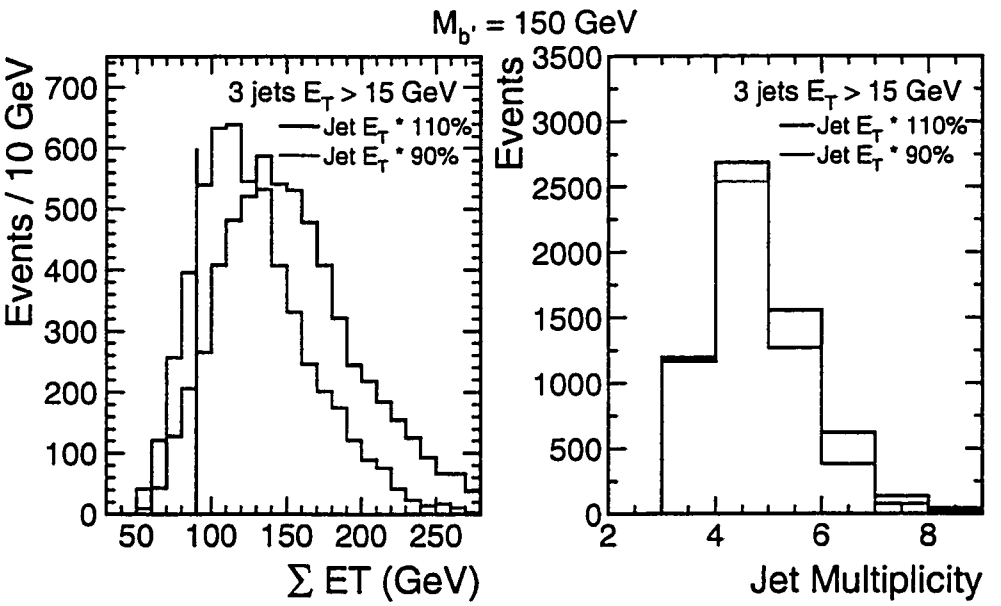

Figure 5.2: Jet-E_T scale impact on kinematic distribution for $m_{b'} = 150$ GeV in the muon channel. Left: $\sum E_T^{jets}$ distribution. The vertical line shows the place of the cut; Right: jet multiplicity distribution. The plots were made after the 3-jet requirement but before the $\sum E_T^{jets}$ cut.

where $\epsilon_{default}, \epsilon_{110\%}, \epsilon_{90\%}$ are the overall b' acceptance times efficiency calculated with the default jet-energy scale, and the jet-energy scale varied by +10% and -10%, respectively.

Several efficiencies for these variations of jet-E_T are shown in Figure 5.3 and 5.4, for the electron and muon channels respectively. In these plots, the top graphs show the value of the efficiencies for the three cases of jet-E_T and the bottom graphs show the systematic uncertainty on the corresponding efficiency. The systematic uncertainties due to the jet-energy scale, on the 3-jet cut and the $\sum E_T^{jets}$ cut efficiencies change as a function of the b' mass in opposite directions, mainly because of the scaling of the $\sum E_T^{jets}$ cut. Consequently, the variation in the combined jet-selection efficiency is fairly flat with the b' mass. The muon trigger and isolation efficiency do not show any appreciable dependence on the jet-energy scale.

The effect on the b-tag efficiency is anti-correlated with the effect on the jet-selection efficiencies. This can be understood in the following way. If the jet-energy scale is lowered, fewer events will pass the jet selection. However, the ones that pass have jets with larger E_T which are more likely to be tagged by the SVX b-tagging algorithm. So, the jet-selection efficiency decrease is partially compensated by an increase in the b-tag efficiency.

We use the total efficiency to make our best estimation of the jet-energy scale systematic uncertainty. The use of the total efficiency accounts for all the correlations mentioned above. We estimate that in the electron channel the this systematic uncertainty is 16% for b' masses of 100 GeV, 13% for $m_{b'}$= 110 GeV and 12% for higher b' masses. In the muon channel, the systematic uncertainty is 13%, 12% and 11% for the same b' masses.

5.2 Gluon Radiation

The Monte Carlo generator includes the modeling of gluon radiation from initial-state (ISR) and final-state (FSR) partons. The emission of these gluons increases the jet multiplicity and therefore it affects the overall efficiency determination for signal events. An example of b' production with an additional gluon from ISR is shown in Figure 5.5.

Traditionally at CDF, the PYTHIA Monte Carlo program [72] has been used to

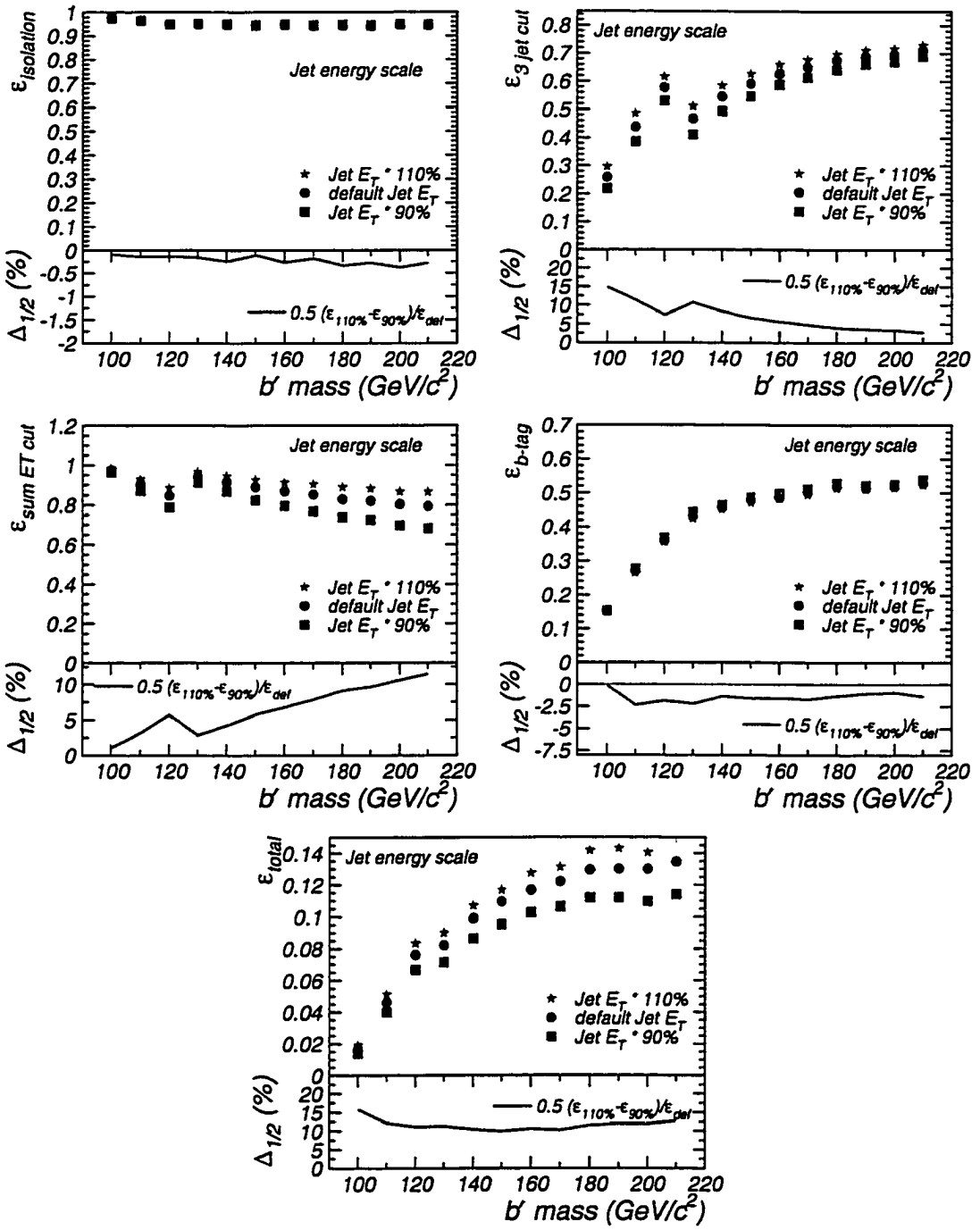

Figure 5.3: Jet-energy scale effect on several efficiencies in the electron channel. Each efficiency is plotted for three variations of jet-E_T scale. The line graph shows the half of the percent difference between the 90% and the 110% cases. The bottom-right plot shows the collective effect on the total efficiency.

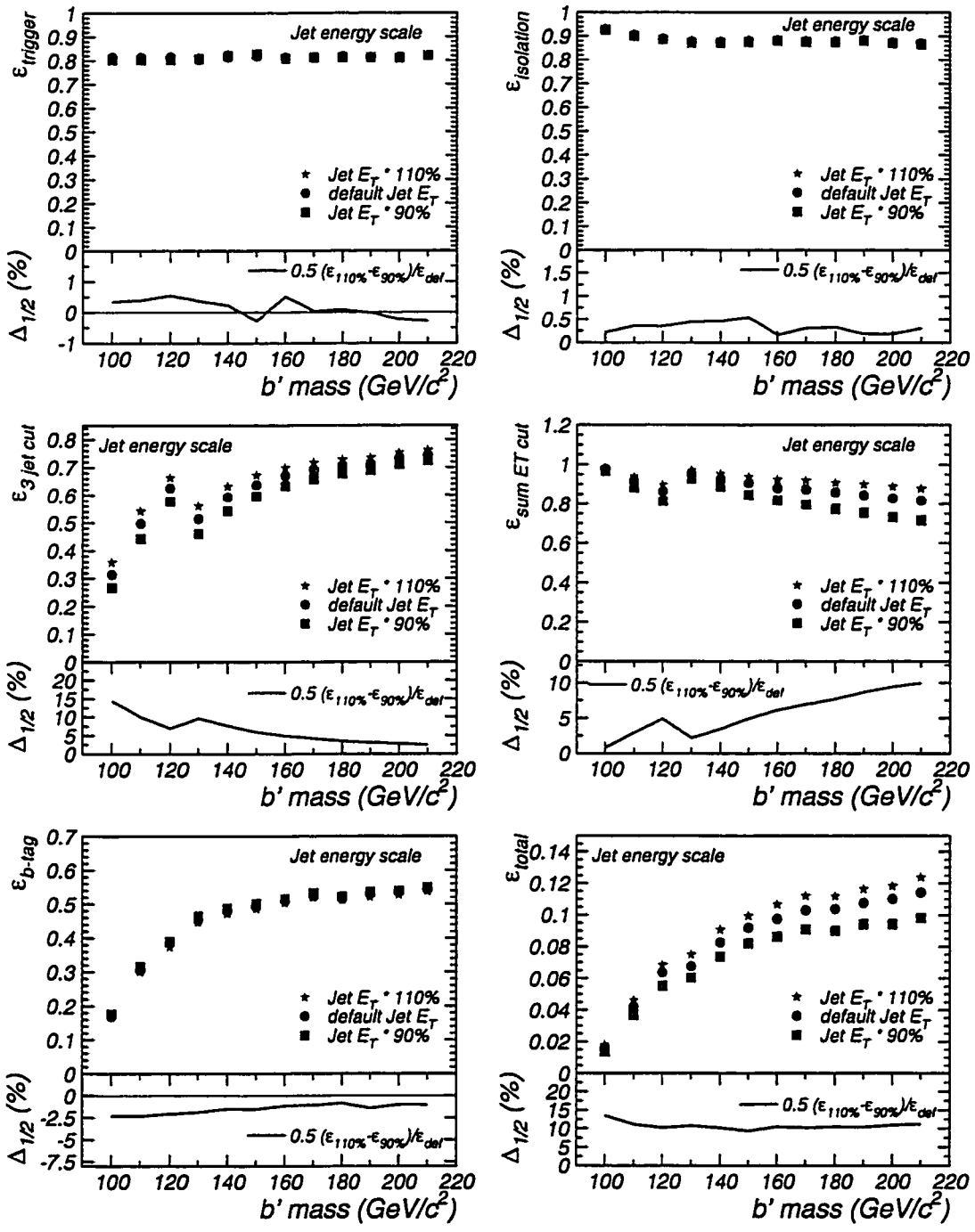

Figure 5.4: Jet-energy scale effect on several efficiencies in the muon channel. Each efficiency is plotted for three variations of jet-E_T scale. The line graph shows the half of the percent difference between the 90% and the 110% cases. The bottom-right plot shows the collective effect on the total efficiency.

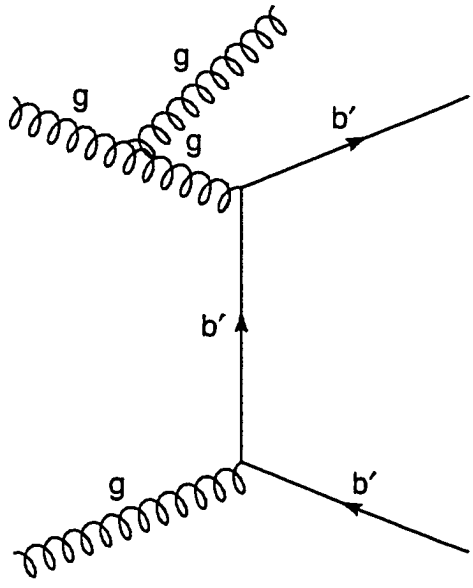

Figure 5.5: Sample Feynman diagram of $b'\bar{b}'$ production with associated initial state gluon radiation.

estimate the effects of the amount of gluon radiation in the Monte Carlo model, even when the signal acceptances are calculated with HERWIG. This happens because it is possible to turn off initial and final state radiation in PYTHIA while it is not possible in HERWIG. However, since the Monte Carlo programs are different, it is not clear that the results obtained with PYTHIA apply to the gluon radiation model in HERWIG.

In our analysis, we used the HERWIG generator, the same program used to calculate the acceptances, to estimate the gluon radiation systematic uncertainty. We devised a method that effectively works the same way as the "switch" in PYTHIA to turn initial and final state radiation on and off. In the Monte Carlo simulation, we used the particle generation codes to identify the partons originating from the initial/final state of the hard collision that produces the b' quarks. We then selected the events whose ISR/FSR partons had all $p_T < 7$ GeV. This way, we obtained a sample virtually free of ISR/FSR because the low-p_T partons are not seen in the detector. Using this ISR/FSR "free" sample, we

calculated the total efficiency and compared it with the previously calculated values for the samples with standard gluon radiation. We then define the systematic uncertainty due to ISR or FSR, $\Delta_{1/2}^{ISR/FSR}$, to be

$$\Delta_{1/2}^{ISR/FSR} = \frac{1}{2} \times \frac{\epsilon_{on} - \epsilon_{off}}{\epsilon_{on}} \tag{5.2}$$

The method was applied separately for the initial and final-state gluon radiation.

The presence of gluon radiation increases the jet multiplicity and therefore increases the efficiency of the three-jet requirement. This effect is more pronounced at low b' mass because the b quarks from low-mass b' decay are produced near threshold and therefore are detected with low efficiency. The jets resulting from gluon radiation have a very small content of heavy flavor. Therefore, the b-tagging efficiency on events which third-jet comes from gluon radiation is very small. So, the effect of gluon radiation on the b-tagging efficiency for a low mass b' is anti-correlated with the effect on the jet-selection efficiencies. The plots in Figures 5.6 and 5.7 show the effect of ISR on several efficiencies, in the electron and muon channels. In general, the gluon radiation adds some amount of jet-energy to the event. This results in a small increase of the $\sum E_T^{jets}$ efficiency. On the other hand, the presence of extra jets decreases the lepton isolation efficiency because the probability of an overlap between a jet and a lepton is larger. We take the collective effect on the total efficiency as our best estimation of the ISR systematic uncertainty. In the electron channel, we estimate a systematic uncertainty varying from 19% for $m_{b'} = 100$ GeV, to 6% for $m_{b'} \geq 130$ GeV. In the muon channel, the uncertainty varies from 18% for $m_{b'} = 100$ GeV, to 6% for $m_{b'} \geq 120$ GeV.

The final-state gluon radiation systematic uncertainty is calculated in the a similar way to the initial-state radiation systematic. The initial-state radiation has a much stronger effect on our acceptance calculations than the final-state radiation. The FSR gluons originate from a more massive object and therefore they carry less momemtum than the ISR gluons. Table 5.1 shows the percentage of the b' Monte Carlo events that have ISR/FSR energetic enough to be seen in the detector. This number is fairly constant for all b' masses. The bottom right plots in Figure 5.8 and Figure 5.9 show the overall effect of the FSR on

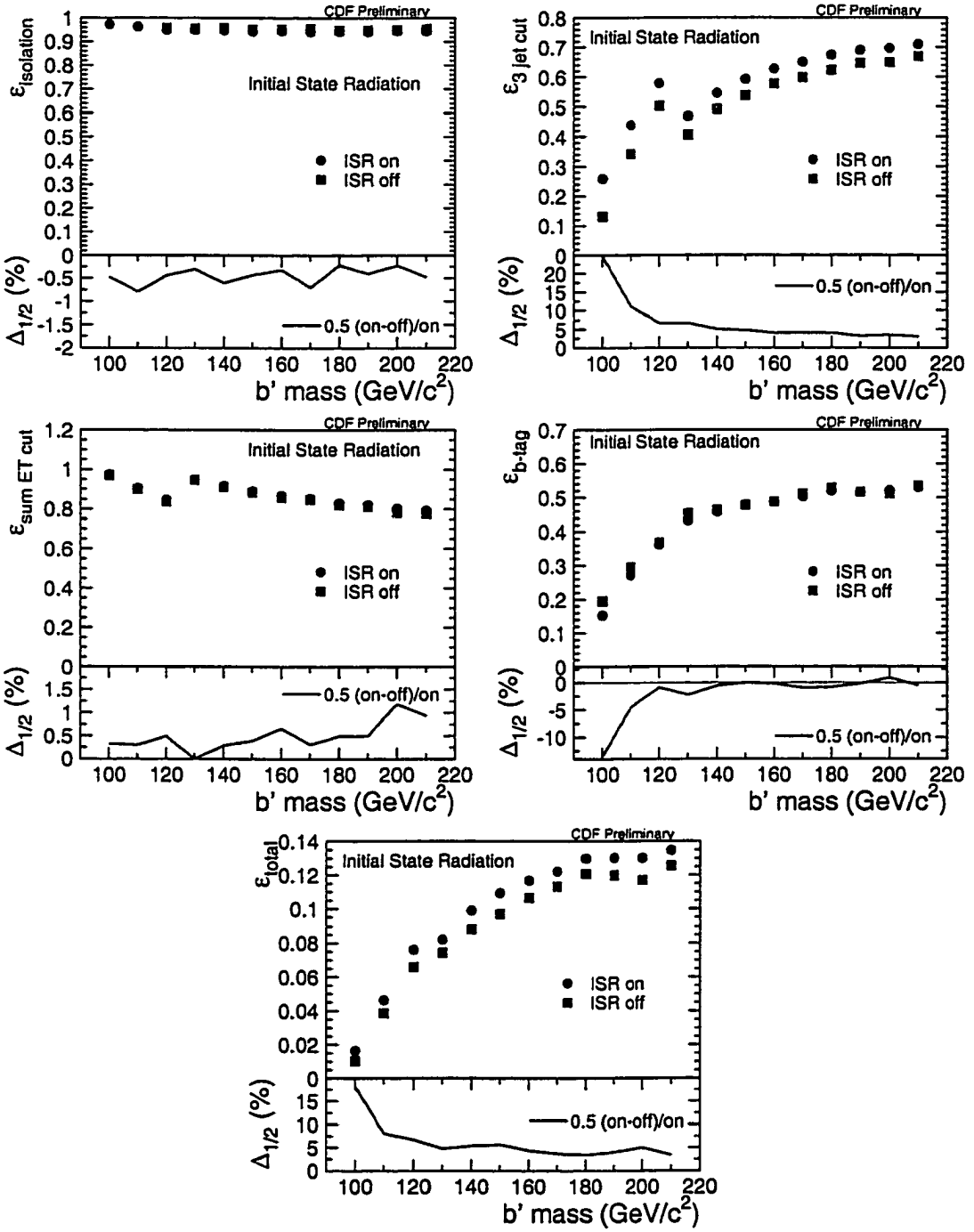

Figure 5.6: Initial-state gluon radiation effect on several efficiencies in the electron channel. Each efficiency is plotted for ISR on and ISR off. The line graph shows the half-percentage difference between the two cases. The bottom-right plot shows the collective effect on the total efficiency.

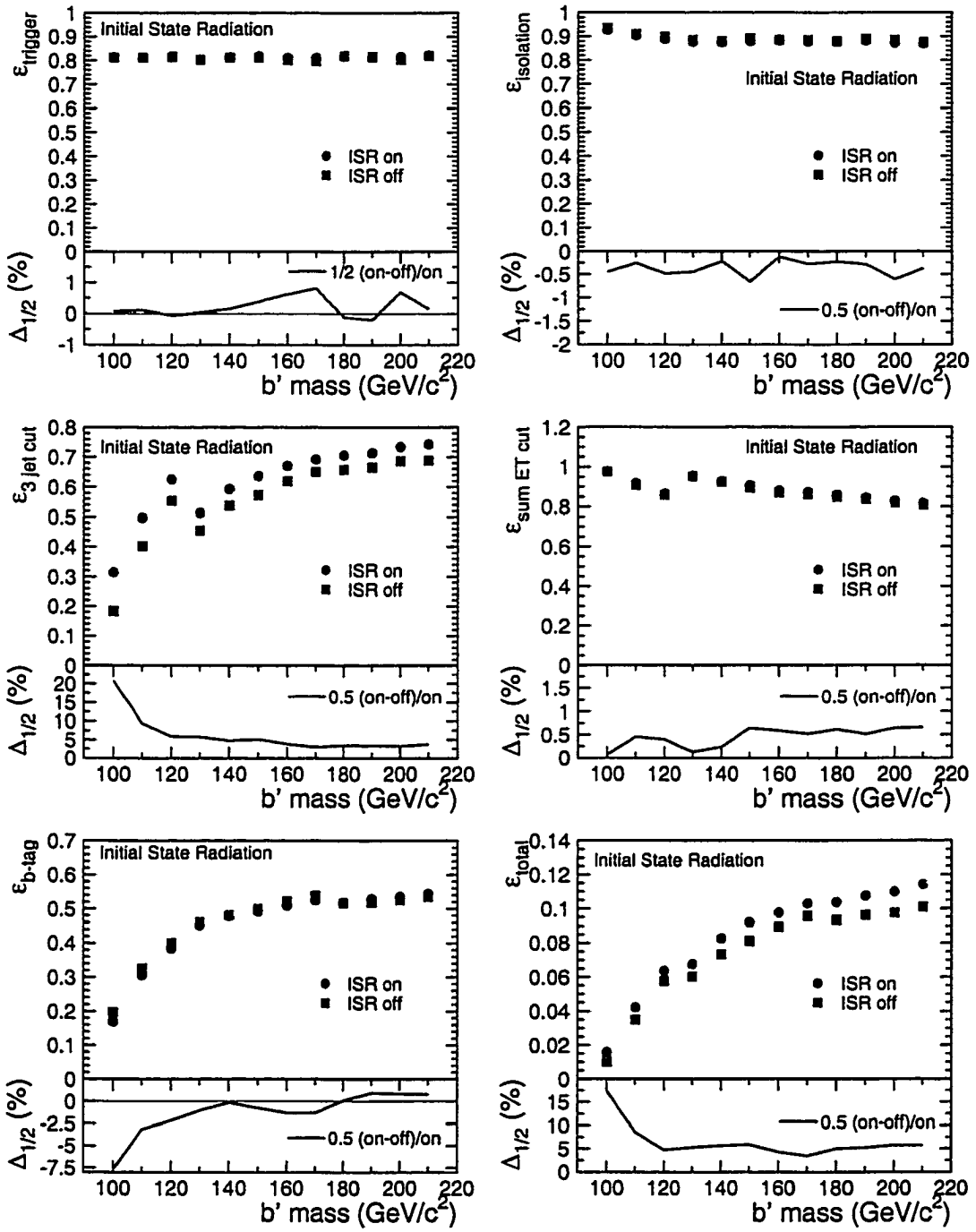

Figure 5.7: Initial-state gluon radiation effect on several efficiencies in the muon channel. Each efficiency is plotted for ISR on and ISR off. The line graph shows the half-percentage difference between the two cases. The bottom right plot shows the collective effect on the total efficiency.

the total efficiency. We use the values shown in the line plot to estimate this systematic uncertainty.

$m_{b'}$ [GeV/c^2]	Events with ISR/FSR partons with $p_T > 7$ GeV [%]	
	ISR	FSR
110	66	4.2
120	65	4.1
140	65	4.4
160	64	4.2

Table 5.1: Percentage of b' Monte Carlo events that have ISR/FSR energetic enough to be seen in the detector.

5.3 Parton Distribution Function

The parton distribution function used in the signal Monte Carlo has some influence on the final-state kinematics of the simulated events. The Monte Carlo samples used for the $b'\bar{b}'$ acceptance calculation were created with the MRSD0′ parton distribution function [52] (PDF). To study the effect of the PDF choice, we created new Monte Carlo samples using different parton distribution functions: GRV 94HO, MTB1, CTEQ 2MS and HMRS B [73]. These structure functions were chosen because they yield results that agree within 3σ with the CDF measurement of the W charge asymmetry [27].

Using these new samples, we calculated the signal acceptance times efficiency for $m_{b'} = 100$ GeV and $m_{b'} = 140$ GeV. The variation of the product of the Z^0 acceptance and the kinematic efficiencies was always within ±5%. The largest variation was 4.8% between the HMRS B and the MRSD0′ for $m_{b'} = 100$ GeV. We have also observed that in general the choice of the PDF had a larger influence at the lower b' mass. We will however assume a 5% systematic uncertainty independent of the b' mass. The PDF systematic uncertainty should be similar in both the muon and electron channel.

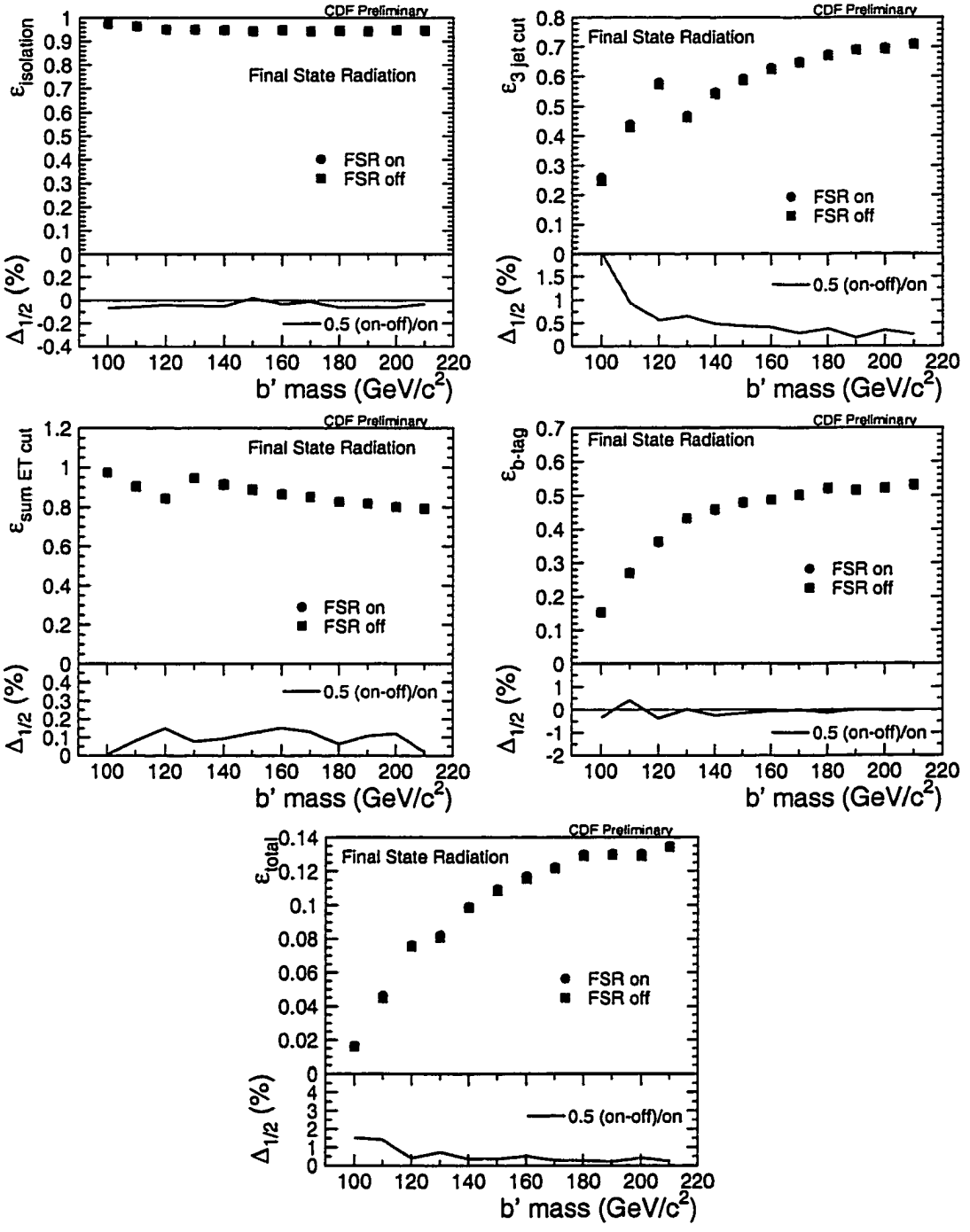

Figure 5.8: Final-state gluon radiation effect on several efficiencies in the electron channel. Each efficiency is plotted for FSR on and FSR off. The line graph shows the half-percentage difference between the two cases. The bottom right plot shows the collective effect on the total efficiency.

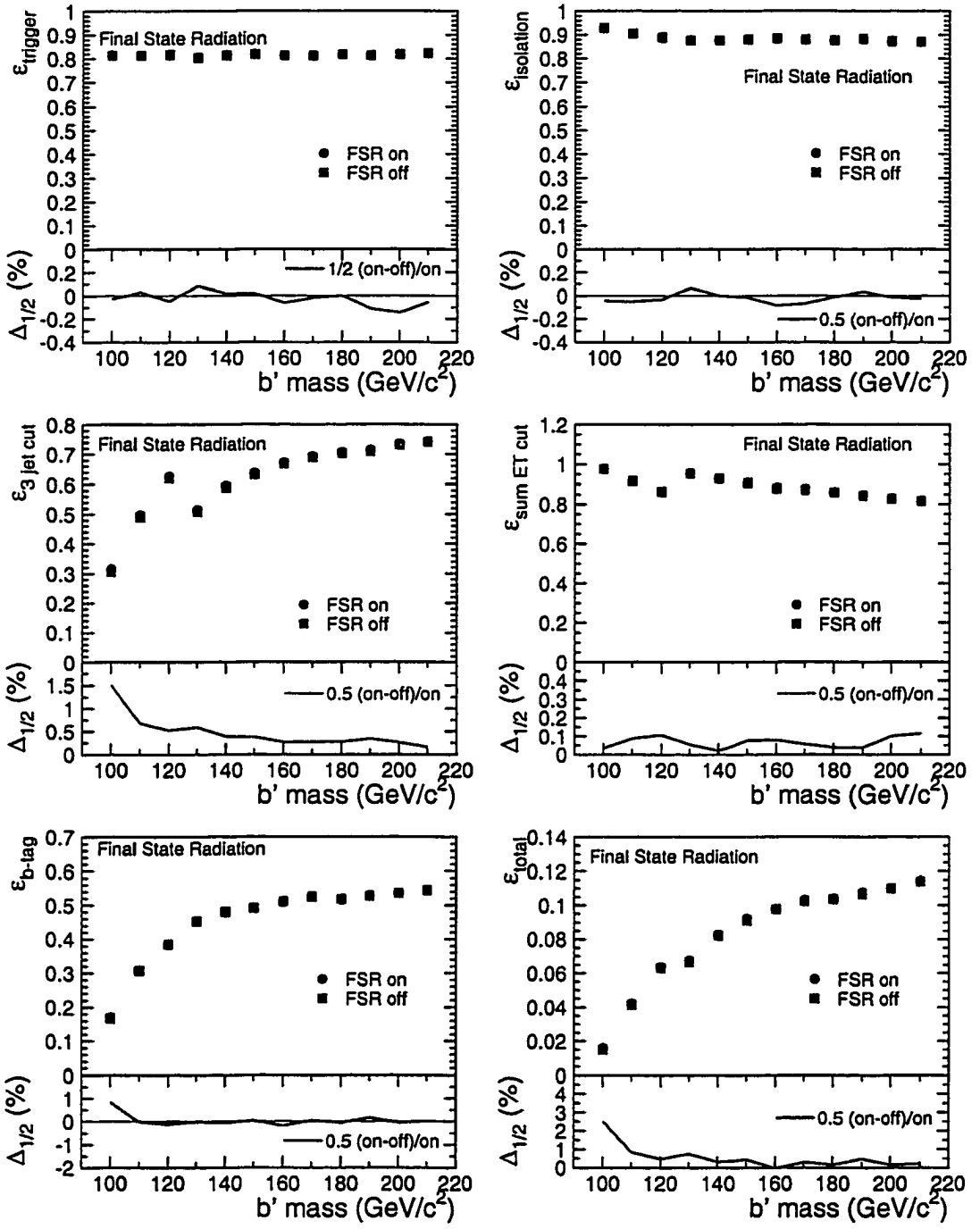

Figure 5.9: Final-state gluon radiation effect on several efficiencies in the muon channel. Each efficiency is plotted for FSR on and FSR off. The line graph shows the half-percentage difference between the two cases. The bottom right plot shows the collective effect on the total efficiency.

5.4 b-tagging

The Silicon Vertex detector b-tagging efficiency is measured from the signal Monte Carlo. Since the Monte Carlo simulation is not perfect, the efficiency is corrected by a scale factor, SF_{b-tag} that accounts for the difference in the b-tagging efficiency when the tagging algorithm is applied to data or Monte Carlo events. The correct value of the scale factor and its associated uncertainty have been a source of much controversy within CDF. In this analysis, we used the latest measurement of the scale factor which has recently been adopted by the collaboration. Its value per b-jet is 1.25 ± 0.13 [65, 66].

The uncertainty includes ± 0.07 for statistical uncertainty from both the data and Monte Carlo, plus the systematic uncertainty from QCD. A systematic uncertainty of ± 0.04 has been assigned to a potential E_T-dependence of the scale factor. Finally, a ± 0.02 systematic uncertainty results from the uncertainty in the rate of gluon splitting in the HERWIG Monte Carlo used to calculate SF_{b-tag}. All these errors are added linearly resulting in a very conservative systematic uncertainty estimation of $\pm 10\%$.

5.5 Total Systematic Uncertainty

The most important systematic uncertainties that affect the determination of the b' acceptance were described in the previous sections. We show in Tables 5.2 and 5.3 the summary of our estimate for all systematic uncertainties. The uncertainty in the luminosity measurement has been recently reevaluated by the CDF collaboration [74]. The luminosity was measured using two telescopes of beam-beam counters to an accuracy of 4.1%. Other systematic uncertainties independent of the b' mass originate from lepton identification, lepton isolation cut, primary vertex cut and the trigger efficiency. We assign a systematic uncertainty of 4% to the electron identification efficiency. The muon identification uncertainty of 5% includes the effect of the cosmic ray removal algorithm (3% uncertainty). The trigger efficiency uncertainty is particularly large in the muon channel due to the use of prescaled triggers and jet triggers. The systematic uncertainties due to the signal Monte

Carlo statistics are shown in Table 5.4. The uncertainties are larger for small b' masses due to the lower b-tag efficiency. The large Monte Carlo samples allowed us to make a better estimation of the gluon radiation and the jet-energy scale systematics.

The total systematic uncertainty on the b' acceptance times efficiency is given in Tables 5.2 and 5.3. The total uncertainty is larger for low mass b' quarks due mainly to the large uncertainty arising from the Monte Carlo modeling of the initial state radiation. The values change in the electron channel from 28.5% for $m_{b'} = 100$ GeV/c^2 to 19.2% for $m_{b'} = 210$ GeV/c^2 and in the muon channel from 27.4% to 19.2% for the same b' masses.

$Z^0 \rightarrow e^+e^-$ channel	Systematic uncertainties [%]			
	$m_{b'}$ [GeV/c^2]			
	100	110	120	130 - 210
Luminosity	4.1			
Jet-energy scale	16	13	12	12
Gluon radiation: ISR	19	9	7	6
FSR	3	2	2	2
PDF	5			
Z-vertex	2.4			
Trigger	1			
Lepton-id	4			
Isolation	4			
b-tag	10			
MC statistics	2.7	2.0	1.5	1.4 - 1.3
Total	28.5	20.9	19.5	19.2

Table 5.2: Summary of our estimate for all systematical uncertainties that affect the determination of the b' total acceptance in the electron channel.

$Z^0 \to \mu^+\mu^-$ channel	Systematic uncertainties [%]			
	$m_{b'}$ [GeV/c^2]			
	100	110	120	130 - 210
Luminosity	4.1			
Jet-energy scale	14	12	11	11
Gluon radiation: ISR	18	9	6	6
FSR	3	2	2	2
PDF	5			
Z-vertex	2.4			
Trigger	5			
Lepton-id	5			
Isolation	4			
b-tag	10			
MC statistics	2.8	2.0	1.6	1.5 - 1.3
Total	27.4	21.1	19.4	19.4

Table 5.3: Summary of our estimate for all systematical uncertainties that affect the determination of the b' total acceptance in the muon channel.

$m_{b'}$ [GeV/c^2]	Monte Carlo statistical uncertainties [%]			
	Before b-tag		Total	
	$Z^0 \to e^+e^-$	$Z^0 \to \mu^+\mu^-$	$Z^0 \to e^+e^-$	$Z^0 \to \mu^+\mu^-$
100	0.99	1.04	2.8	2.8
110	0.92	1.00	2.0	2.0
120	0.79	0.88	1.5	1.6
130	0.85	0.93	1.4	1.5
140	0.78	0.85	1.3	1.4
150	0.77	0.84	1.3	1.4
160	0.78	0.86	1.3	1.4
170	0.79	0.86	1.3	1.3
180	0.79	0.87	1.3	1.4
190	0.79	0.87	1.3	1.3
200	0.82	0.88	1.3	1.3
210	0.81	0.94	1.3	1.4

Table 5.4: Systematic uncertainty due to the signal Monte Carlo statistics for both the electron and muon samples.

Chapter 6

Background

The pair production of b' quarks and their subsequent decay into bZ^0 results in a very distinct signature: a lepton pair with an invariant mass close to m_Z, four jets and at least two b quarks. The only non-negligible background to the $b' \rightarrow bZ$ process is from Z^0 production with associated QCD hadronic jets. An example of one such process is given in Figure 6.1.

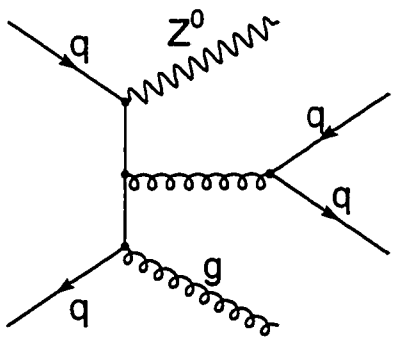

Figure 6.1: Sample Feynman diagram for Z^0 production associated with 3 jets.

The signature of Z^0 + multijets events is similar to the b' signal under study. There are, however, two major differences. First, the background events usually have a very low content of heavy flavor as opposed to the two b jets from the b' quark decays. Second, the jets from Z^0 + multijets events are usually less energetic than the ones in the b' signal.

The selection criteria discussed in Chapter 3 were designed to reduce the background by exploiting these differences. Additionally, the Z^0 + multijets processes are higher-order QCD processes and therefore their production cross section is small. After the b-tag requirement we expect a very small contribution from background. Thus, we assume that all detected events are signal and do not subtract background in the limit calculation. The background estimates described in this chapter are only used to understand event rates, the shape of kinematic distributions and establish the selection criteria.

This background is estimated using a combination of the VECBOS [70] and HERWIG Monte Carlo programs. We have made a Monte Carlo sample of inclusive Z^0 plus three or more jets generated with VECBOS + HERWIG and simulated with the fast CDF detector simulation program. VECBOS makes the calculation of the leading-order matrix elements for the $Z^0 + 3$ partons process. We use the MRSDO′ parton distribution functions [52], and the QCD renormalization and factorization scales of $Q^2 = \langle p_T \rangle^2$, where $\langle p_T \rangle$ is the average p_T of the generated partons. In addition, the Z^0 + partons events are generated with following input parameters:

- Outgoing partons:

  $p_T > 6$ GeV/c

  $|\eta| < 2.5$

  $\Delta R > 0.4$ between partons

- One lepton with:

  $p_T > 12$ GeV

  $|\eta| < 2.5$

After the VECBOS generation, a partial higher-order correction to the tree-level diagrams is obtained by including gluon radiation and hadronic fragmentation using the HERWIG shower simulation algorithm [68]. The Z^0 boson events with hadron showers are then introduced into QFL (v3.61) for the CDF detector response simulation, and the resulting jets are identified and selected the same way as in the data and signal Monte Carlo simulation.

We have generated about 37.5 million weighted events which after the unweighting procedure were reduced to approximately 82500 events; using the cross section reported by VECBOS, these correspond to a total luminosity of 4.36 fb^{-1}. We use this luminosity to normalize the background Monte Carlo. It is well known that the VECBOS cross section has a very large uncertainty. However, we do not include the background estimations in the limit calculation and therefore the overall normalization is not of great importance.

We compare the Z^0 + jets background with the data distributions after imposing the following minimal 3-jet selection:

- 2 jets $E_T > 15$ GeV, $|\eta| < 2$
- 3rd jet $E_T > 7$ GeV, $|\eta| < 2$

Figure 6.2 and Figure 6.3 show the jet-E_T distributions from the background Monte Carlo and data in the electron and muon channels, respectively. The E_T distribution from the two most energetic jets is shown in the left histogram. The right histogram shows the E_T of the third jet in the event. Figure 6.4 and Figure 6.5 compare the jet multiplicity in the background and data after the 3-jet cut. There is very good agreement between data and background in all these distributions. The agreement is actually even good in the overall normalization. This is not suprising because other studies have shown that similar Monte Carlo samples, generated with the same $Q^2 = \langle p_T \rangle^2$, agree well with the $Z^0 \rightarrow e^+e^-$+ jets data from CDF [71].

As we have seen in Chapter 3, our event selection cuts depend on the b' mass being considered, and they were devised to reduce the background content in the final data samples. The number of background events, in the electron and muon channel, that survive each main selection criteria is given in Table 6.1 and Table 6.2, for the cuts corresponding to the different b' masses indicated. The background expectations, after the 3-jet and the $\sum E_T^{jets}$ cuts, are compared to the number of events observed in the electron and muon data in Figure 6.6. The number of events decreases for more massive b' quarks because the $\sum E_T^{jets}$ cut increases with the b' mass. The discontinuity from $m_{b'} = 120$ GeV/c^2 to

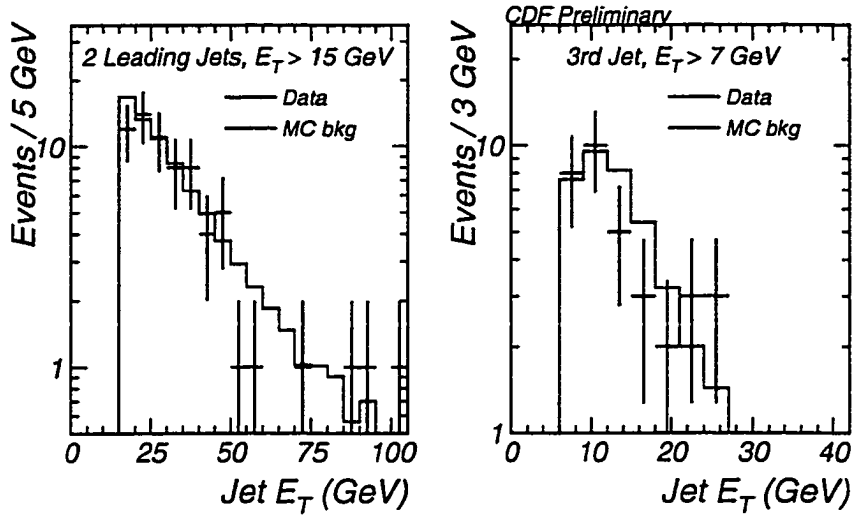

Figure 6.2: Comparison of the jet-E_T distributions of background and data, in the electron channel. The left plot shows the distribution for the two most energetic jets, while the right plot shows the third most energetic jet in the event.

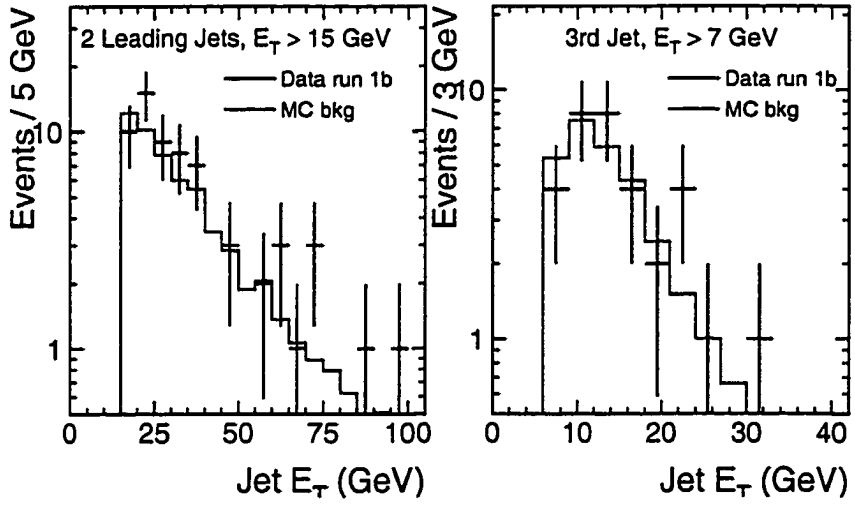

Figure 6.3: Comparison of the jet-E_T distributions of background and data, in the muon channel. The left plot shows the distribution for the two most energetic jets, while the right plot shows the third most energetic jet in the event.

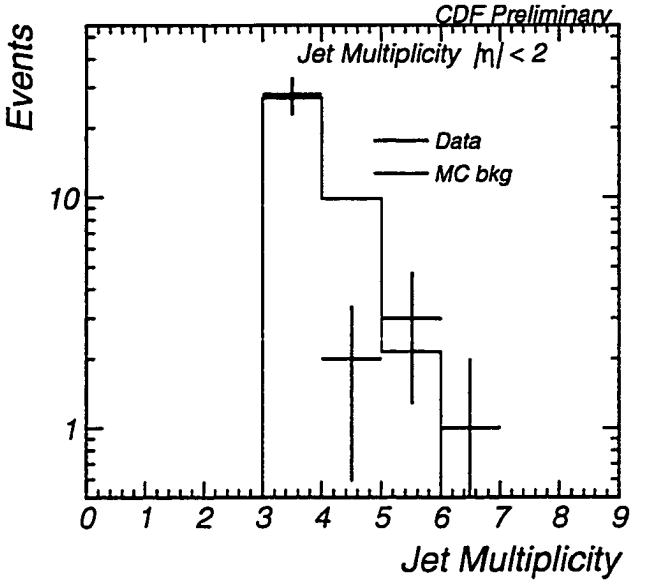

Figure 6.4: Comparison of the multiplicity distributions of the background Monte Carlo sample with electron data after the minimal 3-jet cut.

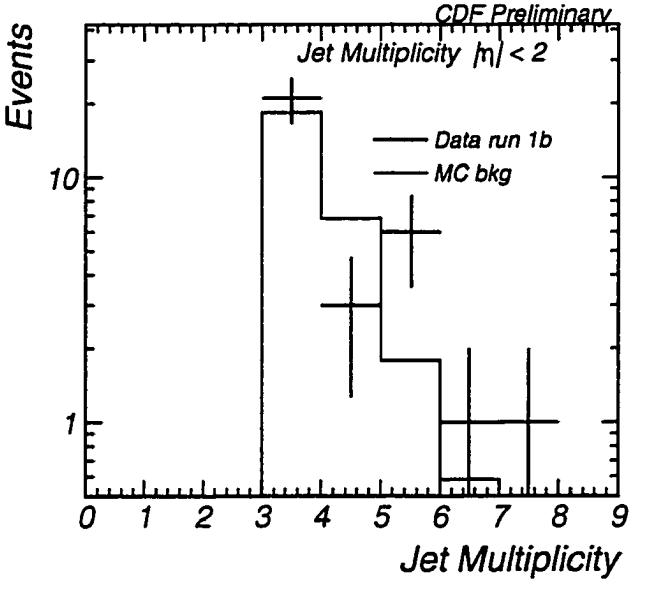

Figure 6.5: Comparison of the multiplicity distributions of the background Monte Carlo sample with muon data after the minimal 3-jet cut.

$m_{b\ell} = 130$ GeV/c^2 is due to the different E_T requirement on the third jet. The agreement between the background expectations and the data is very good.

$m_{b\ell}$ (GeV/c^2)	Background in the $Z^0 \to e^+e^-$ channel		
	Selection criteria		
	3-jet	3-jet + $\sum E_T$	3-jet + $\sum E_T$ + b-tag
100		36.1 ± 0.7	1.09 ± 0.12
110	39.8 ± 0.7	30.2 ± 0.6	0.94 ± 0.12
120		24.9 ± 0.6	0.81 ± 0.11
130		11.4 ± 0.4	0.44 ± 0.08
140		9.8 ± 0.4	0.38 ± 0.07
150	13.6 ± 0.4	8.3 ± 0.3	0.33 ± 0.07
160		6.8 ± 0.3	0.27 ± 0.06
170		5.3 ± 0.3	0.21 ± 0.06
180		4.5 ± 0.2	0.18 ± 0.05
190		3.6 ± 0.2	0.14 ± 0.05
200		2.9 ± 0.2	0.12 ± 0.04
210		2.4 ± 0.2	0.09 ± 0.04

Table 6.1: Number of expected background events in the electron channel after each specified cut, normalized to the data luminosity; errors are statistical only.

Since VECBOS does not generate heavy flavor, we estimate the b-tag rate in Z^0 plus jet events directly from data using a technique developed for the top analysis[1] [69]. In this method, we assume that the observed b-tag rate in an inclusive jet sample is the same as in the Z^0 + jets background, and apply the b-tag rates measured in the inclusive jet sample, parametrized by the event $\sum E_T^{jets}$ and the E_T and track multiplicity of each jet, to the jets of the background events that pass all the other selection criteria. This technique overestimates the background because the inclusive jet sample contains heavy-quark contributions from direct production, gluon splitting and flavor excitation while heavy quarks in Z^0 + jets events are produced mainly from gluon splitting. The background expectations after the b-tag requirement are shown in Table 6.1 and Table 6.2. We expect approximately one background event per lepton channel for $m_{b\ell} < 130$ GeV/c^2 and less than half event for

[1]We estimate the b-tag rate directly from data using the b-tag background parametrization method (SEC_FAKE) [69] instead of the SECVTX algorithm.

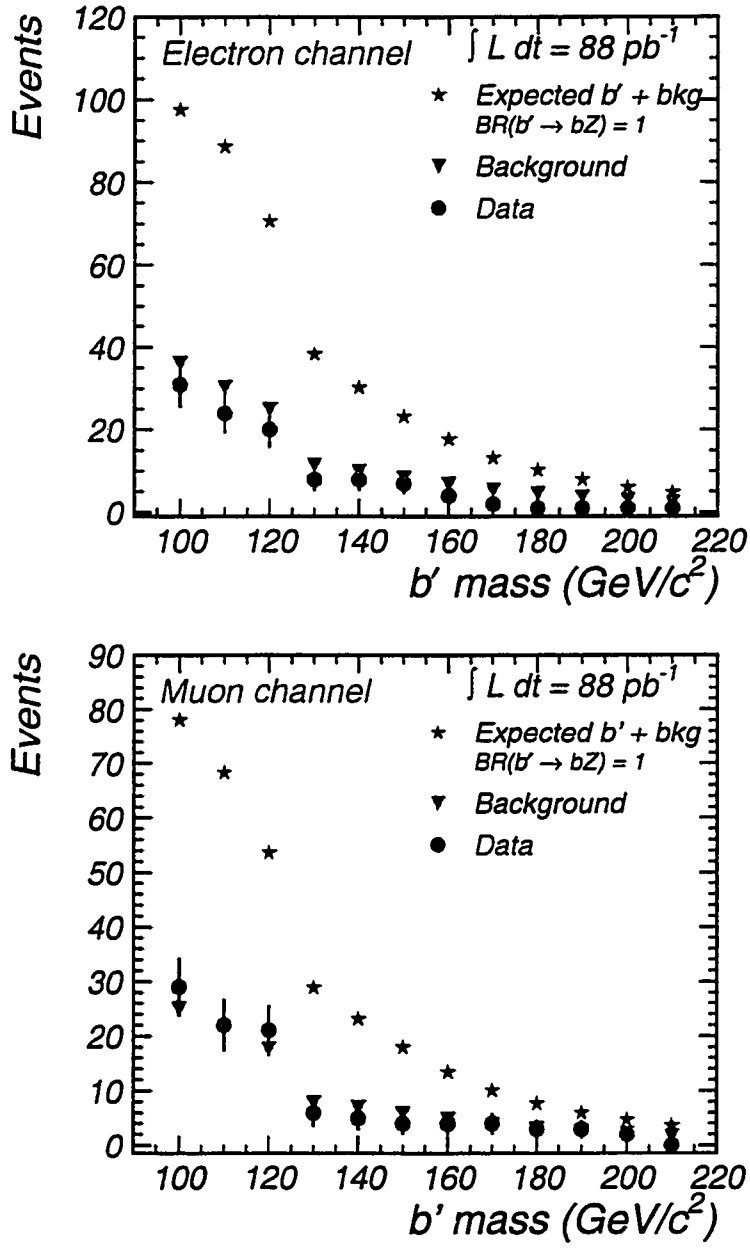

Figure 6.6: Expected number of events from signal and background before the b-tag requirement compared to data as function of b' mass. The errors are statistical only. Top: $Z^0 \to e^+e^-$ channel; Bottom: $Z^0 \to \mu^+\mu^-$ channel.

$m_{b'}$ [GeV/c^2]	Background in the $Z^0 \to \mu^+\mu^-$ channel		
	Selection criteria		
	3-jet	3-jet + $\sum E_T$	3-jet + $\sum E_T$ + b-tag
100		25.0 ± 0.6	1.01 ± 0.12
110	27.6 ± 0.6	21.2 ± 0.5	0.91 ± 0.11
120		17.6 ± 0.5	0.80 ± 0.10
130		7.7 ± 0.3	0.40 ± 0.07
140		6.9 ± 0.3	0.38 ± 0.07
150	9.3 ± 0.4	5.8 ± 0.3	0.32 ± 0.07
160		4.8 ± 0.2	0.27 ± 0.06
170		3.7 ± 0.2	0.21 ± 0.05
180		2.9 ± 0.2	0.17 ± 0.05
190		2.5 ± 0.2	0.15 ± 0.04
200		2.1 ± 0.2	0.13 ± 0.04
210		1.6 ± 0.2	0.10 ± 0.04

Table 6.2: Number of expected background events in the muon channel after each specified cut, normalized to the data luminosity; errors are statistical only.

more massive b' quarks.

A final possible background is W + jets events in which the W decays into $e\nu$ and there is an extra fake electron. The invariant mass of both "electrons" can fall in the Z^0 mass window producing a false Z^0 event. This kind of event should have higher missing transverse energy, $\not\!\!E_T$, than a Z^0 event due to the presence of the neutrino. To check this contamination of our $Z^0 \to e^+e^-$ sample we plot the $\not\!\!E_T$ distribution for data and compared it with the Z^0 + jets Monte Carlo in Figure 6.7. To use our Monte Carlo, we required the presence of at least three jets in the event: two jets with $E_T > 15$ GeV and the third with $E_T > 7$ GeV, with $|\eta| < 2$ for all the three jets. The Monte Carlo and data distributions are very similar, therefore we conclude that this background does not constitute a major contribution to our data sample.

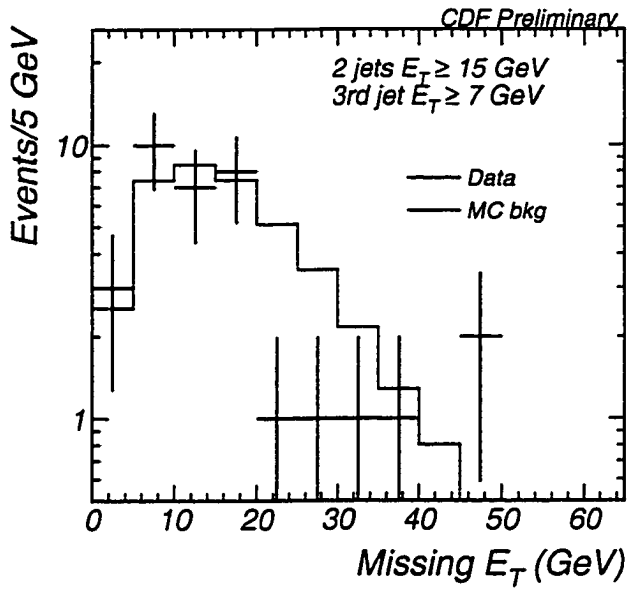

Figure 6.7: Comparison of the missing E_T in data and in our Z^0 + jets background.

Chapter 7

Search Results

The major goal of every search analysis is to find a signal of new physiscs. However, more often than not, it is found that the data are consistent with the Standard Model expectations and do not support the new physics hypothesis being considered. Unfortunately, this analysis is not an exception to this rule.

In this chapter, we will start by comparing the number of events observed in our data sample with the b' signal expectations. Given that the b' quark hypothesis is not confirmed, we will calculate an upper limit on $\sigma_{p\bar{p}\to b'\bar{b}'} \times [BR(b' \to bZ^0)]^2$. Making reasonable assumptions for $BR(b' \to bZ^0)$, a lower limit on b' mass is derived. The limit is obtained using a Bayesian calculation and checked against frequentist methods. In both cases we take in consideration the correlation between the acceptance uncertainties of the muon and electron channels. We finish with a short discussion of the final results.

7.1 Signal Estimation

For each leptonic channel studied, the expected number of signal events for a given b' mass is calculated using the equation

$$N^{exp}_{b'\bar{b}'}(m_{b'}) = \sigma_{p\bar{p}\to b'\bar{b}'}(m_{b'}) \times [BR(b' \to bZ^0)]^2 \times \mathcal{F}[BR(Z^0)] \times (A \cdot \epsilon) \times \int \mathcal{L}dt, \quad (7.1)$$

where the theoretical b' pair-production cross section $\sigma_{p\bar{p}\to b'\bar{b}'}(m_{b'})$ at a certain b' mass is equal to the top cross section $\sigma_{p\bar{p}\to t\bar{t}}(m_t)$ at the same mass, $m_t = m_{b'}$. Also, $(A \cdot \epsilon)$ is

the total acceptance times efficiency from Table 7.1, $\int \mathcal{L}dt$ is the integrated luminosity, and $\mathcal{F}[BR(Z^0)]$ is a function of the Z^0 branching ratio,

$$\mathcal{F}[BR(Z^0)] = 2 \times BR(Z^0 \to anything) \times BR(Z^0 \to l^+l^-) = 6.73\% \qquad (7.2)$$

In this equation, the factor of two accounts for the presence of two Z^0 bosons in the final state, doubling the probability that one will decay into electrons or muons.

$m_{b'}$	$(A \cdot \epsilon)$	
(GeV/c^2)	$Z^0 \to e^+e^-$	$Z^0 \to \mu^+\mu^-$
100	1.65	1.59
110	4.62	4.21
120	7.62	6.37
130	8.22	6.76
140	9.91	8.27
150	10.9	9.20
160	11.7	9.77
170	12.2	10.3
180	13.0	10.4
190	13.0	10.8
200	13.0	11.0
210	13.5	11.4

Table 7.1: Final acceptance times efficiency in the electron and muon channels as a function of the b' mass. These numbers are reproduced from Table 4.12 and Table 4.13.

The number of expected signal events after the main selection requirements is given in Tables 7.2 and 7.3 for the electron and muon channels respectively. After all the selection criteria, the number of b' events that we expect to observe in the electron channel, within the b' mass range studied, varies from 17.5 ± 0.3 to 1.34 ± 0.02. In the muon channel, we expect a range of 15.3 ± 0.3 to 1.15 ± 0.02 signal events depending on the b' mass. The decrease of the b' signal expectations as a function of the b' mass is due to the decrease of the b' pair-production cross section $\sigma_{p\bar{p}\to b'\bar{b}'}(m_{b'})$.

The signal expectations are shown in Figure 7.1 together with the events observed in the Z^0 data sample given in Table 3.4. After the b-tag requirement, we do not observe

$m_{b'}$ [GeV/c^2]	Expected signal events ($Z^0 \to e^+e^-$ channel)		
	Selection cuts		
	3-jet	3-jet + $\sum E_T^{jets}$	3-jet + $\sum E_T^{jets}$ + b-tag
100	63.0 ± 0.6	61.4 ± 0.6	10.0 ± 0.3
110	64.6 ± 0.6	58.5 ± 0.5	16.8 ± 0.3
120	54.0 ± 0.4	45.7 ± 0.4	17.5 ± 0.3
130	28.4 ± 0.2	26.9 ± 0.2	12.3 ± 0.2
140	22.3 ± 0.2	20.4 ± 0.2	9.89 ± 0.12
150	16.8 ± 0.1	14.9 ± 0.1	7.57 ± 0.10
160	12.6 ± 0.2	10.9 ± 0.1	5.63 ± 0.07
170	9.28 ± 0.07	7.91 ± 0.07	4.21 ± 0.05
180	7.06 ± 0.05	5.85 ± 0.05	3.23 ± 0.04
190	5.26 ± 0.04	4.31 ± 0.03	2.35 ± 0.03
200	3.91 ± 0.03	3.14 ± 0.03	1.74 ± 0.02
210	3.00 ± 0.02	2.38 ± 0.02	1.34 ± 0.02

Table 7.2: Expected number of signal events in the electron channel after each main selection requirements. The 3-jet requirement is different for $m_{b'} \leq 120$ GeV/c^2 and $m_{b'} > 120$ GeV/c^2 and the $\sum E_T^{jets}$ cut scales with the b' mass. The errors are statistical only.

$m_{b'}$ [GeV/c^2]	Expected signal events ($Z^0 \to \mu^+\mu^-$ channel)		
	Selection cuts		
	3-jet	3-jet + $\sum E_T^{jets}$	3-jet + $\sum E_T^{jets}$ + b-tag
100	54.3 ± 0.6	53.1 ± 0.6	9.6 ± 0.3
110	51.3 ± 0.5	47.1 ± 0.5	15.3 ± 0.3
120	41.7 ± 0.3	36.0 ± 0.3	14.6 ± 0.2
130	22.2 ± 0.2	21.2 ± 0.2	10.1 ± 0.2
140	17.5 ± 0.1	16.2 ± 0.1	8.26 ± 0.11
150	13.4 ± 0.1	12.2 ± 0.1	6.36 ± 0.09
160	9.92 ± 0.08	8.72 ± 0.08	4.71 ± 0.06
170	7.30 ± 0.06	6.37 ± 0.06	3.55 ± 0.05
180	5.48 ± 0.04	4.71 ± 0.04	2.58 ± 0.04
190	4.11 ± 0.03	3.47 ± 0.03	1.94 ± 0.03
200	3.13 ± 0.02	2.59 ± 0.02	1.47 ± 0.02
210	2.44 ± 0.02	1.99 ± 0.02	1.15 ± 0.02

Table 7.3: Expected number of signal events in the muon channel after each main selection requirements. The 3-jet requirement is different for $m_{b'} \leq 120$ GeV/c^2 and $m_{b'} > 120$ GeV/c^2 and the $\sum E_T^{jets}$ cut scales with the b' mass. The errors are statistical only.

any candidate events in the electron channel. In the muon channel, there is one candidate event that passes our cuts for b' masses below 130 GeV/c^2. The event has a third jet with E_T = 8.3 GeV which fails the jet-E_T requirement of E_T > 15 GeV for $m_{b'} \geq$ 130 GeV. Therefore, we do not observe any events for the cuts corresponding to $m_{b'} \geq$ 130 GeV. Also shown in Figure 7.1 is the Z^0 + jets background estimations from Table 6.1 and Table 6.2. We expect from both lepton channels approximately two background events for $m_{b'} \leq$ 120 GeV/c^2 and less than one event for $m_{b'}$ > 120 GeV/c^2, in agreement with the number of events observed in the data. Since the data are consistent with the Standard Model background and not with the b' quark signal that we were searching for, we proceed to calculate an upper limit on the b' pair-production cross section times branching ratio.

7.2 Limit Calculation

Since the number of observed events is small, they are distributed according to Poisson statistics. In a given channel, the probability of observing a certain number of events n_0 when μ are expected is given by

$$P(n_0;\mu) = \frac{e^{-\mu}\mu^{n_0}}{n_0!}. \tag{7.3}$$

In our analysis we treat all observed events as candidate events and do not subtract background. In this case, the total number of expected events is the same as the number of events from the signal, $\mu = N^{exp}_{b'\bar{b'}}$. To simplify the equations that follow, we redefine ϵ as the product between the total acceptance times efficiency and the leptonic branching ratio of the Z^0, $\epsilon = 2(A \cdot \epsilon)BR(Z^0 \rightarrow l^+l^-)$. We also define the total number of b' events produced which decay into the $b\bar{b}Z^0Z^0$ channel as $N^{ZZ}_{b'\bar{b'}} = \mathcal{L}\sigma_{b'\bar{b'}}BR(b' \rightarrow bZ^0)^2$. This way, we can write,

$$\mu = N^{exp}_{b'\bar{b'}} = \epsilon N^{ZZ}_{b'\bar{b'}}. \tag{7.4}$$

In order to incorporate the systematic uncertainties on the acceptance into the upper limit estimation, the Poisson distribution is convoluted with the acceptance probability

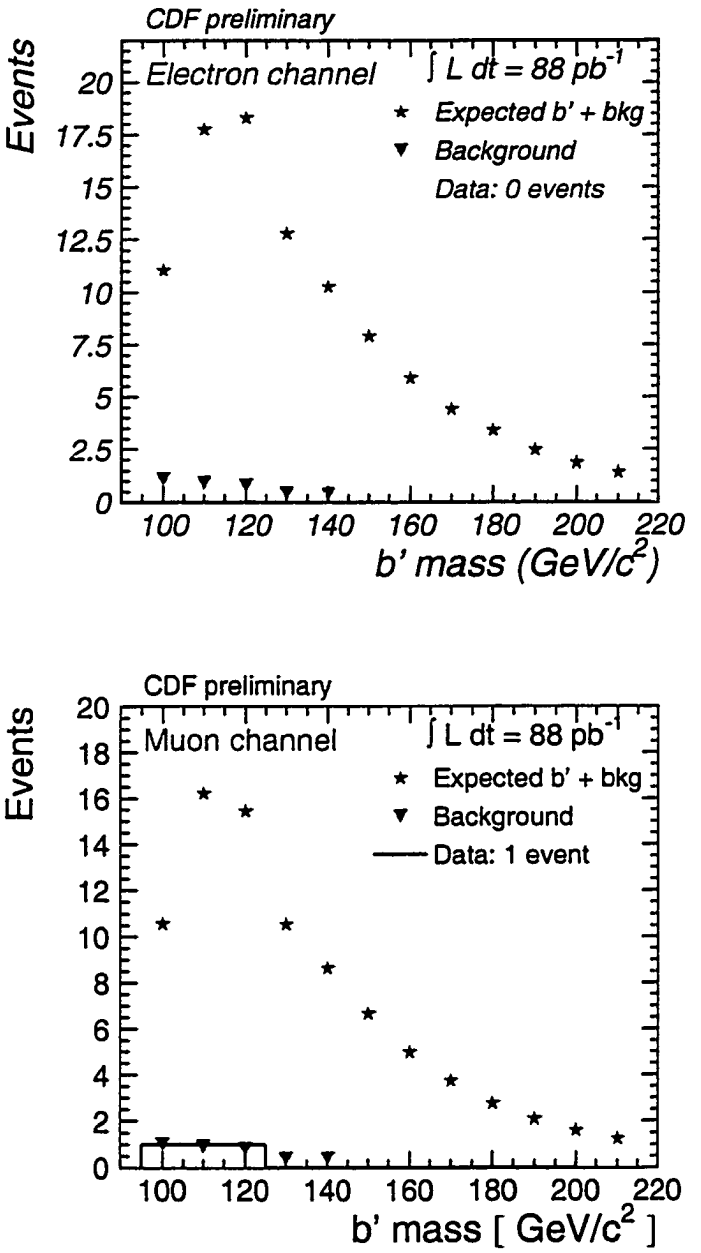

Figure 7.1: Expected number of events as function of b' mass after all selection criteria. Also shown are the data and the expected background. The errors are statistical only. Top: Electron channel; Bottom: Muon channel.

distribution, which is assumed to be a Gaussian with mean ϵ and width σ_ϵ. Thus, the probability distribution function (pdf) for the number of observed events is given by

$$\hat{\mathcal{P}}\left(n_0; \epsilon N_{b'\bar{b}'}^{Z\bar{Z}}\right) = \int_0^\infty P\left(n_0; \epsilon' N_{b'\bar{b}'}^{Z\bar{Z}}\right) \otimes G\left(\epsilon'; \epsilon, \sigma_\epsilon\right) d\epsilon'. \tag{7.5}$$

If we make two independent measurements of the same quantity, *i.e.* using the electron and muon channels, the joint likelihood of observing n_1 followed by n_2 events is

$$\mathcal{L} = \hat{\mathcal{P}}\left(n_1; \epsilon_1 N_{b'\bar{b}'}^{Z\bar{Z}}\right) \hat{\mathcal{P}}\left(n_2; \epsilon_2 N_{b'\bar{b}'}^{Z\bar{Z}}\right). \tag{7.6}$$

In this case, the correlation between the systematic uncertainties of the two measurements needs to be taken into account. We assume that the uncertainty in the acceptance can be decomposed into two parts, a fully correlated uncertainty σ_{ϵ^c} and totally uncorrelated uncertainty σ_{ϵ^u}:

$$G\left(\epsilon_i^l; \epsilon_i, \sigma_{\epsilon_i}\right) = G\left(\epsilon_i^{lc}; \epsilon_i^c, \sigma_{\epsilon_i^c}\right) G\left(\epsilon_i^{lu}; \epsilon_i^u, \sigma_{\epsilon_i^u}\right). \tag{7.7}$$

For the purpose of the limit calculation we consider that the following uncertainties are fully correlated between the two lepton channels:

- Luminosity
- Jet energy scale
- Gluon radiation
- Parton distribution function
- z_{vertex} efficiency
- Isolation efficiency
- b-tag efficiency

while the following uncertainties are considered totally uncorrelated,

- Trigger efficiency

- Lepton identification
- Monte Carlo statistics

From the systematic uncertainties in Tables 5.2 and 5.3 we obtain the correlated and uncorrelated uncertainty values shown in Table 7.4.

$m_{b'}$	correlated $(\delta\sigma_{\epsilon_i^c})$[%]		uncorrelated $(\delta\sigma_{\epsilon_i^u})$[%]	
(GeV/c^2)	$Z^0 \to e^+e^-$	$Z^0 \to \mu^+\mu^-$	$Z^0 \to e^+e^-$	$Z^0 \to \mu^+\mu^-$
100	28.1	26.3	4.9	7.6
110	20.4	19.8	4.6	7.3
120	19.0	18.0	4.4	7.2
130	18.6	18.0	4.4	7.2
140	18.6	18.0	4.3	7.2
150	18.6	18.0	4.3	7.2
160	18.6	18.0	4.3	7.2
170	18.6	18.0	4.3	7.2
180	18.6	18.0	4.3	7.2
190	18.6	18.0	4.3	7.2
200	18.6	18.0	4.3	7.2
210	18.6	18.0	4.3	7.2

Table 7.4: Correlated and uncorrelated systematic uncertainties in both lepton channels as a function of b' mass.

7.2.1 Combined Limit - Bayesian Approach

The application of Bayesian methods to the determination of confidence level limits has been extensively described in the literature [75, 76]. Here, we extend the method to the calculation of combined limits. In this method, we consider the same likelihood function as in Equation 7.6, which includes the proper treatment of the systematic uncertainties correlations:

$$\mathcal{L}(f) = \int_0^\infty d\epsilon'_e \int_0^\infty d\epsilon'_\mu P\left(n_e; \epsilon_e f\right) \otimes G\left(\epsilon'_e; \epsilon_e, \sigma_{\epsilon_e}\right) P\left(n_\mu; \epsilon_\mu f\right) \otimes G\left(\epsilon'_\mu; \epsilon_\mu, \sigma_{\epsilon_\mu}\right) \quad (7.8)$$

To simplify the notation, we define $N_{b'\overline{b'}}^{ZZ} \equiv f$. The quantity f must be common to both channels and represents the physical quantity that is to be measured. In our case, we can

take f as the number of b' events produced and decaying in the $b\bar{b}Z^0Z^0$ channel[1]. The luminosity will be factored out to obtain the 95% C.L. limit on $\sigma_{p\bar{p}\to b'\bar{b}'} \times BR(b' \to bZ^0)^2$.

Using Bayes's theorem, we can write the posterior probability distribution function for f as

$$\mathcal{P}(f|n_e, n_\mu) = \frac{\mathcal{L}(f)\mathcal{P}(f)}{\int_0^\infty \mathcal{L}(f')\mathcal{P}(f')df'} \tag{7.9}$$

where $\mathcal{P}(f)$ is the prior probability distribution function. The 95% confidence level limit $f_{95\%}$ is obtained by integrating the posterior pdf between 0 and the $f = f_{95\%}$ value that satisfies the equation,

$$0.95 = \int_0^{f_{95\%}} \mathcal{P}(f'|n_e, n_\mu)df'. \tag{7.10}$$

Considering an uniform prior pdf for f, $\mathcal{P}(f) = 1$ for $f \geq 0$ and $\mathcal{P}(f) = 0$ for $f < 0$, we have

$$0.95 = \frac{\int_0^{f_{95\%}} \mathcal{L}(f'')df''}{\int_0^\infty \mathcal{L}(f')df'} \tag{7.11}$$

The combined 95% C.L. upper limit on $\sigma_{p\bar{p}\to b'\bar{b}'} \times [BR(b' \to bZ^0)]^2$ is then given by

$$\left(\sigma_{p\bar{p}\to b'\bar{b}'} \times BR(b' \to bZ^0)^2\right)_{95\%CL} = \frac{N^{ZZ}_{b'\bar{b}',95\%}}{\int \mathcal{L}dt} \tag{7.12}$$

where $N^{ZZ}_{b'\bar{b}',95\%} = f_{95\%}$ is the limit on the number of signal events determined by Bayesian method above. The limit on $\sigma_{p\bar{p}\to b'\bar{b}'} \times [BR(b' \to bZ^0)]^2$ is shown in Table 7.5 and Figure 7.2, together with the theoretical prediction, as a function of the b' mass. Since the b' production cross section for a given mass should be similar to the top qaurk cross section at the same mass, the theoretical curve is the next-to-leading-order (NLO) calculation of the top pair-production cross section [77]. In addition, the theoretical prediction assumes that b' decays 100% of the time into bZ^0. The limit on $\sigma_{p\bar{p}\to b'\bar{b}'} \times [BR(b' \to bZ^0)]^2$ is the main result of this thesis.

One should recall that this limit was obtained without subtraction of background,*i.e.* the event observed in the muon channel for $m_{b'} \leq 120$ GeV/c^2 is considered a candidate

[1]In a more general treatment, where the branching ratios into each channel are different, the branching ratios should be combined together with the acceptance for each specific channel. In that case, f would be taken as the actual production cross section.

signal event. This fact produces a somewhat higher limit in that b' mass range and explains the bump observed in the $\sigma_{p\bar{p}\to b'\bar{b}'} \times BR(b' \to bZ^0)^2$ limit plot.

Using this NLO cross section calculation and assuming that $BR(b' \to bZ^0) = 100\%$, we can convert the 95% upper limit on the $\sigma_{p\bar{p}\to b'\bar{b}'} \times [BR(b' \to bZ^0)]^2$ into a b' mass exclusion limit. We exclude the existence of a b' quark with a mass between 100 and 199 GeV/c^2.

$M_{b'}$	$\sigma_{p\bar{p}\to b'\bar{b}'} \cdot BR(b'\bar{b}' \to bZ\bar{b}Z)$(pb)	
(GeV/c^2)	95% CL upper limit	Theory [77] $\beta(b' \to bZ) = 1$
100	37.4	102.
110	10.6	61.6
120	6.51	38.9
130	3.76	25.4
140	3.10	16.9
150	2.80	11.7
160	2.62	8.16
170	2.50	5.83
180	2.41	4.21
190	2.37	3.06
200	2.35	2.26
210	2.26	1.68

Table 7.5: The combined 95% CL upper limit on $\sigma_{p\bar{p}\to b'\bar{b}'} \times BR(b' \to bZ^0)^2$ obtained using both the high-p_T electron and muon data. This is the main result of this thesis.

In Figure 7.3, we present the 95% CL upper limit on the $b' \to bZ^0$ branching ratio. The curve is obtained from the 95% CL limit on the $\sigma_{p\bar{p}\to b'\bar{b}'} \times [BR(b' \to bZ^0)]^2$ and assuming the theoretical NLO pair-production cross section from Ref. [77]. The branching ratio limit excludes a b' quark that decays into bZ^0 with a branching ratio larger than the 95% upper limit independently of the existence of other decay modes. This statement is actually conservative because the search is also sensitive to other b' decay channels such as $b' \to bH$ or $b' \to cW^-$ as long $BR(b' \to bZ)$ is not negligible, since the hadronic decays of the H or W are kinematically similar to those of the Z. The most interesting case is the

decay $b' \to bH$ where the Higgs is light. As long as the $BR(b' \to bZ^0)$ is not negligible this signal should be covered by our search for most of the parameter space because such a Higgs boson would decay predominately into $b\bar{b}$. However, if we conservatively assume no sensitivity to these decay modes, the excluded mass range can be obtained directly from Figure 7.3. For instance, for $BR(b' \to bZ) \geq 50\%$, we exclude a b' mass from 104 GeV to 152 GeV. A more detailed account of this issue is given in Section 7.4.

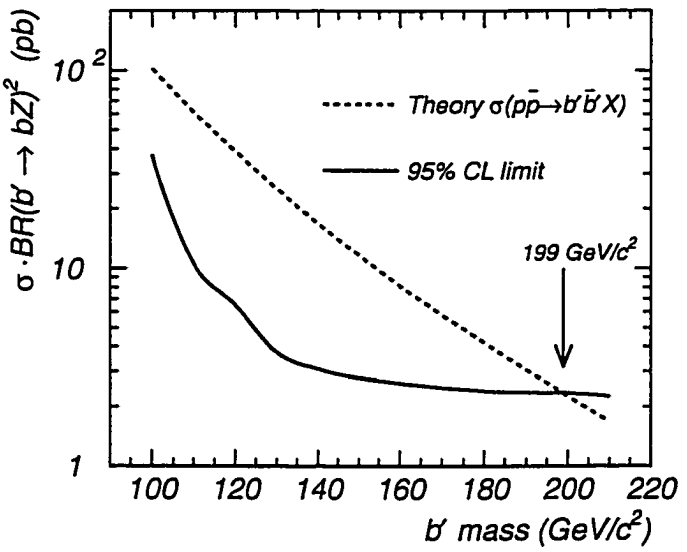

Figure 7.2: The 95% confidence level upper limit on $p\bar{p} \to b'\bar{b}'X$ production cross section times the $b' \to bZ^0$ branching ratio squared (solid). The dashed curve shows the predicted $\sigma_{p\bar{p}\to b'\bar{b}'} \times [BR(b' \to bZ^0)]^2$ with the NLO production cross section from Ref. [77] and $BR(b' \to bZ^0) = 1$.

7.3 Verification with Frequentist Methods

There is some disagreement about the preferred method for calculating upper limits: Bayesian or frequentist. In this section, we check the b' limit, obtained above with the Bayesian calculation, using a frequentist approach.

In this approach, the upper limit at a confidence level α is defined such that, if

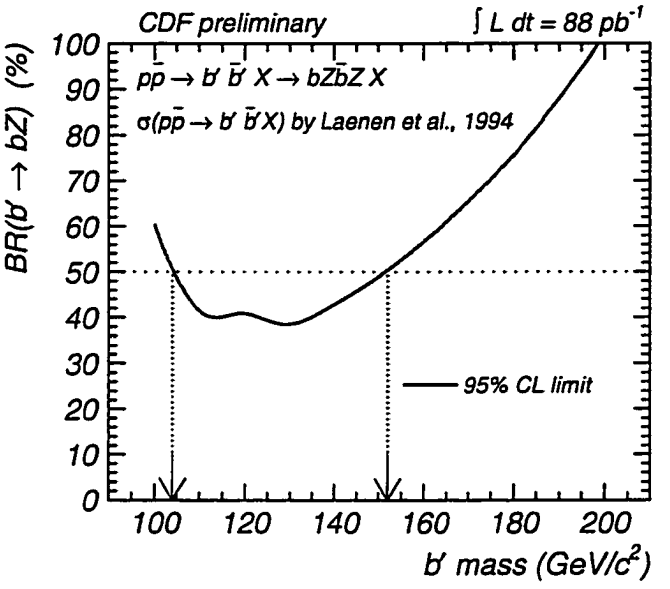

Figure 7.3: The 95% CL upper limit on the $b' \to bZ^0$ branching ratio obtained assuming the pair production cross section from Ref. [77] and using the Bayesian approach described in the text.

a experiment is repeated a very large number of times, the fraction of experiments that observe a value equal or smaller than the measured value is less than $1-\alpha$, if the real value of the quantity being measured is above the upper limit.

We consider the same joint likelihood as in the Bayesian method, Equation 7.6. This likelihood can be evaluated using Monte Carlo techniques. We have used an improved version of the POISSON program [78] to perform the calculation. In this version we have implemented the algorithm explained below to account for correlated uncertainties with different magnitude for each channel, and have also increased the precision of the calculation.

The Monte Carlo calculation throws a large number of pseudo-experiments for a given rate of events $N^{ZZ}_{b'\bar{b}'} = N_0$. In each pseudo-experiment, the acceptance in each channel, i, is drawn from two Gaussian distributions as shown in Equation 7.7. To calculate the correlated part of the uncertainty for each pseudo-experiment we start by drawing one random number from a Gaussian of zero mean and unit width. This number is then multiplied by the relative correlated systematic uncertainty $\delta\sigma_{\epsilon^c_i}$ corresponding to each channel,

$\delta'_{\epsilon_i^c} = 1 + \delta\sigma_{\epsilon_i^c} \cdot G(0;1)$. In this way we create two random numbers that are drawn from Gaussians of different widths but are totally correlated. The uncorrelated fraction of the uncertainty is drawn from different Gaussian distributions for each channel, $\delta'_{\epsilon_i^u} = G(1;\delta\sigma_{\epsilon_i^u})$. The acceptance ϵ'_i for each pseudo-experiment is then obtained from $\epsilon'_i = \epsilon_i \cdot \delta'_{\epsilon_i^u} \cdot \delta'_{\epsilon_i^c}$ where ϵ_i is the acceptance mean value for channel i.

7.3.1 Frequentist Method - Total Rate

The mean number of expected observed events for each channel μ_i is determined from the above acceptance. The number of observed events for each pseudo-experiment n'_i is drawn from a Poisson distribution with mean μ_i. We use the total rate of events from both channels to set the 95% CL limit[2]. Therefore, we compare the sum of n'_i from both channels $n' = n'_1 + n'_2$, with the total number of events observed in the data (zero or one depending on the b' mass). By performing a large number of pseudo-experiments using this procedure, we determine the fraction of pseudo-experiments that have n' less or equal to the number observed in the data for a given value of $N^{ZZ}_{b'\bar{b}'}$. The 95% CL upper limit corresponds to the $N^{ZZ}_{b'\bar{b}'}$ rate for which this fraction is smaller or equal to 0.05.

The combined 95% C.L. upper limit on $\sigma_{p\bar{p}\to b'\bar{b}'} \times [BR(b' \to bZ^0)]^2$ is again given by

$$\left(\sigma_{p\bar{p}\to b'\bar{b}'} \times BR(b' \to bZ^0)^2\right)_{95\%CL} = \frac{N^{ZZ}_{b'\bar{b}',95\%}}{\int \mathcal{L}dt} \tag{7.13}$$

The limit on the $\sigma_{p\bar{p}\to b'\bar{b}'} \times [BR(b' \to bZ^0)]^2$ obtained by the frequentist approach is shown on the left plot of Figure 7.5. In the right plot of the same figure, we present the 95% CL upper limit on the $BR(b' \to bZ^0)$.

The limit obtained by this method is compared to the Bayesian limit in Table 7.5 and Figure 7.4 for several values of b' mass. The results from both methods are very consistent, but as expected the Bayesian method yields a more conservative limit. The largest difference between the two methods is observed for $m_{b'} = 100$ GeV/c^2 because the systematic uncertainty is considerably larger for this particular mass (Table 7.4).

[2]The method presented here corresponds to method 4 of Ref. [78].

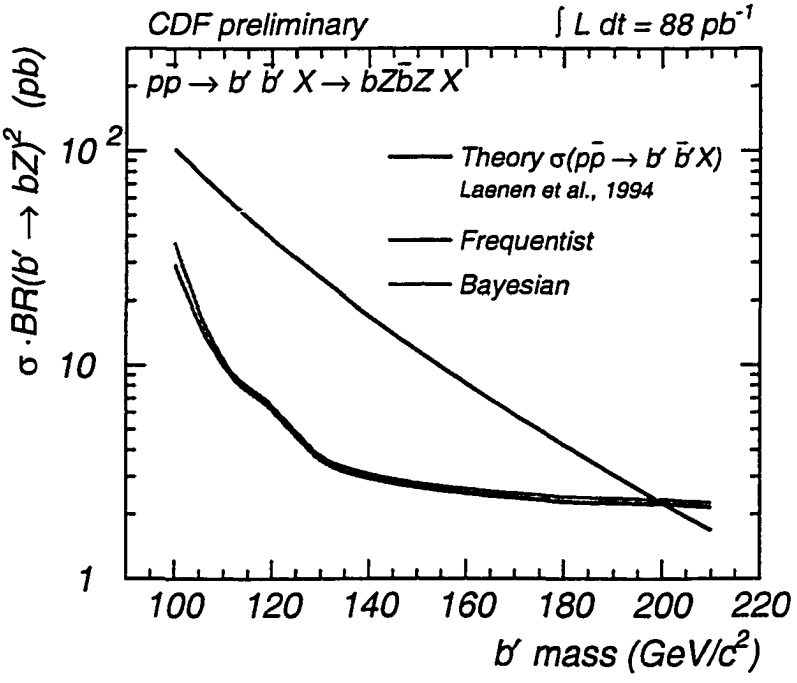

Figure 7.4: Comparison of the 95% CL upper limit on $\sigma \cdot BR(b' \to bZ^0)^2$ obtained using the Frequentist and Bayesian approaches. The theoretical curve assumes $BR(b' \to bZ^0) = 100\%$.

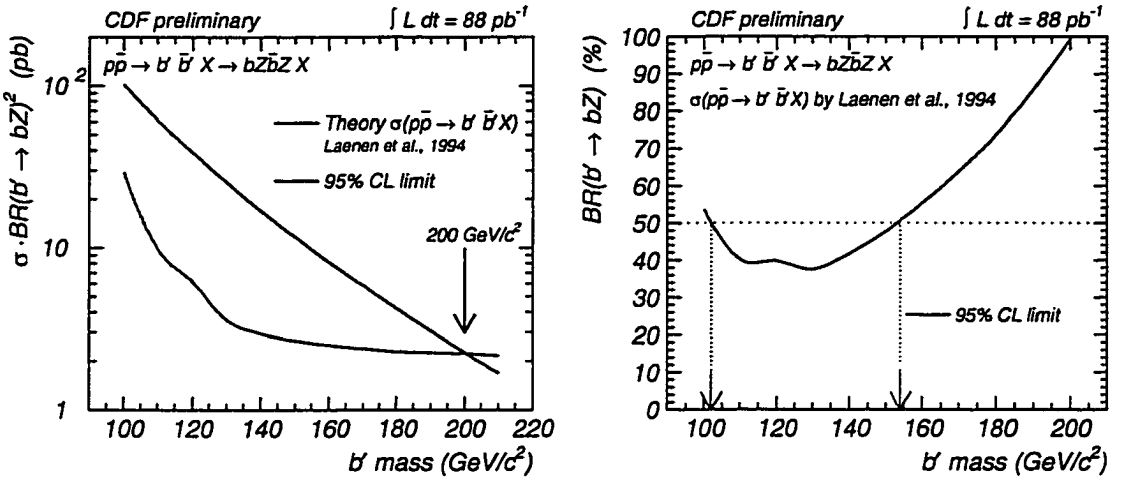

Figure 7.5: Left: 95% CL upper limit on $\sigma \cdot BR(b' \rightarrow bZ^0)^2$ obtained using the Frequentist approach applied to the total rate of events. The theoretical curve assumes $BR(b' \rightarrow bZ^0) = 100\%$. Right: 95% CL upper limit on the $b' \rightarrow bZ^0$ branching ratio obtained assuming the theoretical cross section from [77]

From the frequentist total-rate analysis, we can exclude the existence of a b' quark with a mass between 100 and 200 GeV/c^2. Remeber that, the Bayesian method yields a slightly weaker excluded mass range, $100 \leq m_{b'} \leq 199$ GeV/c^2.

7.3.2 Frequentist Method - Unique Measurements

An alternative frequentist method of calculating the limit using the information from multiples channels is to consider the measurements as unique, ignoring the total rate of observed events [78].

The method is very similar to the previous one. The measurements are assumed to be distiguishable, as above, but the limit is calculated using the probability of the outcome considering the individual observations from each channel instead of using the total rate of observed events. We use the likelihood function in Equation 7.6 and in the Monte Carlo pseudo-experiment ask for the fraction of the pseudo-experiments that would observe n_1

events in channel 1 and n_2 events in channel 2. This method will potentially give different upper limits if the data set is arbitrarily divided into separate measurements [78].

As an exercise, we have applied this method in our analysis and obtain a somewhat different 95% C.L. upper limit on $\sigma_{p\bar{p}\to b'\bar{b}'} \times BR(b' \to bZ^0)^2$. The result is compared with the two previous methods in Table 7.6. Figure 7.6 compares this method with the frequentist method that uses the total rate of events. We observe that for the b' masses where we have one candidate event, the total rate method is considerably more conservative than the unique-measurements method described in this section. The candidate event seems to have a very small effect on the upper limit when the outcome of the pseudo-experiments are considered individually and the information about the total rate is ignored.

$M_{b'}$ (GeV/c^2)	$\sigma_{p\bar{p}\to b'\bar{b}'} \cdot BR(b'\bar{b}' \to bZ\bar{b}Z)$ (pb)			
	95% CL			Theory
	Frequentist(UM)	Frequentist(TR)	Bayesian	$\beta(b' \to bZ) = 1$
100	23.0	29.5	37.4	102.
110	8.12	9.94	10.6	61.6
120	5.06	6.17	6.51	38.9
130	3.48	3.59	3.76	25.4
140	2.87	2.96	3.10	16.9
150	2.60	2.67	2.80	11.7
160	2.43	2.51	2.62	8.16
170	2.32	2.38	2.50	5.83
180	2.23	2.29	2.41	4.21
190	2.19	2.26	2.37	3.06
200	2.17	2.23	2.35	2.26
210	2.10	2.16	2.26	1.68

Table 7.6: Upper limit on $\sigma_{p\bar{p}\to b'\bar{b}'} \times BR(b' \to bZ^0)^2$ at 95% C.L. obtained using both the high-p_T electron and muon data. The calculation was performed using the three methods described in the text. Column one shows the limit obtained with the frequentist method assuming unique measurements, column two shows the frequentist limit using the total rate of events. The Bayesian upper limit is given in column three.

Following the same procedure as before we can derive b' mass exclusion regions. Assuming $BR(b' \to bZ^0) = 100\%$, we exclude a b' mass from 100 to 201 GeV/c^2. For

$BR(b' \to bZ) \geq 50\%$, the exclusion region is reduced to $100 \leq m_{b'} \leq 155$ GeV/c^2. It is interesting to note that the mass lower limit is nearly independent of the method used to calculate the limit, varying only by 2 GeV/c^2. This happens because there are no observed events for high b' masses. We conclude that the method described in this section is the least conservative of the methods studied. In particular, it seems to be too "optimistic" when applied to searches that yield a non-zero number of observed events.

We choose the Bayesian method to present the final result of this analysis, because it is a robust technique and it yields the most conservative result. It is important to notice, however, that the b' mass excluded region depends weakly on the method used to calculate the limit.

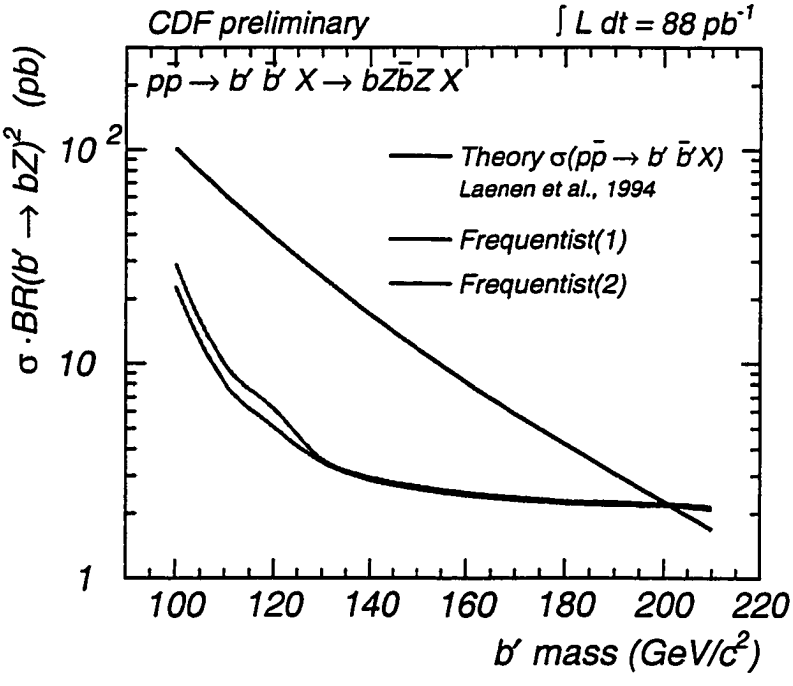

Figure 7.6: Comparison of the 95% CL upper limit on $\sigma \cdot BR(b' \to bZ^0)^2$ obtained using the two different frequentist methods. The Frequentist(1) curve corresponds to the method where the total rate of observed events is not taken into consideration. The Frequentist(2) curve shows the upper limit with the total rate method described in Section 7.3. The theoretical curve assumes $BR(b' \to bZ^0) = 100\%$.

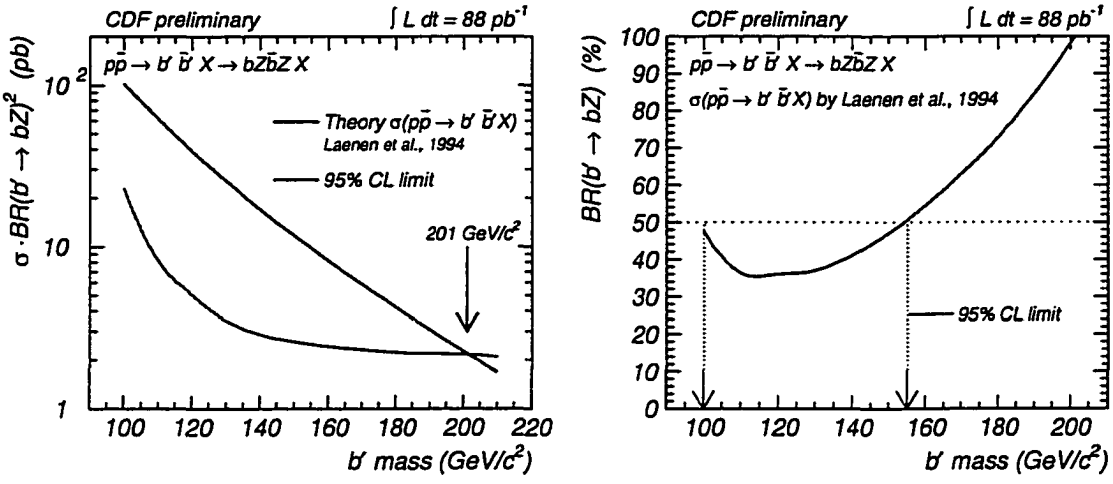

Figure 7.7: Left: 95% CL upper limit on $\sigma \cdot BR(b' \to bZ^0)^2$ obtained using the Frequentist approach applied to the individual rate of events. The theoretical curve assumes $BR(b' \to bZ^0) = 100\%$. Right: 95% CL upper limit on the $b' \to bZ^0$ branching ratio obtained assuming the theoretical cross section from reference [77].

7.4 Final Considerations

7.4.1 The Light Higgs Possibility

If a light Higgs boson, *i.e.* $m_H < 150$ GeV/c^2, exists, the branching ratio for $b' \to bH$ might not be negligible, depending on the b' mass. In this case, the assumption of $BR(b' \to bZ^0) = 100\%$ used to establish a lower limit on the b' mass would not be valid. On the other hand, the limit on $\sigma_{p\bar{p} \to b'\bar{b}'} \times [BR(b' \to bZ^0)]^2$ calculated above would actually be improved. In this section, we will give some preliminary indication of the sensitivity of our results to the existence of such Higgs boson.

The branching ratio of the $b' \to bH$ decay has been calculated as a function of the b' mass [16]. It was shown that $BR(b' \to bH)$ depends strongly on the CKM mixing angles and the Higgs, top, b' and t' masses. Fortunately, the branching ratio calculation was performed for $m_t = 175$ GeV/c^2 and, in addition, the ratio $r = BR(b' \to bH)/BR(b' \to bZ^0)$ is independent of the CKM mixing angles and mostly independent of the t' mass. The ratio r can have a wide range of values depending on the Higgs and b' masses, but unfortunately

the $b' \rightarrow bH$ branching ratio was determined only for four values of Higgs mass, $m_H = 20, m_Z, 150$ and 200 GeV/c^2. For $m_H < m_Z$, the Higgs decay mode will dominate. Due to phase space suppression, for Higgs masses above the Z^0 mass, the $b' \rightarrow bZ^0$ decay dominates up to a specific b' mass above which $b' \rightarrow bH$ prevails. In the special case that $m_H = m_Z$, the branching ratios from both channel are similar up to $m_{b'} \approx 140$ GeV/c^2.

The latest results from LEPII have established a preliminary lower limit on the Higgs mass of 105.6 GeV/c^2 at 95% confidence level [79]. Taking this experimental bound on the Higgs mass and interpolating the values given in Ref. [16], we find that the $b' \rightarrow bZ^0$ decay mode should dominate $b' \rightarrow bH$ for b' masses up to 160-170 GeV/c^2. Since we have found at 95% C.L. that $BR(b' \rightarrow bZ^0) < 50\%$ for 104 GeV $\leq M_{b'} \leq$ 152 GeV, we can conclude that a b' quark decaying by FCNC is excluded in that mass range independently of the existence of a Higgs boson.

If a Higgs boson exists and it has a mass below ~130-140 GeV/c^2, it will predominately decay into $b\bar{b}$. For heavier Higgs masses, the dominant decay will be $H \rightarrow W^*W^*$ or $H \rightarrow WW$. All these decay modes produce jets in the final state. So, as long the $BR(b' \rightarrow bZ^0)$ is not negligible, our search should be sensitive to the process $b'\overline{b'} \rightarrow b\bar{b}Z^0H$.

To demonstrate this, we have studied our acceptance to the process $b'\overline{b'} \rightarrow b\bar{b}Z^0H$. We have made Monte Carlo samples for three different values of the Higgs mass, $m_H = 100, 125$ and 150 GeV/c^2, and different values of b' masses. The acceptance times efficiency, $(A \cdot \epsilon)_{ZH}$ for this mode were calculated using the same procedure as described in Chapter 4. Table 7.7 shows the ratio $(A \cdot \epsilon)_{ZH}/(A \cdot \epsilon)_{ZZ}$ where $(A \cdot \epsilon)_{ZH}$ is the total acceptance times efficiency for the $b'\overline{b'} \rightarrow b\bar{b}Z^0Z^0$ process given in Table 7.1. The ratio was calculated only in the muon channel because it is not expected to be different in the electron channel. To obtain the final relative search sensitivity between the Z^0H and Z^0Z^0 channels, the numbers in Table 7.7 have to be divided by a factor of two to account for the fact that the Z^0H decay mode only has one Z^0 in the final state.

Eventually, knowing these acceptance for the Z^0H decay mode, one could determine confidence level limits for different Higgs masses. Unfortunately, this is not possible

$m_{b'}$ (GeV/c^2)	Ratio of $(A \cdot \epsilon)_{ZH}$ to $(A \cdot \epsilon)_{ZZ}$		
	$m_H = 100$ GeV	$m_H = 125$ GeV	$m_H = 150$ GeV
100	–	–	–
110	1.69 ± 0.06	–	–
120	1.52 ± 0.06	–	–
130	1.55 ± 0.07		–
140	1.37 ± 0.06		–
150	1.37 ± 0.06		–
160	1.39 ± 0.03	1.24 ± 0.03	0.74 ± 0.05
170	1.40 ± 0.05		0.82 ± 0.04
180	1.57 ± 0.07		0.94 ± 0.05
190	1.47 ± 0.05		1.00 ± 0.05
200	1.27 ± 0.06		1.10 ± 0.06
210	1.44 ± 0.06		0.97 ± 0.05

Table 7.7: Ratio of the final acceptance times efficiency for $b'\overline{b'} \to b\bar{b}Z^0H$ process to the one for $b'\overline{b'} \to b\bar{b}Z^0Z^0$, in the $Z^0 \to \mu^+\mu^-$ channel. The Z^0 leptonic branching ratio function, $\mathcal{F}[BR(Z^0)]$ is not included. The dashes indicate $m_{b'}$ and m_H combinations for which the decay $b' \to bH$ is kinematically forbidden.

due to the lack of theoretical information on the ratio $r = BR(b' \to bH)/BR(b' \to bZ^0)$. However, to get some feeling for how this light Higgs would affect the cross section times branching ratio and the b' mass limits, we can perform the exercise shown in Figure 7.8. We calculate the 95% C.L. limit on the $\sigma_{p\bar{p}\to b'\bar{b'}} \times [BR(b' \to bZ^0)]^2$, assuming that $BR(b' \to bH) = BR(b' \to bZ^0) = 0.5$, *i.e.* $r = 1$, independent of the b' mass. If one would neglect the Z^0H acceptance, the limit would be the conservative result, shown in the left plot of Figure 7.8, that we had already obtained in the previous section. On the other hand, if we assume the acceptance in the Z^0H channel to be 1.4 times the acceptance in the Z^0Z^0 channel (a reasonable number for a low-mass Higgs), we get the plot on the right of Figure 7.8. The theoretical expectation for the $p\bar{p} \to b'\overline{b'}X$ production cross section times the $b' \to bZ^0$ branching ratio squared is 25% the value for $BR(b' \to bZ^0) = 1$. However, the 95% confidence level upper limit on $\sigma_{p\bar{p}\to b'\bar{b'}} \times [BR(b' \to bZ^0)]^2$ was improved due to the acceptance in the Z^0H channel. In this case, we would be able to exclude a b' quark with

a mass between 100 GeV/c^2 and 170 GeV/c^2, assuming that the quark would decay 100% of the time by FCNC.

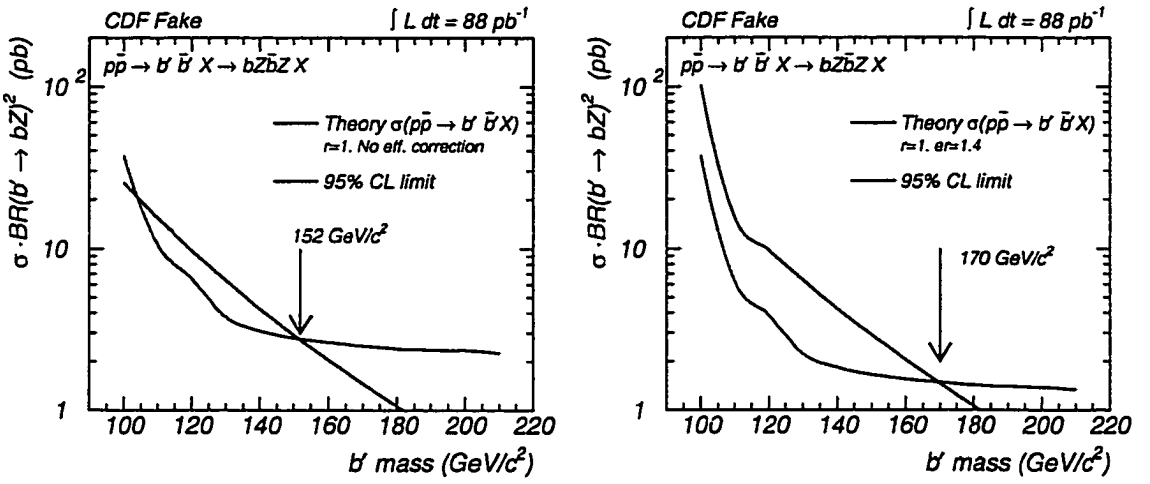

Figure 7.8: The 95% confidence level upper limit on $p\bar{p} \to b'\bar{b}'X$ production cross section times the $b' \to bZ^0$ branching ratio squared assuming that $BR(b' \to bH) = BR(b' \to bZ^0) = 0.5$. Left: Neglecting the acceptance for the Z^0H decay channel; Right: Considering that the acceptance in the Z^0H decay mode is 1.4 times the acceptance in the Z^0Z^0 channel.

7.4.2 The $b' \to tW^*$ Decay

Since the b' mass exclusion range extends above the top mass, we need to worry about the validity of the assumption that $BR(b' \to bZ^0) = 100\%$. For b' masses above the top mass, the decay channel $b' \to tW^*$ is kinematically allowed. However, it is highly suppressed by three-body phase space. In Figure 7.9 we show the ratio $BR(b' \to tW^*)/BR(b' \to bZ^0)$ as a function of the b' mass. The FCNC decay clearly dominates for b' masses up to 190 GeV/c^2. For larger masses, the ratio depends highly on the t' mass considered. For a b' mass of 200 GeV/c^2, the ratio varies from 40% for a b'-t' non-chiral doublet, to 2% for $m_{t'} = 260$ GeV/c^2. The electroweak precision data constrains the mass splitting of extra fermions and boson doublets. At 1σ and 2σ levels, this constraint gives $|m_{t'} - m_{b'}| < 38$ GeV and 93 GeV respectively [80], assuming no extra SU(2) doublets. If the extra quark is a

non-chiral isosinglet, $b' \to bZ^0$ occurs at tree-level resulting in a CC to FCNC ratio much smaller than 1% [11, 81]. We conclude that, for the entire b' mass range excluded, there is some parameter space for which the assumption that $BR(b' \to bZ^0) = 1$ is reasonable.

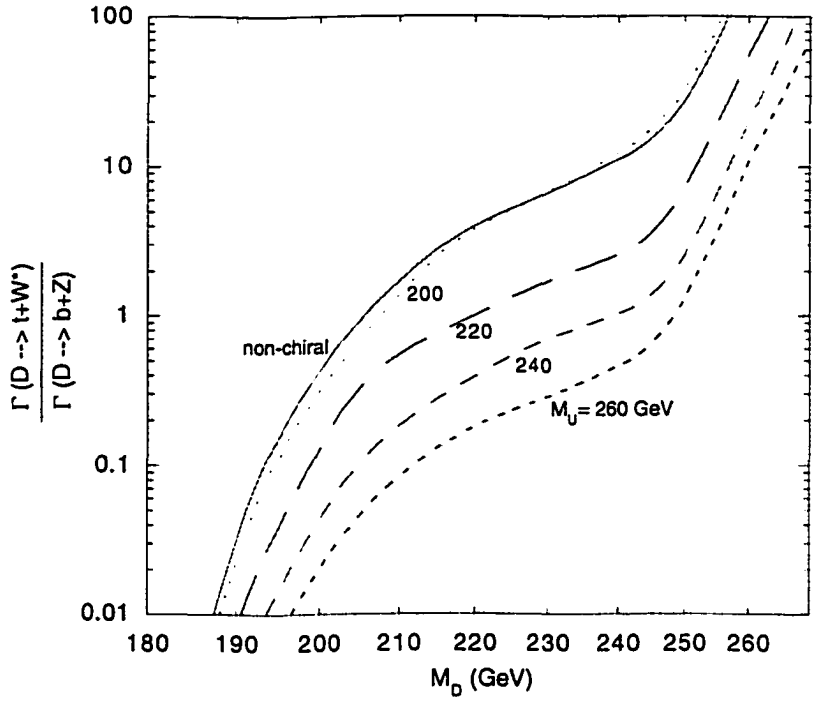

Figure 7.9: Comparison of the charge current and FCNC rates in b' decays as function of the b' mass. The case of a non-chiral isosinglet quark is not shown because the ratio is much smaller than 1% [11, 81].

Chapter 8

Conclusions

The current precision electroweak data severely constrain the existence of extra generations of fermions. Nevertheless, extra quarks are still allowed in the Standard Model and in its most popular extensions.

In this analysis, we have searched for an extra quark (b') with charge -1/3. We have searched for b'-quark pair production in $p\bar{p}$ collisions at $\sqrt{s}$ = 1.8 TeV, using 87.8 pb^{-1} of data collected with the Collider Detector at Fermilab. The favored b' decay mode depends on the CKM matrix mixing angles. The flavor-changing neutral current decays will dominate for a large set of reasonable values of the fourth-generation mixing angles. We have assumed that both b' quarks would decay by FCNC into $b' \rightarrow bZ^0$ and studied the decay mode $b'\overline{b'} \rightarrow b\bar{b}Z^0Z^0$ where one Z^0 decays into e^+e^- or $\mu^+\mu^-$ and the other decays hadronically, giving a signature of two leptons plus jets. We found one event in the muon data sample that passed all the selection criteria for a b' event. However, this is also consistent with expectations from the Standard Model background. In the absence of a signal, a 95% confidence level upper limit on $\sigma_{p\bar{p}\rightarrow b'\bar{b'}} \times [BR\,(b' \rightarrow bZ^0)]^2$ was established as a function of the b' mass. This limit is the major final result of the analysis. From this, b' mass range exclusion regions can be derived for the theoretical model of choice. The search is also sensitive to other b' decay channels such as $b' \rightarrow bH$ or $b' \rightarrow cW^-$ as long $BR(b' \rightarrow bZ)$ is not negligible, since the hadronic decays of the H or W are kinematically similar to those of the Z. The acceptance for $b'\overline{b'} \rightarrow b\bar{b}ZH$ is 1.8 to 0.5 times the acceptance for $b'\overline{b'} \rightarrow b\bar{b}ZZ$,

depending on the Higgs and b' masses and not including the $BR(Z \to l^+l^-)$. However, if we conservatively assume no sensitivity to these decay modes, we exclude a b' mass from 104 GeV to 152 GeV for $BR(b' \to bZ) \geq 50\%$. Assuming that $BR(b' \to bZ) = 100\%$, we are able to exclude at 95% C.L. b' masses from 100 GeV/c^2 up to 199 GeV/c^2.

The b' mass region excluded by this search is compared to the previously existing limits in Figure 8.1. The exclusion region in the flavor-changing neutral current channel was extended by more than a factor of two. The limit for a long-lived quark with a lifetime of $c\tau \approx 1$ cm was also extended since this search should apply to such quarks as well. Since the branching ratios of different FCNC decay channels are related by Standard Model parameters, it would be possible to derive limits on those channels using the results of this search.

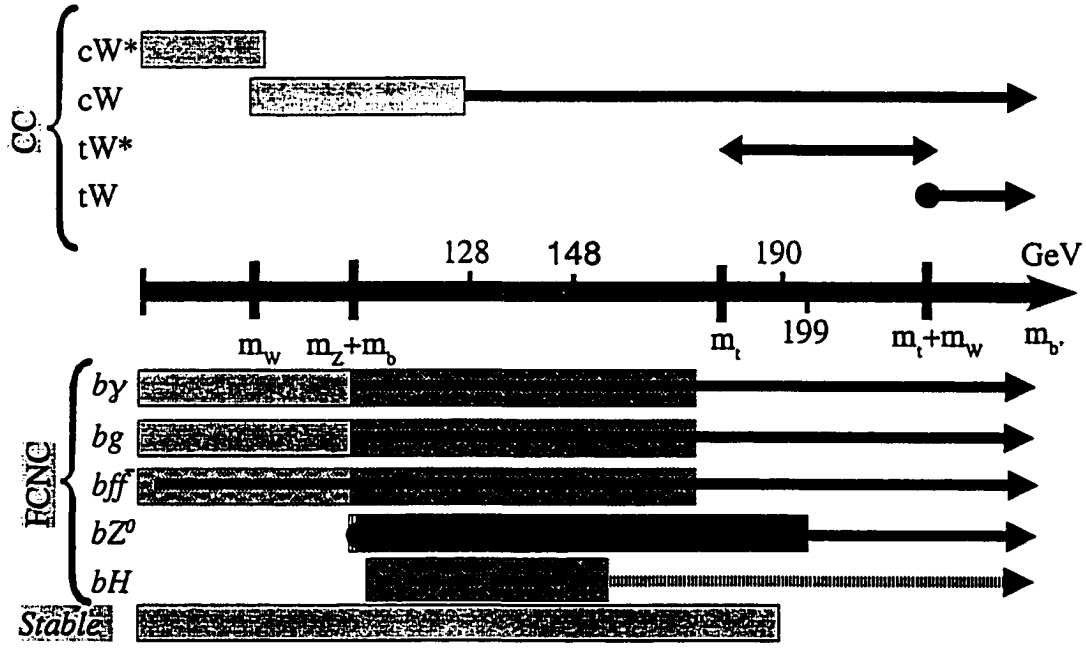

Figure 8.1: Summary of the search results. Light boxes indicate previously excluded regions. The box with vertical dashes indicates the previously excluded region for a long-lived quark. The dark box shows the b' mass range excluded by this search. The dark dashed boxes indicate exclusions that can be inferred from the results of this search.

After this search is legitimate to ask: Is there still room for a b'? Where could it be hiding? While the mass limits are reaching very large discouraging values, it is important to notice that the most important result from these searches is actually the limit on the branching ratio and not on the mass. For instance, the mass limit in the charged-current mode assumed that b' would decay 100% of the time into cW. If the CC and FCNC branching ratios are actually comparable then that limit does not apply anymore. So, for instance, there is room for a b' quark with a mass of close to the CC limit but that would decay mostly by $b' \rightarrow cW$. Of course, a b' quark heavier than 128 GeV/c^2 that decays mostly by the charged current is also still allowed. It is important to note that this region of the parameter space is difficult to exclude because of the top quark decay background.

The next run of the Tevatron, scheduled to begin in Spring 2001, will bring at least a factor of 20 more data. Besides the increased luminosity, the CDF detector has undergone a major upgrade that will result in an increased acceptance for the b' signal. The search for $b' \rightarrow bZ$ will mostly benefit from the increase in the b-tag efficiency. Most importantly, the next run will allow the search for a b' quark in the charge current mode to be extended. With a better understanding of the top signal, it will be possible to extend the $b' \rightarrow cW$ limit close to the top mass. With that result in hand, the window for a light b' quark will definitively be closed.

Appendix

The b' Search Article

Search for a Fourth-Generation Quark More Massive than the Z^0 Boson in $p\bar{p}$ Collisions at $\sqrt{s} = 1.8$ TeV

T. Affolder,[21] H. Akimoto,[43] A. Akopian,[36] M. G. Albrow,[10] P. Amaral,[7] S. R. Amendolia,[32] D. Amidei,[24] J. Antos,[1] G. Apollinari,[36] T. Arisawa,[43] T. Asakawa,[41] W. Ashmanskas,[7] M. Atac,[10] F. Azfar,[29] P. Azzi-Bacchetta,[30] N. Bacchetta,[30] M. W. Bailey,[26] S. Bailey,[14] P. de Barbaro,[35] A. Barbaro-Galtieri,[21] V. E. Barnes,[34] B. A. Barnett,[17] M. Barone,[12] G. Bauer,[22] F. Bedeschi,[32] S. Belforte,[40] G. Bellettini,[32] J. Bellinger,[44] D. Benjamin,[9] J. Bensinger,[4] A. Beretvas,[10] J. P. Berge,[10] J. Berryhill,[7] S. Bertolucci,[12] B. Bevensee,[31] A. Bhatti,[36] C. Bigongiari,[32] M. Binkley,[10] D. Bisello,[30] R. E. Blair,[2] C. Blocker,[4] K. Bloom,[24] B. Blumenfeld,[17] B. S. Blusk,[35] A. Bocci,[32] A. Bodek,[35] W. Bokhari,[31] G. Bolla,[34] Y. Bonushkin,[5] D. Bortoletto,[34] J. Boudreau,[33] A. Brandl,[26] S. van den Brink,[17] C. Bromberg,[25] N. Bruner,[26] E. Buckley-Geer,[10] J. Budagov,[8] H. S. Budd,[35] K. Burkett,[14] G. Busetto,[30] A. Byon-Wagner,[10] K. L. Byrum,[2] M. Campbell,[24] A. Caner,[32] W. Carithers,[21] J. Carlson,[24] D. Carlsmith,[44] J. Cassada,[35] A. Castro,[30] D. Cauz,[40] A. Cerri,[32] P. S. Chang,[1] P. T. Chang,[1] J. Chapman,[24] C. Chen,[31] Y. C. Chen,[1] M.-T. Cheng,[1] M. Chertok,[38] G. Chiarelli,[32] I. Chirikov-Zorin,[8] G. Chlachidze,[8] F. Chlebana,[10] L. Christofek,[16] M. L. Chu,[1] S. Cihangir,[10] C. I. Ciobanu,[27] A. G. Clark,[13] M. Cobal,[32] E. Cocca,[32] A. Connolly,[21] J. Conway,[37] J. Cooper,[10] M. Cordelli,[12] D. Costanzo,[32] J. Cranshaw,[39] D. Cronin-Hennessy,[9] R. Cropp,[23] R. Culbertson,[7] D. Dagenhart,[42] F. DeJongh,[10] S. Dell'Agnello,[12] M. Dell'Orso,[32] R. Demina,[10] L. Demortier,[36] M. Deninno,[3] P. F. Derwent,[10] T. Devlin,[37] J. R. Dittmann,[10] S. Donati,[32] J. Done,[38] T. Dorigo,[14] N. Eddy,[16] K. Einsweiler,[21] J. E. Elias,[10] E. Engels, Jr.,[33] W. Erdmann,[10] D. Errede,[16] S. Errede,[16] Q. Fan,[35] R. G. Feild,[45] C. Ferretti,[32] I. Fiori,[3] B. Flaugher,[10] G. W. Foster,[10] M. Franklin,[14] J. Freeman,[10] J. Friedman,[22] Y. Fukui,[20] S. Gadomski,[23] S. Galeotti,[32] M. Gallinaro,[36] T. Gao,[31] M. Garcia-Sciveres,[21] A. F. Garfinkel,[34] P. Gatti,[30] C. Gay,[45] S. Geer,[10] D. W. Gerdes,[24] P. Giannetti,[32] P. Giromini,[12] V. Glagolev,[8] M. Gold,[26] J. Goldstein,[10] A. Gordon,[14] A. T. Goshaw,[9] Y. Gotra,[33] K. Goulianos,[36] H. Grassmann,[40] C. Green,[34] L. Groer,[37] C. Grosso-Pilcher,[7] M. Guenther,[34] G. Guillian,[24] J. Guimarães da Costa,[24] R. S. Guo,[1] C. Haber,[21] E. Hafen,[22] S. R. Hahn,[10] C. Hall,[14] T. Handa,[15] R. Handler,[44] W. Hao,[39] F. Happacher,[12] K. Hara,[41] A. D. Hardman,[34] R. M. Harris,[10] F. Hartmann,[18] K. Hatakeyama,[36] J. Hauser,[5] J. Heinrich,[31] A. Heiss,[18] B. Hinrichsen,[23] K. D. Hoffman,[34] C. Holck,[31] R. Hollebeek,[31] L. Holloway,[16] R. Hughes,[27] J. Huston,[25] J. Huth,[14] H. Ikeda,[41] M. Incagli,[32] J. Incandela,[10] G. Introzzi,[32] J. Iwai,[43] Y. Iwata,[15] E. James,[24] H. Jensen,[10] M. Jones,[31] U. Joshi,[10] H. Kambara,[13] T. Kamon,[38] T. Kaneko,[41] K. Karr,[42] H. Kasha,[45] Y. Kato,[28] T. A. Keaffaber,[34] K. Kelley,[22] M. Kelly,[24] R. D. Kennedy,[10] R. Kephart,[10] D. Khazins,[9] T. Kikuchi,[41] M. Kirk,[4] B. J. Kim,[19] H. S. Kim,[23] S. H. Kim,[41] Y. K. Kim,[21] L. Kirsch,[4] S. Klimenko,[11] D. Knoblauch,[18] P. Koehn,[27] A. Köngeter,[18] K. Kondo,[43] J. Konigsberg,[11] K. Kordas,[23] A. Korytov,[11] E. Kovacs,[2] J. Kroll,[31] M. Kruse,[35] S. E. Kuhlmann,[2] K. Kurino,[15] T. Kuwabara,[41] A. T. Laasanen,[34] N. Lai,[7] S. Lami,[36] S. Lammel,[10] J. I. Lamoureux,[4] M. Lancaster,[21] G. Latino,[32] T. LeCompte,[2] A. M. Lee IV,[9] S. Leone,[32] J. D. Lewis,[10] M. Lindgren,[5] T. M. Liss,[16] J. B. Liu,[35] Y. C. Liu,[1] N. Lockyer,[31] J. Loken,[29] M. Loreti,[30] D. Lucchesi,[30] P. Lukens,[10] S. Lusin,[44] L. Lyons,[29] J. Lys,[21] R. Madrak,[14] K. Maeshima,[10] P. Maksimovic,[14] L. Malferrari,[3] M. Mangano,[32] M. Mariotti,[30] G. Martignon,[30] A. Martin,[45] J. A. J. Matthews,[26] P. Mazzanti,[3] K. S. McFarland,[35] P. McIntyre,[38] E. McKigney,[31] M. Menguzzato,[30] A. Menzione,[32] E. Meschi,[32] C. Mesropian,[36] C. Miao,[24] T. Miao,[10] R. Miller,[25] J. S. Miller,[24] H. Minato,[41] S. Miscetti,[12] M. Mishina,[20] N. Moggi,[32] E. Moore,[26] R. Moore,[24] Y. Morita,[20] A. Mukherjee,[10] T. Muller,[18] A. Munar,[32] P. Murat,[32] S. Murgia,[25] M. Musy,[40] J. Nachtman,[5] S. Nahn,[45] H. Nakada,[41] T. Nakaya,[7] I. Nakano,[15] C. Nelson,[10] D. Neuberger,[18] C. Newman-Holmes,[10] C.-Y. P. Ngan,[22] P. Nicolaidi,[40] H. Niu,[4] L. Nodulman,[2] A. Nomerotski,[11] S. H. Oh,[9] T. Ohmoto,[15] T. Ohsugi,[15] R. Oishi,[41] T. Okusawa,[28] J. Olsen,[44] C. Pagliarone,[32] F. Palmonari,[32] R. Paoletti,[32] V. Papadimitriou,[39] S. P. Pappas,[45] A. Parri,[12] D. Partos,[4] J. Patrick,[10] G. Pauletta,[40] M. Paulini,[21] A. Perazzo,[32] L. Pescara,[30] T. J. Phillips,[9] G. Piacentino,[32] K. T. Pitts,[10] R. Plunkett,[10] A. Pompos,[34] L. Pondrom,[44] G. Pope,[33] F. Prokoshin,[8] J. Proudfoot,[2] F. Ptohos,[12] G. Punzi,[32] K. Ragan,[23] D. Reher,[21] A. Reichold,[29] W. Riegler,[14] A. Ribon,[30] F. Rimondi,[3] L. Ristori,[32] W. J. Robertson,[9] A. Robinson,[23] T. Rodrigo,[6] S. Rolli,[42] L. Rosenson,[22] R. Roser,[10] R. Rossin,[30] W. K. Sakumoto,[35] D. Saltzberg,[5] A. Sansoni,[12] L. Santi,[40] H. Sato,[41] P. Savard,[23] P. Schlabach,[10] E. E. Schmidt,[10] M. P. Schmidt,[45] M. Schmitt,[14] L. Scodellaro,[30] A. Scott,[5] A. Scribano,[32] S. Segler,[10] S. Seidel,[26] Y. Seiya,[41] A. Semenov,[8] F. Semeria,[3] T. Shah,[22] M. D. Shapiro,[21] P. F. Shepard,[33] T. Shibayama,[41] M. Shimojima,[41] M. Shochet,[7] J. Siegrist,[21] G. Signorelli,[32] A. Sill,[39] P. Sinervo,[23] P. Singh,[16] A. J. Slaughter,[45] K. Sliwa,[42] C. Smith,[17] F. D. Snider,[10] A. Solodsky,[36] J. Spalding,[10] T. Speer,[13] P. Sphicas,[22] F. Spinella,[32] M. Spiropulu,[14] L. Spiegel,[10] L. Stanco,[30] J. Steele,[44] A. Stefanini,[32] J. Strologas,[16] F. Strumia,[13]

0031-9007/00/84(5)/835(6)$15.00

D. Stuart,[10] K. Sumorok,[22] T. Suzuki,[41] R. Takashima,[15] K. Takikawa,[41] M. Tanaka,[41] T. Takano,[28] B. Tannenbaum,[5] W. Taylor,[23] M. Tecchio,[24] P. K. Teng,[1] K. Terashi,[41] S. Tether,[22] D. Theriot,[10] R. Thurman-Keup,[2] P. Tipton,[35] S. Tkaczyk,[10] K. Tollefson,[35] A. Tollestrup,[10] H. Toyoda,[28] W. Trischuk,[23] J. F. de Troconiz,[14] S. Truitt,[24] J. Tseng,[22] N. Turini,[32] F. Ukegawa,[41] J. Valls,[37] S. Vejcik III,[10] G. Velev,[32] R. Vidal,[10] R. Vilar,[6] I. Vologouev,[21] D. Vucinic,[22] R. G. Wagner,[2] R. L. Wagner,[10] J. Wahl,[7] N. B. Wallace,[37] A. M. Walsh,[37] C. Wang,[9] C. H. Wang,[1] M. J. Wang,[1] T. Watanabe,[41] D. Waters,[29] T. Watts,[37] R. Webb,[38] H. Wenzel,[18] W. C. Wester III,[10] A. B. Wicklund,[2] E. Wicklund,[10] H. H. Williams,[31] P. Wilson,[10] B. L. Winer,[27] D. Winn,[24] S. Wolbers,[10] D. Wolinski,[24] J. Wolinski,[25] S. Worm,[26] X. Wu,[13] J. Wyss,[32] A. Yagil,[10] W. Yao,[21] G. P. Yeh,[10] P. Yeh,[1] J. Yoh,[10] C. Yosef,[25] T. Yoshida,[28] I. Yu,[19] S. Yu,[31] A. Zanetti,[40] F. Zetti,[21] and S. Zucchelli[3]

(CDF Collaboration)

[1]*Institute of Physics, Academia Sinica, Taipei, Taiwan 11529, Republic of China*
[2]*Argonne National Laboratory, Argonne, Illinois 60439*
[3]*Istituto Nazionale di Fisica Nucleare, University of Bologna, I-40127 Bologna, Italy*
[4]*Brandeis University, Waltham, Massachusetts 02254*
[5]*University of California at Los Angeles, Los Angeles, California 90024*
[6]*Instituto de Fisica de Cantabria, University of Cantabria, 39005 Santander, Spain*
[7]*Enrico Fermi Institute, University of Chicago, Chicago, Illinois 60637*
[8]*Joint Institute for Nuclear Research, RU-141980 Dubna, Russia*
[9]*Duke University, Durham, North Carolina 27708*
[10]*Fermi National Accelerator Laboratory, Batavia, Illinois 60510*
[11]*University of Florida, Gainesville, Florida 32611*
[12]*Laboratori Nazionali di Frascati, Istituto Nazionale di Fisica Nucleare, I-00044 Frascati, Italy*
[13]*University of Geneva, CH-1211 Geneva 4, Switzerland*
[14]*Harvard University, Cambridge, Massachusetts 02138*
[15]*Hiroshima University, Higashi-Hiroshima 724, Japan*
[16]*University of Illinois, Urbana, Illinois 61801*
[17]*The Johns Hopkins University, Baltimore, Maryland 21218*
[18]*Institut für Experimentelle Kernphysik, Universität Karlsruhe, 76128 Karlsruhe, Germany*
[19]*Korean Hadron Collider Laboratory, Kyungpook National University, Taegu 702-701, Korea and Seoul National University, Seoul 151-742, Korea and SungKyunKwan University, Suwon 440-746, Korea*
[20]*High Energy Accelerator Research Organization (KEK), Tsukuba, Ibaraki 305, Japan*
[21]*Ernest Orlando Lawrence Berkeley National Laboratory, Berkeley, California 94720*
[22]*Massachusetts Institute of Technology, Cambridge, Massachusetts 02139*
[23]*Institute of Particle Physics, McGill University, Montreal, Canada H3A 2T8 and University of Toronto, Toronto, Canada M5S 1A7*
[24]*University of Michigan, Ann Arbor, Michigan 48109*
[25]*Michigan State University, East Lansing, Michigan 48824*
[26]*University of New Mexico, Albuquerque, New Mexico 87131*
[27]*The Ohio State University, Columbus, Ohio 43210*
[28]*Osaka City University, Osaka 588, Japan*
[29]*University of Oxford, Oxford OX1 3RH, United Kingdom*
[30]*Universita di Padova, Istituto Nazionale di Fisica Nucleare, Sezione di Padova, I-35131 Padova, Italy*
[31]*University of Pennsylvania, Philadelphia, Pennsylvania 19104*
[32]*Istituto Nazionale di Fisica Nucleare, University and Scuola Normale Superiore of Pisa, I-56100 Pisa, Italy*
[33]*University of Pittsburgh, Pittsburgh, Pennsylvania 15260*
[34]*Purdue University, West Lafayette, Indiana 47907*
[35]*University of Rochester, Rochester, New York 14627*
[36]*Rockefeller University, New York, New York 10021*
[37]*Rutgers University, Piscataway, New Jersey 08855*
[38]*Texas A&M University, College Station, Texas 77843*
[39]*Texas Tech University, Lubbock, Texas 79409*
[40]*Istituto Nazionale di Fisica Nucleare, University of Trieste, Udine, Italy*
[41]*University of Tsukuba, Tsukuba, Ibaraki 305, Japan*
[42]*Tufts University, Medford, Massachusetts 02155*
[43]*Waseda University, Tokyo 169, Japan*
[44]*University of Wisconsin, Madison, Wisconsin 53706*
[45]*Yale University, New Haven, Connecticut 06520*

(Received 13 September 1999)

We present the results of a search for pair production of a fourth-generation charge $-\frac{1}{3}$ quark (b') in $\sqrt{s} = 1.8$ TeV $p\bar{p}$ collisions using 88 pb^{-1} of data obtained with the Collider Detector at Fermilab. We assume that both quarks decay via the flavor-changing neutral current process $b' \to bZ^0$ and that the b' mass is greater than $m_Z + m_b$. We studied the decay mode $b'\bar{b}' \to Z^0Z^0b\bar{b}$ where one Z^0 decays into e^+e^- or $\mu^+\mu^-$ and the other decays hadronically, giving a signature of two leptons plus jets. An upper limit on the $\sigma_{p\bar{p}\to b'\bar{b}'} \times [B(b' \to bZ^0)]^2$ is established as a function of the b' mass. We exclude at 95% confidence level a b' quark with mass between 100 and 199 GeV/c^2 for $B(b' \to bZ^0) = 100\%$.

PACS numbers: 13.85.Rm, 13.85.Qk, 14.65.-q

The standard model (SM) with three generations of quarks and leptons is in excellent agreement with all experimental data available today. There is no strong reason to believe that an extra fermion generation exists. However, the SM does not explain either the fermion family replication or the fermion mass hierarchy. Several models have been proposed to solve shortcomings in the SM specifically through the introduction of extra quarks and leptons. In addition, grand unification, supersymmetry, supergravity, and superstrings predict or can accommodate extra quarks [1]. An extensive discussion of such models can be found in a recent review [2].

In general, flavor-changing neutral current (FCNC) processes in the standard model are highly suppressed. However, if a fourth-generation charge $-\frac{1}{3}$ quark (b') exists and is lighter than both the t' [its partner in an SU(2) doublet] and the top quark (t), the charged-current (CC) decays $b' \to tW^-$ and $b' \to t'W^-$ are kinematically forbidden. The leading charged-current decay mode will then be $b' \to cW^-$, which is doubly Cabibbo-suppressed. In this situation loop-induced FCNC decays can dominate [2–4] provided $|V_{cb'}|/|V_{tb'}|$ is less than roughly 10^{-2} to 10^{-3}, depending on the b' and t' masses [4]. If $m_{b'} > m_Z + m_b$, the dominant FCNC decay mode is $b' \to bZ^0$ [4] as long as $b' \to bH$ is kinematically suppressed or forbidden [5]. For $m_t < m_{b'} < m_t + m_W$, the decay mode $b' \to tW^*$ becomes available but is suppressed by three-body phase space, and the $b' \to bZ^0$ channel can still dominate over the CC decay for b' masses up to about 230 GeV/c^2 [2,6].

Several experiments have searched explicitly for b' quarks decaying via FCNC [7]. The most stringent limit comes from the D0 Collaboration, which searched in the $b'\bar{b}' \to \gamma gb\bar{b}$ and $b'\bar{b}' \to \gamma\gamma b\bar{b}$ channels, excluding a b' quark mass up to $m_Z + m_b$ for a FCNC branching fraction larger than 50% [8]. CDF has excluded a long-lived b' quark with mass up to 148 GeV/c^2 and a lifetime of $\tau \approx 3.3 \times 10^{-11}$ sec, assuming $B(b' \to bZ^0) = 100\%$ [9]. If the CC decay $b' \to cW^-$ dominates, the lower mass bound of 128 GeV found in a D0 top quark search [10] also applies to the b' quark [11].

In this Letter, we report on a search for a b' quark using 88 ± 4 pb^{-1} of $p\bar{p}$ collisions at $\sqrt{s} = 1.8$ TeV collected with the CDF detector from 1994 to 1995. Fourth-generation b' quarks can be pair-produced in $p\bar{p}$ collisions through gg fusion and $q\bar{q}$ annihilation with the same cross section, for a given mass, as the top quark. We search for pair-produced b' quarks decaying via FCNC into bZ^0, where one Z^0 decays into leptons and the other decays hadronically. The signature is two high transverse momentum (p_T) leptons from the Z^0 decay, two high-p_T jets from the second Z^0, and two b jets whose p_T scales with the b' mass.

A detailed description of the CDF detector can be found elsewhere [12]. We briefly describe the components most relevant for this analysis. Inside a 1.4 T solenoidal magnetic field, the silicon vertex detector (SVX), the vertex time projection chamber (VTX), and the central tracking chamber (CTC) provide tracking information. The SVX, positioned immediately outside the beampipe and inside the VTX, consists of four layers of silicon microstrip detectors and covers $|z| < 25$ cm [13]. It provides precise track reconstruction in the plane transverse to the beam and is used to identify secondary vertices from the decay of b hadrons. The VTX is used to measure the position of the primary interaction vertex along the z axis. The CTC is a cylindrical drift chamber that covers the pseudorapidity range $|\eta| < 1.1$ and consists of 84 layers that are grouped in nine alternating superlayers of axial and stereo wires. Outside the solenoid, electromagnetic and hadronic calorimeters, arranged in a projective tower geometry, surround the tracking volume and are used to identify electrons and jets over the range $|\eta| < 4.2$. The electron energy is measured in the central electromagnetic calorimeter (CEM) ($|\eta| < 1.1$) and the end-plug electromagnetic calorimeter (PEM) ($1.1 < |\eta| < 2.4$). Outside the calorimeters, three systems of drift chambers in the region $|\eta| < 1.0$ provide muon identification.

We select events satisfying a high-p_T lepton trigger, containing a well-identified muon or electron in the central region, whose primary vertex is within 60 cm of the nominal interaction position. A trigger that requires one jet with $E_T > 10$ GeV, in addition to the lepton, is also used for muon events. Inclusive $Z^0 \to e^+e^-$ and $Z^0 \to \mu^+\mu^-$ samples are selected by requiring one primary lepton that satisfies tight lepton identification cuts and a second lepton satisfying loose identification cuts [14]. Dielectron events are selected by requiring at least one tight electron with transverse energy $E_T > 20$ GeV in the CEM and a second loose electron with $E_T > 10$ GeV in either the CEM or PEM calorimeters. Dimuon events are required to have one tight muon with transverse momentum $p_T > 20$ GeV/c in the central region and a second loose muon with $p_T > 10$ GeV/c. A calorimeter isolation cut is imposed on the second lepton. We accept events if the reconstructed ee or $\mu\mu$ invariant mass is between 75 and

105 GeV/c^2. After this selection there are 6287 (2940) Z^0 events remaining in the electron (muon) data sample.

In order to optimize our sensitivity to a b' quark signal we make a jet selection that depends on the b' mass being considered. Hadronic jets are selected using a clustering algorithm [15] with a cone size of $\Delta R = \sqrt{\Delta\eta^2 + \Delta\phi^2} = 0.4$. Each event is required to have at least three jets within $|\eta| < 2.0$, two of which with $E_T > 15$ GeV. For b' masses above 120 GeV/c^2, the third jet is required to have $E_T > 15$ GeV. For $m_{b'} \leq 120$ GeV/c^2, the E_T requirement on the third jet is relaxed to $E_T > 7$ GeV since the b jets for b' masses near the $m_Z + m_b$ threshold have low momentum. We define the variable $\sum E_T^{\text{jets}}$ as the summed transverse energy of jets with $E_T > 15$ GeV and $|\eta| < 2.0$ and require this quantity to be larger than $m_{b'}c^2 - 60$ GeV. Figure 1 shows the $\sum E_T^{\text{jets}}$ distribution for e^+e^- and $\mu^+\mu^-$ events passing the three-jet requirement for b' masses above 120 GeV/c^2. Also shown are the distributions expected from SM background and from a b' quark with a mass of 150 GeV/c^2 (see below).

We further require at least one jet to be tagged as a b quark by the SVX b-tagging algorithm developed for the top quark analysis [16]. The number of events passing each major selection criterion for each leptonic channel is shown in Table I. One $\mu\mu$ event passes all our selection criteria for $m_{b'} \leq 120$ GeV/c^2. This event has a third jet with $E_T = 8.3$ GeV which fails the third-jet E_T requirement for larger b' masses.

The signal acceptance and detection efficiencies are estimated from a combination of data and Monte Carlo simulation. We have generated $b'\bar{b}' \to bZ^0\bar{b}Z^0$ Monte Carlo samples for different b' masses between 100 and 210 GeV/c^2 using the HERWIG program [17] with

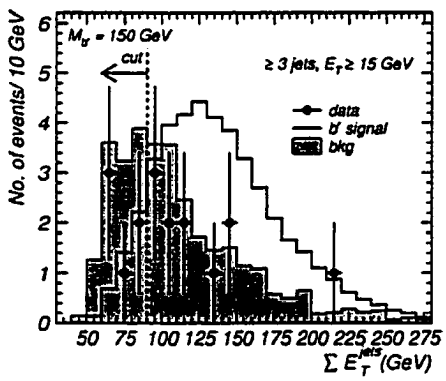

FIG. 1. $\sum E_T^{\text{jets}}$ distribution for events with at least 3 jets with $E_T > 15$ GeV and $|\eta| < 2$, before the b-tagging requirement. The expected SM background is shown shaded. The expected signal event distribution for a b' quark mass of 150 GeV/c^2 is shown as a solid line. The vertical dashed line represents the $\sum E_T^{\text{jets}}$ cut for this specific b' mass. Events to the right of this line are accepted.

MRSD0′ structure functions [18]. One Z^0 is required to decay into muons or electrons while the other is allowed to decay through any available decay channel. The CLEO QQ Monte Carlo program [19] is used to model the decays of b hadrons. These events are passed through a simulation of the CDF detector and are subjected to the same selection requirements as the data.

The electron trigger efficiency is determined from data to be (92 ± 1)%, while the muon trigger efficiency per event (82 ± 4)% is obtained from a combination of data and simulation. The efficiencies of the lepton identification cuts are determined using a $Z^0 \to e^+e^-$ ($\mu^+\mu^-$) data sample with an unbiased selection on one of the leptons. The $Z^0 \to e^+e^-$ and $Z^0 \to \mu^+\mu^-$ geometric and kinematic acceptance was obtained from the HERWIG Monte Carlo program. The total Z^0 detection efficiency times acceptance, including the isolation efficiency, is (41 ± 3)% for e^+e^- and (30 ± 3)% for $\mu^+\mu^-$ and is nearly independent of the b' mass.

The event b-tag efficiency rises with $m_{b'}$ from 17% for $m_{b'} = 100$ GeV/c^2 to values between 50% and 57% for masses above 150 GeV/c^2. The total acceptance times efficiency, not including the $B(Z \to l^+l^-)$, increases from 1.7% (1.6%) to 14% (11%) for the electron (muon) channel as $m_{b'}$ increases from 100 to 210 GeV/c^2 (Table II). This increase is due to the fact that a more massive b' leads to a more central event with more energetic jets in which, in addition, the b-tag algorithm is more efficient.

The dominant systematic uncertainties on the acceptance times efficiency arise from the jet energy scale and gluon radiation [14]. By varying parameters in the Monte Carlo simulation we estimate that the systematic uncertainty due to the jet energy scale in the electron (muon) channel is 16% (14%) for $m_{b'} = 100$ GeV/c^2 and less than 13% for higher masses. The presence of gluon radiation increases the jet multiplicity and therefore increases the efficiency of the three-jet requirement. This effect is more pronounced at low b' mass because the b quarks from low-mass b' decay are produced near threshold and therefore are detected with low efficiency. We estimate the systematic uncertainty due to this effect to be 19% (18%) in the electron (muon) channel for $m_{b'} = 100$ GeV/c^2, and less than 9% for a heavier b'. Other important systematic uncertainties arise from the b-tag efficiency (10%), parton distribution function (5%), total integrated luminosity

TABLE I. Events observed in data after each main selection requirement in both the electron and the muon channels.

$m_{b'}$	$Z^0 \to e^+e^-$			$Z^0 \to \mu^+\mu^-$		
(GeV/c^2)	3 jets	$\sum E_T^{\text{jets}}$	b-tag	3 jets	$\sum E_T^{\text{jets}}$	b-tag
100	34	31	0	32	29	1
120	34	20	0	32	21	1
140	9	8	0	8	5	0
160	9	4	0	8	4	0
180	9	1	0	8	3	0
200	9	1	0	8	2	0

TABLE II. Total acceptance (A) times efficiency (ϵ) and relative systematic uncertainties (δ_{total}) in the electron and muon channels, 95% C.L. upper limit on the pair-production cross section times the branching ratio of $b' \to bZ^0$ squared, and theoretical pair-production cross section [20].

	$Z^0 \to e^+e^-$		$Z^0 \to \mu^+\mu^-$			
$m_{b'}$ (GeV/c^2)	$(A \times \epsilon)$ (%)	δ_{total} (%)	$(A \times \epsilon)$ (%)	δ_{total} (%)	$\sigma \times B^2_{95\%\text{C.L.}}$ (pb)	σ_{theory} (pb)
100	1.7	29	1.6	27	37	102
110	4.6	21	4.2	21	11	61.6
120	7.6	20	6.4	19	6.5	38.9
130	8.2	19	6.8	19	3.8	25.4
140	9.9	19	8.3	19	3.1	16.9
150	11	19	9.2	19	2.8	11.7
160	12	19	9.8	19	2.6	8.16
170	12	19	10	19	2.5	5.83
180	13	19	10	19	2.4	4.21
190	13	19	11	19	2.4	3.06
200	13	19	11	19	2.4	2.26
210	14	19	11	19	2.3	1.68

(1.1%), lepton identification efficiency (4% for electrons, 5% for muons), isolation efficiency (4%), and trigger efficiency (1% for electrons, 5% for muons). The total uncertainty on the acceptance times efficiency is shown as a function of b' mass in Table II.

The only non-negligible background is from Z^0 events with associated QCD hadronic jets. This background is estimated using a combination of the VECBOS [21] and HERWIG Monte Carlo programs. VECBOS calculates the leading-order matrix elements for Z^0 + three partons events using the MRSD0′ structure functions [22]. A partial higher-order correction to the tree-level diagrams is obtained by including gluon radiation and hadronic fragmentation using HERWIG. These Z^0 events are then passed through a simulation of the CDF detector. We estimate the b-tag rate in Z^0 plus jet events directly from data using a technique developed for the top analysis [23]. We apply the b-tag rates measured in an inclusive jet sample to the Z^0 + jets events that pass all the other selection criteria. This method overestimates the background because the inclusive jet sample contains heavy-quark contributions that are not present in Z^0 + jets events. We expect approximately two background events for $m_{b'} \leq 120$ GeV/c^2 and less than one event for $m_{b'} > 120$ GeV/c^2, in agreement with the number of events observed in the data.

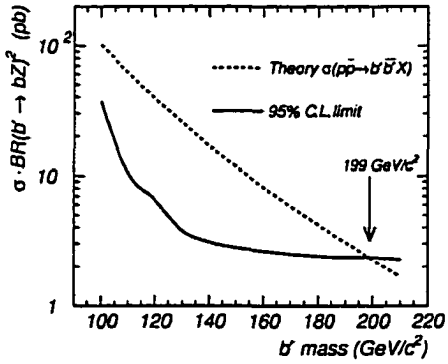

FIG. 2. The 95% confidence level upper limit on $p\bar{p} \to b'\bar{b}'X$ production cross section times the $b' \to bZ^0$ branching ratio squared (solid). The dashed curve shows the predicted $\sigma_{p\bar{p}\to b'\bar{b}'} \times [B(b' \to bZ^0)]^2$ with the NLO production cross section from Ref. [20] and $B(b' \to bZ^0) = 1$.

Under the assumption that the observed $\mu\mu$ event is from signal, that is, without subtracting background, we obtain a conservative 95% confidence level upper limit on the $\sigma_{p\bar{p}\to b'\bar{b}'} \times [B(b' \to bZ^0)]^2$. The limit is presented as a function of the b' mass in Table II. We have used a Bayesian method to calculate the limit and treat the number of expected signal events as a Poisson distribution convoluted with a Gaussian systematic uncertainty. Using the theoretical next-to-leading-order (NLO) b' pair production cross section [20] and assuming that $B(b' \to bZ^0)$ is 100%, we exclude at 95% confidence level b' masses from 100 to 199 GeV/c^2, as shown in Fig. 2. This search is also sensitive to other b' decay channels such as $b' \to bH$ or $b' \to cW^-$ as long as $B(b' \to bZ)$ is not negligible, since the hadronic decays of the H or W are kinematically similar to those of the Z. The acceptance for $b'\bar{b}' \to b\bar{b}ZH$ is 1.7 to 0.5 times the acceptance for $b'\bar{b}' \to b\bar{b}ZZ$, depending on the Higgs and b' masses and not including the $B(Z \to l^+l^-)$. However, if we conservatively assume no sensitivity to these decay modes, we exclude a b' mass from 104 to 152 GeV for $B(b' \to bZ) \geq 50\%$.

We thank the Fermilab staff and the technical staffs of the participating institutions for their vital contributions. This work was supported by the U.S. Department of Energy and National Science Foundation; the Italian Istituto Nazionale di Fisica Nucleare; the Ministry of Education, Science, Sports and Culture of Japan; the Natural Sciences and Engineering Research Council of Canada; the National Science Council of the Republic of China; the Swiss National Science Foundation; the A. P. Sloan Foundation; and the Bundesministerium fuer Bildung und Forschung, Germany.

[1] W. J. Marciano, Phys. Rev. D **41**, 219 (1990); P. H. Frampton and D. Ng, *ibid.* **43**, 3034 (1991); P. Q. Hung, Phys. Rev. Lett. **80**, 3000 (1998); J. F. Gunion, D. W. McKay, and H. Pois, Phys. Rev. D **53**, 1616 (1996); V. Barger, M. S. Berger, and R. J. N. Phillips, *ibid.* **52**, 1663 (1995); M. Carena, H. E. Haber, and C. E. M. Wagner, Nucl. Phys. **B472**, 55 (1996); Z. Berezhiani and E. Nardi, Phys. Lett. B **355**, 199 (1995).
[2] P. Frampton, P. Q. Hung, and M. Sher, hep-ph/9903387, Phys. Rep. (to be published).
[3] V. Barger, R. J. N. Phillips, and A. Soni, Phys. Rev. Lett. **57**, 1518 (1986).
[4] W. S. Hou and R. G. Stuart, Nucl. Phys. **B320**, 277 (1989); Phys. Rev. Lett. **62**, 617 (1989).
[5] W. S. Hou and R. G. Stuart, Phys. Rev. D **43**, 3669 (1991).
[6] P. H. Frampton and P. Q. Hung, Phys. Rev. D **58**, 057704 (1998).
[7] K. Abe *et al.*, Phys. Rev. Lett. **63**, 1776 (1989); S. Eno *et al.*, *ibid.* **63**, 1910 (1989); G. S. Abrams *et al.*, *ibid.* **63**, 2447 (1989); I. Adachi *et al.*, Phys. Lett. B **234**, 197 (1990); D. Decamp *et al.*, *ibid.* **236**, 511 (1990); M. Z. Akrawy *et al.*, *ibid.* **246**, 285 (1990).
[8] S. Abachi *et al.*, Phys. Rev. Lett. **78**, 3818 (1997).
[9] F. Abe *et al.*, Phys. Rev. D **58**, 051102 (1998).
[10] S. Abachi *et al.*, Phys. Rev. D **52**, 4877 (1995).
[11] C. Caso *et al.*, Eur. Phys. J. C **3**, 1 (1998).
[12] F. Abe *et al.*, Nucl. Instrum. Methods Phys. Res., Sect. A **271**, 387 (1988); P. Azzi *et al.*, *ibid.* **360**, 137 (1995).
[13] The CDF coordinate system uses (θ, ϕ, z), where the proton beam is in the z direction and θ and ϕ are, respectively, the polar angle and the azimuthal angle. The transverse momentum of a particle is $p_T = p \sin\theta$.
[14] J. Guimarães da Costa, Ph.D. thesis, University of Michigan, 2000 (unpublished).
[15] F. Abe *et al.*, Phys. Rev. D **45**, 1448 (1992).
[16] F. Abe *et al.*, Phys. Rev. D **51**, 4623 (1995).
[17] G. Marchesini and B. R. Webber, Nucl. Phys. **B310**, 461 (1988); G. Marchesini *et al.*, Comput. Phys. Commun. **67**, 465 (1992).
[18] A. D. Martin, R. G. Roberts, and W. J. Stirling, Phys. Lett. B **306**, 145 (1993); **309**, 492(E) (1993).
[19] P. Avery, K. Read, and G. Trahern, Cornell Internal Note CSN-212, 1985 (unpublished).
[20] E. Laenen *et al.*, Phys. Lett. B **321**, 254 (1994); E. Laenen (private communication).
[21] F. A. Berends *et al.*, Nucl. Phys. **B357**, 32 (1991).
[22] The QCD renormalization and factorization scales are set by the $\langle p_T \rangle^2$ of the generated partons. The outgoing partons are generated with a minimum p_T of 6 GeV/c, $|\eta| < 2.5$, and $\Delta R > 0.4$ between partons.
[23] F. Abe *et al.*, Phys. Rev. D **50**, 2966 (1994); Phys. Rev. Lett. **73**, 225 (1994).

Bibliography

[1] C. Caso *et al.*, Eur. Phys. J. **C3**, 1 (1998).

[2] W. J. Marciano, Phys. Rev. D **41**, 219 (1990).

[3] V. A. Miransky, M. Tanabashi and K. Yamawaki, Phys. Lett. B **221**, 177 (1989).

[4] K. R. Dienes, E. Dudas, T. Gherghetta, Phys. Lett. B **436**, 55 (1998); Nucl. Phys. **B537**, 47 (1999).

[5] J. F. Gunion, D. W. McKay and H. Pois, Phys. Rev. D **53**, 1616 (1996).

[6] Z. Berezhiani and E. Nardi, Phys. Lett. B **355**, 199 (1995).

[7] M. Carena, H. E. Haber and C. E. M. Wagner, Nucl. Phys. **B472**, 55 (1996).

[8] P. H. Frampton T. W. Kephart, Phys. Rev. Lett. **66**, 1666 (1991); P. H. Frampton and D. Ng, Phys. Rev. D **43**, 3034 (1991);

[9] P. Q. Hung, Phys. Rev. Lett. **80**, 3000 (1998).

[10] Amitava Datta, Pramana J. Phys. 40 503 (1993).

[11] P. Frampton, P. Q. Hung and M. Sher, hep-ph/9903387 (to be published in Physics Reports).

[12] V. Barger, R. J. N. Phillips and A. Soni, Phys. Rev. Lett. **57**, 1518 (1986).

[13] W. S. Hou and R. G. Stuart, Nucl. Phys. **B320**, 277 (1989); Phys. Rev. Lett. **62**, 617 (1989).

[14] P. Agrawal and W. S. Hou, Phys. Rev. D **42**, 1022 (1992).

[15] F. Abe *et al.*, Phys. Rev. Lett. **64**, 147 (1990).

[16] W. S. Hou and R. G. Stuart, Phys. Rev. D **43**, 3669 (1991).

[17] P. H. Frampton and P. Q. Hung, Phys. Rev. D **58**, 057704 (1998).

[18] K. Abe *et al.*, Phys. Rev. Lett. **63**, 1776 (1989); S. Eno *et al.*, *ibid.* **63**, 1910 (1989); G. S. Abrams *et al.*, *ibid.* **63**, 2447 (1989); I. Adachi *et al.*, Phys. Lett. B **234**, 197 (1990); D. Decamp *et al.*, *ibid.* **236**, 511 (1990); M. Z. Akrawy *et al.*, *ibid.* **246**, 285 (1990).

[19] S. Abachi *et al.*, Phys. Rev. Lett. **78**, 3818 (1997).

[20] F. Abe *et al.*, Phys. Rev. D **58**, 051101 (1998).

[21] A. Connolly, Proceedings of 1999 DPF Meeting, hep-ph/9904010.

[22] S. Abachi *et al.*, Phys. Rev. D **52**, 4877 (1995).

[23] M. Veltman, Nucl. Phys. **B123**, 89 (1977).

[24] U. Amaldi *et al.*, Phys. Rev. D **36**, 1385 (1987).

[25] E. Guillian, Ph.D. thesis, University of Michigan, 1999 (unpublished).

[26] F. Abe *et al.*, Nucl. Instrum. Methods A **271**, 387 (1988).

[27] F. Abe *et al.*, Phys. Rev. D **52**, 4784 (1995).

[28] H. Minemura *et al.*, Nucl. Instrum. Methods A **238**, 18 (1985).

[29] C. Haber *et al.*, Nucl. Inst. and Methods, **A289**, 388 (1990).

[30] D. Amidei *et al.*, Nucl. Inst. and Methods, **A342**, 251 (1994).

[31] D. Amidei *et al.*, Nucl. Inst. and Methods, **A350**, 73 (1994).

[32] P. Azzi *et al.*, Nucl. Inst. and Methods, **A360**, 137 (1995).

[33] F. Snider *et al.*, Nucl. Inst. and Methods **A268**, 75 (1988).

[34] F. Bedeschi *et al.*, Nucl. Instrum. Methods **A268**, 50 (1988).

[35] L. Balka *et al.*, Nucl. Inst. and Methods, **A267**, 272 (1988).

[36] S. R. Hahn *et al.*, Nucl. Inst. and Methods, **A267**, 351 (1988).

[37] K. Yasuoka *et al.*, Nucl. Inst. and Methods, **A267**, 315 (1988).

[38] R. G. Wagner *et al.*, Nucl. Inst. and Methods, **A267**, 330 (1988).

[39] T. Devlin *et al.*, Nucl. Inst. and Methods, **A268**, 24 (1988).

[40] S. Bertolucci *et al.*, Nucl. Inst. and Methods, **A267**, 301 (1988).

[41] Y. Fukui *et al.*, Nucl. Inst. and Methods, **A267**, 280 (1988).

[42] S. Cihangir *et al.*, Nucl. Inst. and Methods, **A267**, 249 (1988).

[43] G. Brandenburg *et al.*, Nucl. Inst. and Methods, **A267**, 257 (1988).

[44] G. W. Foster *et al.*, Nucl. Inst. and Methods, **A269**, 93 (1988).

[45] Top Group, *Sample Selection for Run 1b Top Search*, CDF Internal Note 2966, 1995 (unpublished).

[46] M. Kruse, *Observation of the Top Quark Pair Production in the Dilepton Decay Channel from Proton-Antiproton Collisions at* $\sqrt{s} = 1.8$ TeV, Ph.D. thesis, Purdue University, 1996 (unpublished).

[47] D. Gerdes, *Study of conversion removal for leptons+jets sample*, CDF Internal Note 2903, 1994 (unpublished).

[48] F. Abe *et al.*, Phys. Rev. D **45**, 1448 (1992).

[49] F. Abe *et al.*, Phys. Rev. D **51**, 4623 (1995).

[50] G. Marchesini and B. R. Webber, Nucl. Phys. **B310**, 461 (1988); G. Marchesini *et al.*, Comput. Phys. Commun. **67**, 465 (1992).

[51] Herbet Greenlee, private communication. Subroutine used by the D0 collaboration in reference [19].

[52] A. D. Martin, R. G. Roberts and W. J. Stirling, Phys. Lett. B **306**, 145 (1993); **309**, 492(E) (1993).

[53] P. Avery, K. Read, and G. Trahern, Cornell Internal Note CSN-212, 1985 (unpublished).

[54] Cross section and Branching Ratios Working Group, *$t\bar{t}$ Acceptance Calculation for the Run 1b SVX B-tag Analysis*, CDF Internal Note 3403, 1995 (unpublished).

[55] D. Glenzinski, Observation of the Top Quark in Proton-Antiproton Collisions at a Center of Mass Energy of 1.8 TeV, Ph.D. thesis, The Johns Hopkins University, 1995.

[56] M. Kruse *et al.*, *Top Acceptance in the Dilepton Channel for Run 1*, CDF Internal Note 3300, 1995 (unpublished).

[57] K. Pitts and L. Qi, *The CFT Efficiency for High-p_T Tracks in Run 1b*, CDF Internal Note 4000, 1997 (unpublished).

[58] R. Roser and T. Liss, *A Measurement of the Trigger Efficiencies for $t\bar{t}$ Events in Run 1B*, CDF Internal Note 3442, 1995 (unpublished). We have used a newer version of C$TOP:SIM_MUTRIG.CDF which is available in FNALD and dated from October 18, 1996.

[59] F. Abe *et al.*, Phys. Rev. Lett. **80**, 2773 (1998).

[60] C. Campagnari, *Normalization of Run 1b μ+ jets data*, CDF Internal Note 2821, 1994 (unpublished).

[61] K. Bloom, $Z^0 \to e^+e^-$ *and* $Z^0 \to \mu^+\mu^-$ *Cross Sections in Run 1b*, CDF Internal Note 4528, 1998 (unpublished).

[62] M. Kruse *et al.*, *High* p_T *Lepton ID Efficiencies for Run 1b*, CDF Internal Note 2883, 1994 (unpublished).

[63] M. Kruse and J. Konigsberg, *Top Dilepton Analysis - Update to 110* pb^{-1}, CDF Internal Note 3482, 1997 (unpublished).

[64] G. Unal, *Track efficiency and SVX scale factor*, CDF Internal Note 3563, 1995 (unpublished).

[65] G. Appolinari *et al.*, *Measurement of the data to simulation scale factor for the tagging efficiencies of SECVTX and JPB*, CDF Internal Note 4257, 1999 (unpublished).

[66] P. Derwent *et al.*, *God parents report on the new* $t\bar{t}$ *SVX cross section measurement*, CDF Internal Note 4939, 1999 (unpublished).

[67] The Top Group, *The New Combined CDF* $t\bar{t}$ *production cross section for Run 1*, CDF Internal Note 5043, 1999 (unpublished).

[68] J. Benlloch, *Proceedings of the 1992 DPF Meeting*, 10-14 Nov., 1992, Batavia, IL., ed. C. H. Albright *et al.*, World Scientific, 1091 (1993).

[69] F. Abe *et al.*, Phys. Rev. D **50**, 2966 (1994); Phys. Rev. Lett. **73**, 225 (1994).

[70] F. A. Berends *et al.*, Nucl. Phys. **B357**, 32 (1991).

[71] F. Abe *et al.*, Phys. Rev. Lett. **77**, 448 (1996).

[72] T. Sjöstrand, Computer Phys. Commun. **82**, 74 (1994).

[73] For a description of the CTEQ global fits, see J. Botts *et al.*, Phys. Lett. B **304**, 159 (1993). For a description of the Morfin-Tung (MT) set, see J. Morfin and W.K. Tung, *ibid* **52**, 13 (1991). For a description of the Gluck-Reya-Vogt (GRV) set, see M. Gluck, E. Reya, and A. Vogt, Z. Phys. C **53**, 127 (1992).

[74] D. Cronin-Hennessy *et al.*, Fermilab preprint PUB-99-162 (1999), submitted to Nucl. Instrum. Methods.

[75] R. Cousins, Am. J. Phys. **63**, 398 (1995).

[76] J. Conway and K. Maeshima, *Upper Limits on Poisson Processes Incorporating Uncertainties in Acceptance and Background*, CDF Internal Note 4476, 1998 (unpublished).

[77] E. Laenen *et al.*, Phys. Lett. B **321**, 254 (1994); E. Laenen (private communication).

[78] R. J. Hollebeek *et al.*, *The evaluation of upper limits for top quark production using combined measurements*, CDF Internal Note 1109, 1990 (unpublished).

[79] A. Blondel for the ALEPH collaboration, LEP Committee Meeting, CERN, November 1999.

[80] J. Erler and P. Langacker, hep-ph/9809352.

[81] M. Sher, private communication.

2017 ProQuest Distribution Agreement

This Agreement is between the author (Author) and ProQuest LLC, through its ProQuest Dissertation Distribution business (formerly ProQuest/UMI). Under this Agreement, Author grants ProQuest certain rights to preserve, archive and distribute the dissertation or thesis (the Work), abstract, and index terms provided by Author to ProQuest.

Section I. License for Inclusion of the Work in ProQuest Publishing Program

Grant of Rights. Author hereby grants to ProQuest the **non-exclusive**, worldwide right to reproduce, distribute, display and transmit the Work (in whole or in part) in such tangible and electronic formats as may be in existence now or developed in the future. Author further grants to ProQuest the right to include the abstract, bibliography and other metadata in the ProQuest Dissertations & Theses database (PQDT) and in ProQuest Dissertation Abstracts International and any successor or related index and/or finding products or services.

ProQuest Publishing Program - Election and Elements. The rights granted above shall be exercised according to the publishing option selected by Author in Section III, Author Options, and subject to the following additional Publishing Program requirements:

- Distribution of the Work. Except as restricted by Author in the publishing option selected, the rights granted by Author automatically include (1) the right to allow sale and distribution of the Work, in whole or in part, by ProQuest and its sales agents and distributors and (2) the right to make the Abstract, bibliographic data and any meta data associated with the Work available to search engines and harvesters.
- Restrictions. ProQuest will use commercially reasonable efforts to restrict the distribution of the Work as provided under the publishing option selected by Author or *as later elected by Author* through direct contact with ProQuest. Such election is subject to Author's Degree Granting Institution Directives. With respect to restrictions requested after submission of the Work, Author acknowledges that ProQuest cannot recall or amend previously distributed versions of the Work.
- Removal of Work from the Program. ProQuest may elect not to distribute the Work if it believes that all necessary rights of third parties have not been secured. Refer to the website http://www.proquest.com/products_umi/dissertations/ for information about copyright and your dissertation or thesis. If Author's degree is rescinded, and/or the degree-granting institution so directs, ProQuest will expunge the Work from its publishing program in accordance with its then current publishing policies.
- Degree Granting Institution Directives. Author is solely responsible for any conflict between policies and directions of Author's degree-granting institution, Author's choice of publishing model, and/or any restriction Author places on the use of the Work. For the avoidance of doubt, ProQuest is not responsible for access to the Work that is provided by Author's degree-granting institution through its library or institutional repository. Author must work directly with Author's degree granting institution to ensure application of any restrictions to access relating to the Work by Author's degree granting institution.

.

Delivery of the Work. Author shall provide to ProQuest the Work and all necessary supporting documents during the online submission process, according to the Instructions accompanying this agreement.

Rights Verification. Author represents and warrants that Author is the copyright holder of the Work and has obtained all necessary rights to permit ProQuest to reproduce and distribute third party materials contained in any part of the Work, including all necessary licenses for any non-public, third party software necessary to access, display, and run or print the Work. Author is solely responsible and will indemnify ProQuest for any third party claims related to the Work as submitted for publication.

Open Access Publishing Plus

☑ I want the broadest possible dissemination of my work, and I want to provide free global access to the electronic copy of my work via the internet.

☑ I understand that I will not be eligible to receive royalties.

I want major search engines (e.g. Google, Yahoo) to discover my work. Learn more: http://www.proquest.com/en-US/products/dissertations/google.shtml

☑ Yes

☐ No

Acknowledgment: I have read, understand and agree to this ProQuest Publishing Agreement, including all rights and restrictions included within the publishing option chosen by me as indicated above.

REQUIRED Author's signature_____ **Date**____**2018/01/19**_____

(Print Name)_____**João Pedro Barreiro Guimarães da Costa**_____

Institution conferring degree _____**University of Michigan**_____

This page must accompany your manuscript and the rest of the submission materials

Please check type of manuscript:

___ M (Master's Thesis)

___ D (Dissertation)

Dissertation/Master's Thesis Submission Form

Please print clearly in block letters

Personal Information

Last Name _____ Middle Name or Initial _____

First Name _____ Country (ies) of Citizenship _____

Degree & Dissertation Information

Title of Dissertation/ Thesis _____

Institution conferring degree _____ Degree awarded (abbreviate; e.g., Ph.D.) _____

College, School, or Division _____ Year degree awarded _____

Department or Program _____ Year manuscript completed _____

Advisor/Committee Chair _____

Committee Member _____ Committee Member _____

Committee Member _____ Committee Member _____

Committee Member _____ Committee Member _____

Language of manuscript _____

Primary Subject Category: Enter the 4-digit code and category name from the Subject Category Guide that most closely describes the area of your research. Code_____ Category_____

You may suggest two additional subject categories that may aid in the discovery of your work in our digital database.

Code_____ Category_____ Code_____ Category_____

Provide up to 6 keywords or short phrases for citation indices, library cataloging, and database searching.

_____ _____ _____

_____ _____ _____

Current Contact Information

Current Email Address _____

Street Address _____

Please provide your postal address if you are interested in receiving royalties on sales of your thesis.

City _____ Province _____ Daytime Phone _____

Country _____ Postal Code _____ Evening Phone _____

Permanent Contact Information

Permanent Email Address _____

Street Address (line 1) _____

City _____ Province _____ Future Phone _____

Country _____ Postal Code _____ Alternate Future Phone _____

THIS PAGE MUST ACCOMPANY YOUR MANUSCRIPT AND THE REST OF YOUR SUBMISSION MATERIALS

Subject Categories

The ProQuest Dissertations & Theses (PQDT) database and the ProQuest citation indices are arranged by subject categories. Please select the one category below that best describes your field of research or creative work. You may add one or two additional categories on your submission form that will also be associated with your work as secondary subjects.

Arts, Business, Education, Humanities, and Social Sciences

AREA, ETHNIC, AND GENDER STUDIES

African American studies	0296
African studies	0293
American studies	0323
Asian American studies	0343
Asian studies	0342
Baltic studies	0361
Black studies	0325
Canadian studies	0385
Caribbean studies	0432
Classical studies	0434
East European studies	0437
Ethnic studies	0631
European studies	0440
French Canadian culture	0482
Gender studies	0733
GLBT studies	0492
Hispanic American studies	0737
Holocaust studies	0507
Islamic culture	0512
Judaic studies	0751
Latin American studies	0550
Middle Eastern studies	0555
Native American studies	0740
Near Eastern studies	0559
North African studies	0560
Pacific Rim studies	0561
Regional studies	0604
Scandinavian studies	0613
Slavic studies	0614
South African studies	0654
South Asian studies	0638
Sub Saharan Africa studies	0639
Women's studies	0453

BUSINESS

Accounting	0272
Arts management	0424
Banking	0770
Business	0310
Entrepreneurship	0429
Finance	0508
Management	0454
Marketing	0338
Sports management	0430

COMMUNICATIONS AND INFORMATION SCIENCES

Communication	0459
Information science	0723
Journalism	0391
Library science	0399
Mass communication	0708
Technical communication	0643

Web studies	0646

FINE AND PERFORMING ARTS

Art criticism	0365
Art history	0377
Cinematography	0435
Dance	0378
Design	0389
Film studies	0900
Fine arts	0357
Music	0413
Performing arts	0641
Theater	0465
Theater history	0644

EDUCATION

Adult education	0516
Art education	0273
Bilingual education	0282
Business education	0688
Community college education	0275
Continuing education	0651
Curriculum development	0727
Early childhood education	0518
Education	0515
Education finance	0277
Education policy	0458
Educational administration	0514
Educational evaluation	0443
Educational leadership	0449
Educational psychology	0525
Educational technology	0710
Educational tests & measurements	0288
Elementary education	0524
English as a second language	0441
Foreign language instruction	0444
Gifted education	0445
Health education	0680
Higher education	0745
Higher education administration	0446
History of education	0520
Home economics education	0278
Industrial arts education	0521
Instructional design	0447
Language arts	0279
Mathematics education	0280
Middle school education	0450
Multicultural education	0455
Music education	0522
Pedagogy	0456
Performing arts education	0457
Philosophy of education	0998
Physical education	0523
Reading instruction	0535
Religious education	0527
School counseling	0519
Science education	0714
Secondary education	0533
Social sciences education	0534
Sociology of education	0340
Special education	0529
Teacher education	0530
Vocational education	0747

HUMANITIES

HISTORY

African history	0331
American history	0337
Ancient history	0579
Asian history	0332
Black history	0328
Canadian history	0334
European history	0335
History	0578
History of Oceania	0504
History of science	0585
Latin American history	0336
Medieval history	0581
Middle Eastern history	0333
Military history	0772
Modern history	0582
Russian history	0724
World history	0506

LANGUAGE & LITERATURE

African literature	0316
American literature	0591
Ancient languages	0289
Asian literature	0305
British and Irish literature	0593
Canadian literature	0352
Caribbean literature	0360
Classical literature	0294
Comparative literature	0295
English literature	0593
French Canadian literature	0355
Germanic literature	0311
Icelandic & Scandinavian literature	0362
Language	0679
Latin American literature	0312
Linguistics	0290
Literature	0401
Literature of Oceania	0356
Medieval literature	0297
Middle Eastern literature	0315
Modern language	0291
Modern literature	0298
Rhetoric	0681
Romance literature	0313
Slavic literature	0314

PHILOSOPHY AND RELIGION

Aesthetics	0650
Biblical studies	0321
Canon law	0375
Clerical studies	0319
Comparative religion	0618
Divinity	0376
Epistemology	0393
Ethics	0394
Logic	0395
Metaphysics	0396
Pastoral counseling	0397
Philosophy	0422
Philosophy of Religion	0322
Philosophy of science	0402
Religion	0318
Religious history	0320
Spirituality	0647
Theology	0469

LAW AND LEGAL STUDIES

Alternative dispute resolution	0649
Intellectual property	0513
International law	0616
Law	0398
Patent law	0562

SOCIAL SCIENCES

Archaeology	0324
Area planning and development	0341
Criminology	0627
Cultural anthropology	0326
Demography	0938
Economic history	0509
Economic theory	0511
Economics	0501
Economics, Commerce-Business	0505
Economics, Labor	0510
Folklore	0358
Forensic anthropology	0339
Geography	0366
Individual & family studies	0628
International relations	0601
Labor relations	0629
Military studies	0750
Organization theory	0635
Organizational behavior	0703
Peace studies	0563
Physical anthropology	0327
Political Science	0615
Public administration	0617
Public policy	0630
Recreation and tourism	0814
Social research	0344
Social structure	0700
Social work	0452
Sociolinguistics	0636
Sociology	0626
Transportation planning	0709
Urban planning	0999

INTERDISCIPLINARY

Alternative energy	0363
Biographies	0304
Climate change	0404
Cultural resources management	0436
Energy	0791
Food science	0359
Home economics	0386
Information technology	0489
Multimedia	0558
Museum studies	0730
Sustainability	0640
Textile research	0994
Wood sciences	0746

Behavioral, Natural, and Physical Sciences

AGRICULTURE

Agriculture	0473
Agronomy	0285
Animal diseases	0476
Animal sciences	0475
Fisheries and aquatic sciences	0792
Forestry	0478
Horticulture	0471
Plant pathology	0480
Plant sciences	0479
Range management	0777
Soil sciences	0481
Urban forestry	0281
Wildlife management	0286

ARCHITECTURE

Architecture	0729
Architectural engineering	0462
Landscape architecture	0390

BEHAVIORAL SCIENCES

Animal behavior	0602
Behavioral sciences	0384
Clinical psychology	0622
Cognitive psychology	0633
Counseling psychology	0603
Developmental psychology	0620
Experimental psychology	0623
Occupational psychology	0624
Personality psychology	0625
Physiological psychology	0989
Psychobiology	0349
Psychology	0621
Quantitative psychology and psychometrics	0632
Social psychology	0451

BIOLOGICAL SCIENCES

Biochemistry	0487
Bioinformatics	0715
Biology	0306
Biomechanics	0648
Biophysics	0786
Biostatistics	0308
Cellular biology	0379
Developmental biology	0758
Endocrinology	0409
Entomology	0353
Evolution & development	0412
Genetics	0369
Histology	0414
Limnology	0793
Microbiology	0410
Molecular biology	0307
Morphology	0287
Neurosciences	0317
Parasitology	0718
Physiology	0719
Plant biology	0309
Systematic biology	0423
Virology	0720
Zoology	0472

ECOSYSTEM SCIENCES

Ecology	0329
Macroecology	0420
Paleoecology	0426

ENGINEERING

Aerospace engineering	0538
Artificial intelligence	0800
Automotive engineering	0540
Biomedical engineering	0541
Chemical engineering	0542
Civil engineering	0543
Computer engineering	0464
Computer science	0984
Electrical engineering	0544
Engineering	0537
Geological engineering	0466
Geophysical engineering	0467
Geotechnology	0428
Industrial engineering	0546
Mechanical engineering	0548
Mining engineering	0551
Naval engineering	0468
Nanotechnology	0652
Nuclear engineering	0552
Ocean engineering	0547
Operations research	0796
Packaging	0549
Petroleum engineering	0765
Plastics	0795
Robotics	0771
System science	0790

ENVIRONMENTAL SCIENCES

Conservation biology	0408
Environmental economics	0438
Environmental education	0442
Environmental engineering	0775
Environmental geology	0407
Environmental health	0470
Environmental justice	0619
Environmental law	0439
Environmental management	0474
Environmental philosophy	0392
Environmental science	0768
Environmental studies	0477
Land use planning	0536
Natural resource management	0528
Water resources management	0595
Wildlife conservation	0284

MATHEMATICAL AND PHYSICAL SCIENCES

Acoustics	0986
Analytical chemistry	0486
Applied mathematics	0364
Astronomy	0606

GEOSCIENCES

Aeronomy	0367
Atmospheric chemistry	0371
Atmospheric sciences	0725
Biogeochemistry	0425
Biological oceanography	0416
Chemical oceanography	0403
Continental dynamics	0406
Geobiology	0483
Geochemistry	0996
Geographic information science and geodesy	0370
Geology	0372
Geomorphology	0484
Geophysics	0373
Hydrologic sciences	0388
Marine geology	0556
Meteorology	0557
Mineralogy	0411
Paleoclimate science	0653
Paleontology	0418
Petroleum geology	0583
Petrology	0584
Physical geography	0368
Physical oceanography	0415
Planetology	0590
Plate tectonics	0592
Remote sensing	0799
Sedimentary geology	0594

HEALTH AND MEDICAL SCIENCES

Aging	0493
Alternative medicine	0496
Audiology	0300
Dentistry	0567
Epidemiology	0766
Gerontology	0351
Health care management	0769
Health sciences	0566
Immunology	0982
Kinesiology	0575
Medical ethics	0497
Medical imaging and radiology	0574
Medicine	0564
Mental health	0347
Nursing	0569
Nutrition	0570
Obstetrics and gynecology	0380
Occupational health	0354
Occupational therapy	0498
Oncology	0992
Ophthalmology	0381
Osteopathic medicine	0499
Pathology	0571
Pharmaceutical sciences	0572
Pharmacology	0419
Physical therapy	0382
Public health	0573
Public health occupations education	0500
Speech therapy	0460
Surgery	0576
Toxicology	0383
Veterinary medicine	0778

Astrophysics	0596
Atomic physics	0748
Chemistry	0485
Condensed matter physics	0611
Electromagnetics	0607
High temperature physics	0597
Inorganic chemistry	0488
Low temperature physics	0598
Materials science	0794
Mathematics	0405
Mechanics	0346
Molecular chemistry	0431
Molecular physics	0609
Nanoscience	0565
Nuclear chemistry	0738
Nuclear physics	0756
Optics	0752
Organic chemistry	0490
Particle physics	0798
Physical chemistry	0494
Physics	0605
Plasma physics	0759
Polymer chemistry	0495
Quantum physics	0599
Statistics	0463
Theoretical mathematics	0642
Theoretical physics	0753